Dendritic integration of sensory information in perceptual decision-making



Lukas Groschner

Keble College

University of Oxford

In partial fulfilment of the requirements for the degree

Doctor of Philosophy

Hilary 2018

Acknowledgements

I am deeply grateful to those who have contributed to this work and who have inspired and supported me throughout my studies. First and foremost, I would like to thank Gero Miesenböck; I hope that I can retain and pass on some of his scientific creativity, serenity, generosity, and the academic freedom I got to experience. I am grateful to Shamik DasGupta for teaching me how to 'fly', to Rafal Bogacz for helping with the drift-diffusion model, and to my examiners Peter Magill and Mark Stopfer for their time and valuable comments on this manuscript. I would also like to thank Laura Chan Wah Hak, Diogo Pimentel, Eleftheria Vrontou, Cliff Talbot, Katerina Christodoulou, Bill Podlaski, Kay Ellison, Jan Kropf, and members of the Centre for Neural Circuits and Behaviour, present and past, for their help. This work was supported by a Wellcome Trust OXION studentship.

I am eternally grateful to my loving parents for their unwavering support throughout my life and across the sea. Most importantly, I want to thank Eva and Nora, whom I share everything with. Thank you for your confidence, your immeasurable help, and your endless patience.

Abstract

Perceptual decisions require the temporal integration of sensory evidence to a response threshold. How the brain performs this operation is unknown. In fruit flies, expression of the forkhead box P transcription factor (FoxP) in αβ core ($\alpha\beta_c$) Kenyon cells of the mushroom bodies influences decision times in odour discrimination tasks. Flies with a hypomorphic mutation in the *FoxP* locus take longer to commit to a choice than wild-type flies, especially in difficult tasks.

Using calcium imaging and patch clamp electrophysiology *in vivo*, I investigate how FoxP shapes the biophysical properties of $\alpha\beta_c$ neurons and link these properties to the flies' olfactory decision-making behaviour. I find that $\alpha\beta_c$ Kenyon cells integrate individual odour-evoked synaptic inputs to action potential threshold at time scales matching the speed of olfactory discrimination. FoxP, by controlling the abundance of the voltage-gated potassium channel Shal (K_V4) in $\alpha\beta_c$ Kenyon cell dendrites, determines the integrative properties of these neurons and dictates decision times. Targeted expression of dominant-negative or functional Shal in $\alpha\beta_c$ Kenyon cells is sufficient to correct or reproduce, respectively, the *FoxP* mutant phenotype.

Subthreshold dynamics in membrane voltage thus have a previously unrecognised influence on temporal aspects of decision-making.

Contents

Acknowledgements **3**

Abstract **4**

List of figures **6**

List of tables **7**

Abbreviations **8**

1. Introduction **10**

1.1 Temporal integration and the neural basis of decision-making 10

1.2 Drift-diffusion models of decision-making 12

1.3 Neural network architectures of decision-making 14

1.4 Architecture of an olfactory system 16

1.5 FoxP influences the speed of olfactory decisions 20

2. Methods **22**

2.1 Fly strains and culture 22

2.2 Measurement of reaction times and decision accuracies 23

2.3 Drift-diffusion model 25

2.4 Structural imaging 26

2.5 Antibody preparation 26

2.6 Western blotting 27

2.7 Functional imaging 27

2.8 Electrophysiology 28

2.9 Statistics 32

3. Results **33**

3.1 Biophysics of FoxP-positive and FoxP-negative Kenyon cells 33

3.2 FoxP represses *Shal* in $\alpha\beta_c$ KCs 40

3.3 FoxP, Shal, and synaptic integration 43

3.4 FoxP, Shal, and reaction times 46

3.5 Neurometric functions based on first spikes 49

4. Discussion **56**

4.1 Control of *Shal* expression by FoxP 56

4.2 Biophysics of neuronal dendrites 57

4.3 Neural mechanisms of decision-making 61

References **66**

Figures

Figure 1. Drift-diffusion model of decision-making. 13

Figure 2. Neural circuit architectures of decision models. 15

Figure 3. Neural circuit architectures of olfactory systems. 18

Figure 4. *FoxP*-mutant flies have increased reaction times in an olfactory discrimination task. 20

Figure 5. Expression patterns of GAL4 lines. 22

Figure 6. *Drosophila* FoxP isoforms. 33

Figure 7. FoxP regulates the responsiveness of $\alpha\beta_c$ KCs to sensory stimulation. 34

Figure 8. FoxP does not affect maximal GCaMP6m signals in KCs. 35

Figure 9. Morphology of $\alpha\beta_c$ KCs. 36

Figure 10. FoxP does not alter synaptic transmission onto $\alpha\beta_c$ KCs. 37

Figure 11. FoxP regulates the intrinsic excitability of $\alpha\beta_c$ KCs. 38

Figure 12. FoxP does not regulate the intrinsic excitability of α'β' KCs. 39

Figure 13. FoxP alters the current-spike frequency function of $\alpha\beta_c$ KCs but not of α'β' KCs. 39

Figure 14. FoxP influences the action potential waveform of $\alpha\beta_c$ KCs. 40

Figure 15. FoxP represses an A-type potassium current in $\alpha\beta_c$ KCs. 41

Figure 16. A-type potassium currents of $\alpha\beta_c$ KCs show pharmacological characteristics of Shal. 42

Figure 17. Somatodendritic localization of Shal in in $\alpha\beta_c$ KCs. 43

Figure 18. FoxP tunes the integrative properties of $\alpha\beta_c$ KCs. 44

Figure 19. Comparison of stimulus-evoked and miniature EPSCs in $\alpha\beta_c$ KCs. 45

Figure 20. Integrative properties of α'β' KCs. 45

Figure 21. FoxP influences the EPSP waveform of $\alpha\beta_c$ KCs. 46

Figure 22. Shal currents in $\alpha\beta_c$ KCs determine reaction times. 47

Figure 23. Bidirectional manipulations of Shal currents in $\alpha\beta_c$ KCs. 48

Figure 24. The first odour-evoked spikes of $\alpha\beta_c$ KCs predict behavioural performance. 50

Figure 25. Discrimination between a high and a negatively reinforced lower odour concentration. 52

Figure 26. Spike metrics of $\alpha\beta_c$ KCs are robust under changes of odour stimulus waveform. 53

Figure 27. Odour responses of α'β' KCs. 54

Figure 28. Proposed mechanism: FoxP represses *Shal* to regulate dendritic signal propagation. 58

Tables

Table 1. Sample sizes for behavioural measurements in Figure 22. 48

Table 2. Sample sizes for neurometric measurements in Figure 24g. 51

Table 3. Sample sizes for behavioural measurements in Figure 25b. 52

Abbreviations

$\alpha\beta_c$ KC	αβ core Kenyon cell
α'β' KC	α'β' Kenyon cell
AL	Antennal lobe
ANOVA	Analysis of variance
APL	Anterior paired lateral neuron
ATP	Adenosine triphosphate
CCD	Charge-coupled device
C_m	Membrane capacitance
DN	Dominant negative
DNA	Deoxyribonucleic acid
EGTA	Ethylene glycol-bis(2-aminoethylether)-N,N,N′,N′-tetraacetic acid
eEPSC	Evoked excitatory post synaptic current
EPSC	Excitatory post synaptic current
EPSP	Excitatory post synaptic potential
FoxP	Forkhead box P transcription factor
FoxP-PC	FoxP protein isoform C
FoxP-RC	FoxP mRNA isoform C
FoxP-RD	FoxP mRNA isoform D
GABA	γ-aminobutyric acid
GC	Granule cell
GFP	Green fluorescent protein
GTP	Guanosine-5'-triphosphate
HEPES	4-(2-hydroxyethyl)-1-piperazineethanesulfonic acid
IgG	Immunoglobulin G
KC	Kenyon cell
K_V	Voltage-gated potassium channel
LED	Light-emitting diode
LH	Lateral horn
LIP	Lateral intraparietal
LN	Local neuron
MBON	Mushroom body output neuron

MCH	4-methylcyclohexanol
mEPSC	Miniature excitatory post synaptic current
M_r	Molecular mass (relative)
mRNA	Messenger ribonucleic acid
M/T	Mitral/tufted cell
MT	Middle temporal
NA	Numerical aperture
ORN	Olfactory receptor neuron
PBS	Phosphate-buffered saline
PCR	Polymerase chain reaction
PG	Periglomerular cell
PID	Photoionization detector
PN	Antennal lobe projection neuron
PVDF	Polyvinylidenfluorid
qPCR	Quantitative polymerase chain reaction
R_m	Membrane resistance
RNA	Ribonucleic acid
RNAi	Ribonucleic acid interference
SDS-PAGE	Sodium dodecyl sulfate polyacrylamide gel electrophoresis
s.e.m.	Standard error of the mean
Shal	Shaker cognate l
TES	N-[Tris(hydroxymethyl)methyl]-2-aminoethanesulfonic acid
TRAP	Translating ribosome affinity purification
TTX	Tetrodotoxin
UAS	Upstream activating sequence
VDRC	Vienna *Drosophila* Recource Centre
V_m	Membrane potential
WT	Wild-type

Throughout the text, nucleotides (genes and mRNA) are referred to in italics, proteins in roman type.

"I have chosen to discuss the problem of temporal integration here, not with the expectation of offering a satisfactory physiological theory to account for it, but because it seems to me to be both the most important and also the most neglected problem of cerebral physiology."

— Karl S. Lashley (1951)

1 Introduction

1.1 Temporal integration and the neural basis of decision-making

In his essay 'The Problem of Serial Order in Behavior', the psychologist Karl Lashley highlighted the ubiquity of brain processes that unfold over time. All processes that cannot be explained by the mere succession of external stimuli require temporal integration. As examples, Lashley lists leg movements in insects, birdsong, action planning, and human language (Lashley, 1951).

Temporal integration is key also to the cognitive process of decision-making because the information required to commit to a choice is rarely available all at once but must be gathered sequentially. Simple two-choice perceptual tasks have proven instrumental in studying the formation of a decision because they allow the experimenter to control meticulously the strength of sensory evidence and measure the behavioural consequences. A wealth of literature stretching back to the 19th century documents variations in the speed of perceptual judgments as a function of stimulus strength (Donders, 1869; Gold and Shadlen, 2007; Link and Tindall, 1971; Vickers, 1970): easy decisions, informed by clear-cut sensory evidence, tend to be fast, while difficult decisions, based on weak or ambiguous data, tend to be slow. The relationship between difficulty and decision time likely reflects the need to construct time-averaged sensory representations. Just like an engineer averages signals over time to reduce the effects of contaminating noise, the brain appears to improve its signal-to-noise ratio by integrating sequential samples of sensory information over time. In the absence of noise, the amount of information required to commit to one of two possible choices is small; in fact, the brain needs to extract only one bit of information: 1 or 0, larger or smaller, up or down. In less ideal circumstances, information about a sensory event x (e.g. up or down) can only be obtained by measuring a related variable y (e.g. concentration).

In nervous systems, the activity of sensory neurons often represents a filtered version of y, varying in time, with Gaussian noise limiting the amount of extractable information (Tkacik and Bialek, 2016). By integrating repeated measures of y, the brain achieves a reduction in entropy, or an increase in confidence about the underlying state of x. The timescale over which this process takes place (for perceptual decisions typically hundreds of milliseconds to seconds) separates the perceptual decision from the duration of the sensory event itself. This 'freedom from immediacy' is considered a hallmark of cognition (Shadlen and Kiani, 2013). The exact neural mechanisms that underlie the temporal integration of evidence in perceptual decision-making, and other time-dependent cognitive processes such as those cited by Lashley, remain unknown (Goel and Buonomano, 2014; Gold and Shadlen, 2007; Lashley, 1951; Shadlen and Kiani, 2013).

Most accounts of how the brain performs temporal integration in the context of perceptual decision-making have focused almost exclusively on evolving patterns of spiking (i.e. suprathreshold) neural activity. Limited by recording techniques, these studies have examined spike rates of single neurons during two-alternative forced-choice discrimination tasks, most commonly discriminations of visual motion (Newsome et al., 1989) or vibrotactile frequency (Mountcastle et a., 1990).

In a visual random-dot motion task, for example, the experimental subject is presented with an array of moving dots on a computer screen and has to indicate, as quickly and as accurately as possible, the direction of coherent dot motion (the 'signal') masked by a fluctuating pattern of randomly moving dots ('noise'). The difficulty of the task can be titrated from easy to near psychophysical threshold by varying the fraction of coherently moving dots (the signal-to-noise ratio). In monkeys performing this type of task, individual neurons in different areas of the brain exhibit spike rate dynamics that correlate not only with the quality and strength of the noisy stimulus (Britten et al., 1992; Newsome et al., 1989) but also the animal's behavioural judgement (Shadlen and Newsome, 2001), as reflected in the motor response communicating the choice (Hanes and Schall, 1996). In the middle temporal (MT) visual area, for example, the nature of a noisy stimulus (e.g. leftward vs. rightward motion of dots) can be decoded efficiently by comparing spike counts of a single pair of direction selective neurons tuned to leftward and rightward motion, 'neuron' and 'antineuron', respectively (Britten et al., 1992). These neurons are thought to provide sensory evidence of visual motion, moment by moment, to some downstream integrator. Equivalent to the presentation of additional evidence, microstimulation of a cluster of MT

neurons with similar direction selectivity biases the monkey's choices towards the preferred direction of these neurons (Salzman et al. 1990) leading to more and faster decisions in this direction (Hanks et al., 2006).

Conversely, stimulation of the lateral intraparietal (LIP) area, which is thought to receive input from MT neurons and could potentially act as an integrator of momentary visual evidence, has only modest effects on choice accuracies and reaction times (Hanks et al., 2006). The mean spike rates of LIP neurons appear to gradually increase or decrease during the evolution of a decision in a visual discrimination task, as if representing the relative evidence accrued in favour of one of two options (Brunton et al., 2013; Huk and Shadlen, 2005; Latimer et al., 2015; Shadlen and Newsome, 2001). Although the spiking activities of LIP neurons seem to reflect the animal's confidence and psychophysical performance with striking fidelity, their causal involvement is questionable, as acute pharmacological inactivation of the LIP area has no measurable effect on the animal's decision-making behaviour (Katz et al., 2016). These and other recent experiments (Yates et al., 2017) suggest that the complex, decision-correlated activity patterns of LIP neurons parallel, rather than constitute, the integration of visual evidence. Both the site and the neuronal mechanisms of temporal integration during perceptual discriminations therefore remain open questions.

1.2 Drift-diffusion models of decision-making

The question of a biological substrate notwithstanding, searches for a theory that formalizes the cognitive process of decision formation have generated mathematical models derived from sequential analysis and signal detection theory that capture all psychophysical aspects of perceptual decisions (Bogacz et al., 2006; Gold and Shadlen, 2007). Behavioural data from different experimental paradigms support the idea of bounded evidence accumulation, a form of temporal integration (Hanes and Schall, 1996; Palmer et al., 2005; Shadlen and Newsome, 2001). According to this framework, independent samples of sensory evidence are gradually summed up to a certain critical amount; once this threshold is met, a motor response is initiated. This operation involves A) the maintenance of evidence accrued so far in the form of a (short-term) memory and B) the addition of new pieces of evidence to the memory. Based on this concept, so-called drift-diffusion models of decision-making (Figure 1) (Bogacz et al., 2006; Ratcliff, 1978) have been developed to predict accuracies and reaction times in perceptual discrimination tasks for different sensory modalities and in different species (Brunton et al., 2013; DasGupta et al., 2014; Palmer et al., 2005;

Ratcliff et al., 2003; Ratcliff and McKoon, 2008). Drift-diffusion-based models are also the most widely and successfully used formalisms to model psychophysical performance. A comprehensive analysis of six distinct, commonly used formalisms has found that five of them can be reduced to a simple diffusion process (Bogacz et al., 2006), suggesting that an analogous mechanism could be implemented within a brain (Gold and Shadlen, 2002).

Drift-diffusion models assume that the evolution of a decision involves the deterministic temporal integration of sensory evidence as well as random fluctuations (Figure 1a). The difference in evidence favouring one alternative over the other (a.k.a. the 'decision variable') is represented in the form of a one-dimensional random walk in time with a difficulty-dependent bias or drift and added Gaussian diffusion noise (with zero mean and variance σ^2). The drift rate v is related to the difficulty x of the perceptual discrimination. The decision process terminates once the decision variable reaches one of two symmetrical decision criteria (a.k.a. 'bounds' located at $\pm A$ in Figure 1a). Solving the first-passage problem for the decision variable (i.e. the probability of the decision variable reaching a specified bound at a specified time) yields the analytical expressions in Equations (1) and (2) that link accuracy (fraction of correct choices, F_x) and reaction time T_x to task difficulty x, bound height A, and residual time T_0 (Bogacz et al., 2006):

Accuracy: $$F_x = \frac{1}{1+e^{-2A\frac{v_x}{\sigma^2}}} \quad (1)$$

Reaction time: $$T_x = \frac{A}{v_x}\tanh\left(A\frac{v_x}{\sigma^2}\right) + T_0 \quad (2)$$

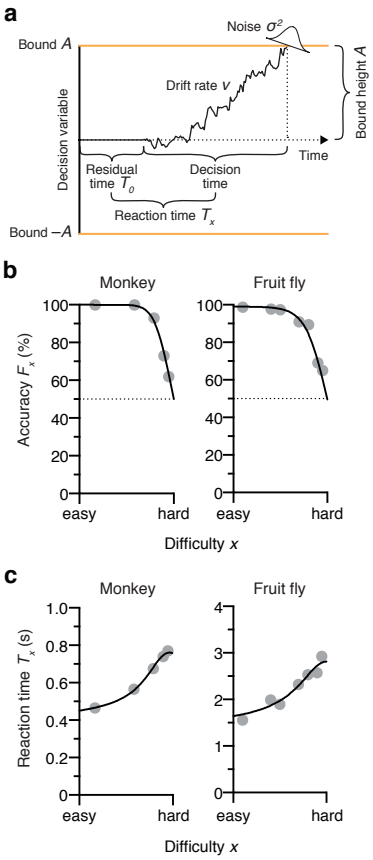


Figure 1. Drift-diffusion model of decision-making.
a, Example of a random walk illustrating the accumulation of evidence over time. Starting at a neutral point, evidence in favour of option *A* or option *–A* accumulates as a function of time, approaching a critical amount (bound *A* or *–A*). Commitment to one of the choices occurs once the difference in evidence (decision variable) reaches the respective bound. The decision variable evolves under the influences of difficulty-dependent drift *v* and diffusion noise with the variance σ^2. The reaction time T_x is composed of the actual decision time and a residual time T_0 consisting of motor latencies. **b**, Accuracy as a function of task difficulty in a visual discrimination task for monkeys (left) and an olfactory discrimination task for fruit flies (right). Data are means ± s.e.m.; error bars are masked by the symbols. Lines are drift-diffusion-based fits to experimental data and were obtained using Equation (1). **c**, Reaction time as a function of task difficulty in monkeys (left) and fruit flies (right). Data are means ± s.e.m.; error bars are masked by the symbols. Lines are drift-diffusion-based fits obtained using Equation (2). Experimental data (**b**, **c**) are from DasGupta et al., 2014 and Palmer et al., 2005, reprinted with permission from AAAS and ARVO, respectively.

The residual time T_0 is a constant independent of evidence accumulation and includes mostly motor latencies associated with the indication of the choice by the experimental subject. This experimentally-constrained offset is a prerequisite for inferring temporal relations between neurophysiological and behavioural measurements.

The beauty of this type of model lies in the fact that it accounts for the accuracies F_x and the reaction times T_x of behavioural decisions, while preserving the empirically observed trade-off between the two: lowering the bound height A reduces both the reaction time T_x and the accuracy F_x. Fitting the model parameters v, A and T_0 (Figure 1a) to the empirically measured reaction times of an experimental subject is sufficient to allow quantitative predictions about the subject's accuracy (Roitman and Shadlen, 2002; Shadlen and Kiani, 2013). Equations (1) and (2) provide excellent fits to psychometric data from species as distantly related as monkeys and fruit flies (Figure 1b, c) (DasGupta et al., 2014; Palmer et al., 2005), supporting the notion of a stereotypic mechanism, conserved across phyla and sensory modalities, that implements the bounded integration of sensory information over time.

1.3 Neural network architectures of decision-making

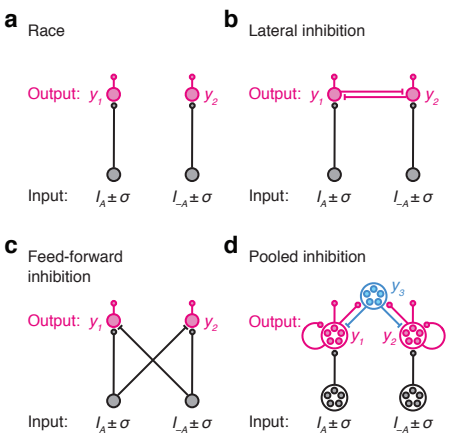
The current lack of comprehensive anatomical knowledge about the circuitry underlying any decision-related activity leaves plenty of room for models to implement the accumulation of sensory evidence using artificial neural networks. Different variations of four main architectures (Figure 2) (Bogacz et al., 2006) have been proposed, all of which fulfil the functional criteria required to map the bounded accumulation of evidence onto a neuronal medium—at least *in silico*.

The 'race model' (Figure 2a), instead of computing the difference in activity between two choice-selective neuronal populations (i.e. a 'decision variable'), assumes two separate neural integrators (y_1 and y_2) that accumulate noisy evidence in favour of option A or $-A$, respectively (Vickers, 1970). As soon as the activity of one of the integrators breaches a set threshold, a behavioural response is elicited.

In the 'lateral inhibition model' (Figure 2b) the two integrators are leaky and mutually inhibit each other, with two important consequences: First, only a difference between the two inputs I_A and I_{-A} is integrated; if I_A and I_{-A} change in the same direction, lateral inhibition between the integrators y_1 and y_2 will cancel each other out. Second, this simple circuit architecture of mutual inhibition enables a group of neurons (e.g. y_1 in Figure 2b) to provide

itself with positive feedback through self-disinhibition via its counterpart (y_2). This indirect self-excitation is sufficient to compensate for the leak and allows for the integration time constants of the neural network to assume values 1000 times greater than the intrinsic time constant of an individual neuron (Cannon et al., 1983; Usher and McClelland, 2001). In the 'feed-forward inhibition model' (Figure 2c) the integrators are perfect (i.e. not leaky) and receive opposing inhibition through crossed inputs from downstream neurons (Shadlen and Newsome, 2001). Both models, through inhibition, achieve a comparison of spike rates between two neuronal populations, yielding an arbitrary decision variable. However, both the lateral and the feed-forward inhibition model would require additional units, differential release of excitatory and inhibitory neurotransmitters, or differential expression of receptors. A more naturalistic model of 'pooled inhibition' (Figure 2d) simulates individual neurons within pools of choice-selective, recurrently interconnected neuronal populations that maintain activity through self-excitation and receive global inhibition by a population of inhibitory interneurons (y_3 in Figure 2d). Here, the numerical ratios of the respective neuronal pools and the individual neurons' biophysical properties were matched, as far as possible, to anatomical and physiological data from cortical regions (Wang, 2002). Yet, precisely defined relationships between neural network models, mathematical models of sequential sampling (drift-diffusion or race models) and any tangible biological nervous system are still elusive (Bogacz et al., 2006). The genetic, cellular and temporal resolution currently achievable by the physiological techniques used to study the neural basis of visual decision-making in rodents and primates are not yet sufficient to provide a mechanistic understanding of the underlying circuitry.

Figure 2. Neural circuit architectures of decision models.
a, Race model: Two independent neural integrators (y_1 and y_2, red) accumulate noisy input in favour of option A or $-A$ ($I_A \pm \sigma$ or $I_{-A} \pm \sigma$) until one of them reaches a threshold. **b**, Lateral inhibition: y_1 indirectly excites itself by self-disinhibition through y_2 and vice versa. In this way, only a difference between I_A and I_{-A} is integrated, if I_A and I_{-A} change by the same value, mutual inhibition between y_1 and y_2 will hold the balance. **c**, Feed-forward inhibition: Here, y_1 and y_2 are perfect integrators receiving excitation via their cognate input and inhibition via the opposing input. **d**, Pooled inhibition: Individual cells within pools of recurrently connected neurons (y_1 and y_2) maintain activity through self-excitation and receive global inhibition via a population of inhibitory interneurons (y_3, blue). Small circles denote excitatory synapses and flat lines denote inhibitory connections. Figure adapted from (Bogacz et al., 2006).



The olfactory system, with its shallow organizational structure (see below), provides a favourable contrast to the complexity of other sensory circuits. Several groups have therefore begun to study olfactory decision-making behaviour in mice, rats and fruit flies (Abraham et al., 2004; DasGupta et al., 2014; Rinberg et al., 2006; Uchida and Mainen, 2003). Like mammals, fruit flies take longer to commit to difficult olfactory choices than to easy ones, and the same quantitative relationships, formalized by drift-diffusion models, can be employed to link speed, accuracy, and difficulty of odour discriminations (Figure 1b, c) (DasGupta et al., 2014). This points to the presence of a decision-making circuit that integrates olfactory information within the brain of the fruit fly *Drosophila melanogaster*.

1.4 Architecture of an olfactory system

Olfactory discriminations start with the interaction of odorant molecules with olfactory receptors. These are found on the dendrites of olfactory receptor neurons (ORNs) within the olfactory epithelium in the nasal cavity of mammals or inside chemosensory protrusions, so-called sensilla, on the antennae and maxillary palps of the fruit fly (Figure 3) (Hildebrand and Shepherd, 1997). The anatomical difference is important because it dictates the way of sampling odour plumes and the time taken to do so: Reaction times of vertebrates are heavily influenced by the respiratory cycle (Uchida and Mainen, 2003), whereas insects typically sample their olfactory environment by rapid movements of their antennae (Huston et al., 2015), liberating them from the temporal constraints imposed by active ventilation.

Upon contact with peripheral olfactory organs, volatile odour molecules, aided by odorant-binding proteins, transition from the gaseous to the liquid phase (lymph or mucus) surrounding ORN dendrites (Pikielny et al., 1994). Once solubilized, odorants bind to olfactory receptors, much like neurotransmitters bind to their postsynaptic receptors, an interaction defined by the stereochemistry of each odour molecule. Olfactory receptors are of the G-protein-coupled family in mammals (Buck and Axel, 1991) and ionotropic in flies (Sato et al., 2008; Wicher et al., 2008); activation of either receptor type by its odorant ligand leads to an increase, or (less often) a decrease in spike rates (Hallem et al., 2004) riding on a background rate of approximately 8 Hz (Bhandawat et al., 2007). An individual ORN expresses only a limited repertoire of olfactory receptor genes, one of which defines the neuron's odour selectivity (Clyne et al., 1999; Goldman et al., 2005; Vosshall et al., 1999). Many olfactory receptors are broadly tuned and bind multiple, structurally similar odorants with different affinities in a concentration-dependent manner (Hallem and Carlson,

2006; Raman et al., 2010). ORNs expressing the same functional olfactory receptor gene are distributed randomly within zones on primary olfactory organs, yet their axons converge with remarkable precision onto a well confined region in the olfactory bulb or antennal lobe of vertebrates and fruit flies, respectively: a glomerulus (Gao et al., 2000; Ressler et al., 1994; Vassar et al., 1994; Vosshall et al., 2000).

This basic circuit architecture (Figure 3a, b) can be found in organisms widely separated in complexity and evolutionary time; the difference is merely one of scale: approximately 1500 glomeruli in the mouse correspond to ~50 in the fruit fly (Hildebrand and Shepherd, 1997). Fifty glomeruli, however, are sufficient to account for an enormous number of possible glomerular response patterns (Ng et al., 2002) that enable a fly to discriminate even between very similar odours (Parnas et al., 2013).

Each glomerulus of the fly antennal lobe is composed of neuropil from three types of neuron: ORNs (~1500 per lobe), projection neurons (PNs, ~160 per lobe) and local neurons (LNs, ~100 per lobe). ORNs provide excitatory input to both LNs and PNs, the vertebrate homologues of which are periglomerular and granule cells and mitral and tufted cells, respectively (Figure 3a, b) (Wilson and Mainen, 2006). Lateral inhibition and excitation by different classes of LNs adjusts the basal activity and the gain of PNs to varying concentrations of background odours (Olsen et al., 2010; Olsen and Wilson, 2008; Shang et al., 2007). Most PNs receive inputs from ORNs innervating a single, distinct glomerulus defined by its cognate olfactory receptor and send axonal projections to third-order olfactory neurons in the mushroom bodies and the lateral horns of the protocerebrum (Figure 3b) (Jefferis et al., 2001; Marin et al., 2002). The latter, innervated by both excitatory and inhibitory PNs in a stereotypic fashion (Fisek and Wilson, 2014), are implicated in innate odour-guided behaviours (Heimbeck et al., 2001; Parnas et al., 2013). The mushroom bodies, on the other hand, are required for associative olfactory learning and memory (de Belle and Heisenberg, 1994; Heisenberg et al., 1985; Keene and Waddell, 2007). Here, the afferent ‘labelled lines’ are reorganized in a seemingly random fashion as they connect to Kenyon cells (KCs), the mushroom bodies’ intrinsic neurons (Caron et al., 2013; Murthy et al., 2008) homologous to the pyramidal neurons of the vertebrate piriform cortex (Figure 3). Lining the superficial layer of the posterior, dorsal brain, approximately 2000 KCs per hemisphere each extend a single neurite to the calyx, the dendritic region of the mushroom body, where they receive excitatory input from cholinergic PNs and global inhibition from one giant GABAergic anterior paired lateral neuron (APL) per hemisphere (Figure 3b) (Lin

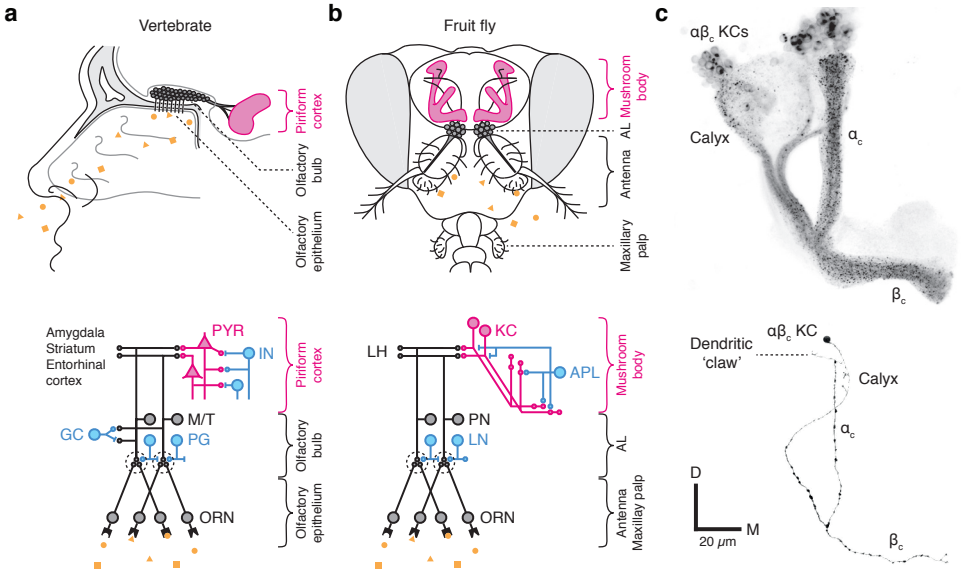


Figure 3. Neural circuit architectures of olfactory systems.
a, Simplified schematic of the vertebrate olfactory system at macroscopic (top) and cellular resolution (bottom). Odorant molecules (orange) bind to olfactory receptors on the dendrites of olfactory receptor neurons (ORNs). ORNs with the same olfactory receptor are distributed randomly in the olfactory epithelium, but their axons converge onto one or two clearly demarcated glomeruli (dashed circles) in the olfactory bulb. Periglomerular (PG) and granule cells (GC) provide lateral inhibition. Mitral and tufted (M/T) cells send axonal projections to the piriform cortex (red) and other brain regions, where the labelled lines are lost in seemingly random connectivity between M/T cells, pyramidal neurons (PYR) and inhibitory interneurons (IN). **b**, Simplified schematic of the fruit fly olfactory system at macroscopic (top) and cellular resolution (bottom). The axons of ORNs expressing the same receptor gene converge onto a confined glomerulus (dashed circles) in the antennal lobe (AL). Local neurons (LNs) provide lateral excitation and inhibition. Projection neurons (PNs) send axonal projections to the lateral horn (LH), and the mushroom body, where the labelled lines are lost in seemingly random connectivity between PNs and Kenyon cells (KCs). KCs receive global inhibition via a large inhibitory interneuron (APL). First- and second-order olfactory neurons are shown in black, third-order neurons in red and inhibitory neurons in blue; dashed lines denote glomerular units. For clarity, some synaptic and electrical connections including excitatory LNs and their possible vertebrate homolog short axon cells are not shown. **c**, Maximum intensity projection of confocal stacks spanning the right mushroom body of a fly expressing *UAS-6×GFP* in $\alpha\beta_c$ KCs under the control of *NP7175-GAL4* (top) and corresponding micrograph of a single, biocytin-filled $\alpha\beta_c$ KC (bottom). α_c, vertical α lobe and β_c, horizontal β lobe comprising axons of $\alpha\beta_c$ KCs; D, dorsal; M, medial.

et al., 2014; Papadopoulou et al., 2011). Individual KCs elaborate between 2 and 11 claw-shaped postsynaptic sites clasping the presynaptic boutons of excitatory PNs (Caron et al., 2013; Gruntman and Turner, 2013). In contrast to the broad combinatorial representation of odours by the antennal lobe, activity at the KC level is sparse, both spatially and temporally, with no more than 5-10% of cells discharging only a few spikes in response to any given odour (Ito et al., 2008; Lin et al., 2014; Turner et al., 2008). KC axons project to the anterior brain where γ KCs extend as a single horizontal lobe, while the projections of αβ and α'β'

neurons bifurcate to form a vertical α and a horizontal β lobe per hemisphere (Figure 3c). Based on morphology, clonal origin, and specific genetic labels, αβ KCs can be subdivided further into αβ core ($\alpha\beta_c$), αβ surface and αβ posterior neurons (Tanaka et al., 2008). In anatomically confined compartments of the mushroom body's lobes, ~2000 KCs converge numerically onto only 34 mushroom body output neurons (MBONs; Aso et al., 2014a) exciting them through cholinergic transmission (Barnstedt et al., 2016).

MBONs, whose activation *per se* is not sufficient to trigger motor responses (Aso et al., 2014b), connect the mushroom bodies to downstream regions of the central complex involved in the coordination of locomotor activity (Strauss, 2002), and form interconnections of different signs between individual mushroom body compartments (Aso et al., 2014a), possibly providing GABAergic or glutamatergic (Liu and Wilson, 2013) lateral inhibition and cholinergic recurrent excitation (Aso et al., 2014b). The mushroom body is innervated also by ~130 dopaminergic neurons, which assign valence to a specific odour stimulus by depressing synaptic connections between KCs and MBONs during associative learning (Claridge-Chang et al., 2009; Hige et al., 2015; Séjourné et al., 2011). When an odour coincides with punishment, dopaminergic neurons innervating the vertical α lobes get activated alongside an odour-specific subset of KCs, causing long-term depression of the synapses connecting the activated KCs to MBONs. Upon subsequent exposure to the odour, MBONs with dendrites in the β lobes will now receive stronger input than their α lobe counterparts, triggering aversive behaviour. Conversely, appetitive conditioning (e.g. using the same odour as the conditioned stimulus) depresses output from the β lobes and will trigger approach (Aso et al., 2014a; Owald et al., 2015). Odour identity is encoded in the form of sparse activity across the KC population (Lin et al., 2014; Turner et al., 2008); valence is assigned to this odour-evoked activity pattern at mushroom body output synapses (Séjourné et al., 2011).

Fruit flies can learn to differentiate between pairs of distinct odours (Quinn et al., 1974), two overlapping blends of odours (Campbell et al., 2013), or two different concentrations of one and the same odour (DasGupta et al., 2014). The difficulty-dependence of the flies' reaction times in such an odour discrimination task (Figures 1b, c, and 4) (DasGupta et al., 2014), suggests that a temporal integrator of sensory information is present somewhere within the olfactory system of the fruit fly.

1.5 FoxP influences the speed of olfactory decisions

A crucial hint to the identity of a putative integrator within the fly's olfactory system came from the discovery that a small, genetically distinct population of $\alpha\beta_c$ KCs (Aso et al., 2014a; Tanaka et al., 2008), is a critical determinant of reaction time (Figure 4c) (DasGupta et al., 2014). The decision-relevant neurons encompass just ~80 out of the ~2000 KCs per hemisphere of the fly brain and are distinguished by the expression of the forkhead box P transcription factor (FoxP) (DasGupta et al., 2014), an ancestral member (Santos et al., 2011) of a transcription factor family of considerable interest in molecular and developmental neurobiology (Konopka et al., 2009; Sia et al., 2013; Vargha-Khadem et al., 1995), cognitive science (Hamdan et al., 2010; Vargha-Khadem et al., 1995), linguistics (Lai et al., 2001; Vargha-Khadem et al., 1995), and evolutionary anthropology (Enard et al., 2002; Konopka et al., 2009). The neuronally expressed vertebrate orthologues of *FoxP*,

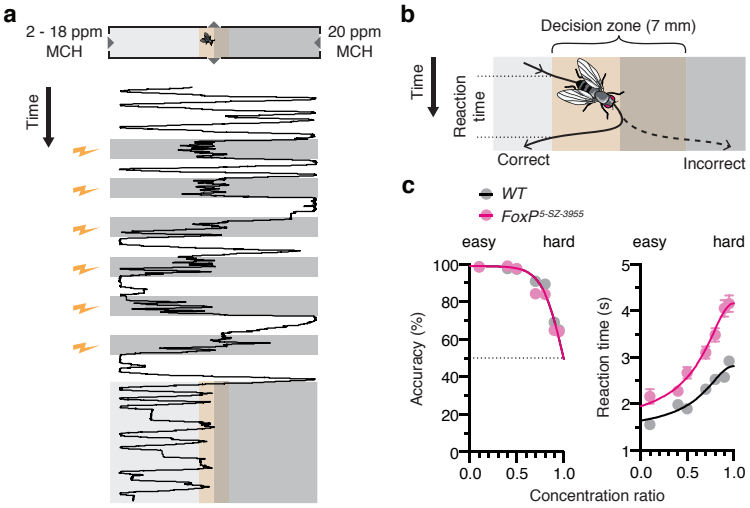


Figure 4. *FoxP*-mutant flies have increased reaction times in an olfactory discrimination task.
a, Measurement of decision accuracies and reaction times. Two odour streams converge in a 7-mm wide decision zone (orange) at the centre of a narrow chamber (top). Position of an exemplary fly within the chamber (horizontal dimension) as a function of time (vertical dimension) during training and testing. Flies are trained to avoid a specific concentration of MCH (20 ppm, grey) using electric shock (orange lightning) and must discriminate the reinforced from a lower MCH concentration (2–18 ppm); the concentration ratio during testing determines the difficulty of the task. **b**, The accuracy of a decision is determined by which side of the chamber the fly exits the decision zone and the time spent inside the decision zone is quantified as the reaction time. **c**, Flies with a homozygous loss-of-function mutation in the *FoxP* gene (*FoxP*$^{5\text{-}SZ\text{-}3955}$) take longer than wild-type (*WT*) flies to form decisions of similar accuracy. Experimental data in panel (**c**) are from (DasGupta et al., 2014), reprinted with permission from AAAS.

including human *FOXP1* and *FOXP2*, play critical roles in cognition (Hamdan et al., 2010; Vargha-Khadem et al., 1995), vocal communication (Haesler et al., 2007; Lai et al., 2001; Sia et al., 2013), and the replay of learned motor sequences (Aso et al., 2014a; Groszer et al., 2008)—all examples of temporal processing cited by Lashley (Lashley, 1951).

Drosophila FoxP mutants take longer than wild-type flies to make odour intensity discriminations of similar accuracy (Figure 4c) (DasGupta et al., 2014), suggesting that the process evidence accumulation within their olfactory system is impaired. Promising neuronal candidates that might account for this process are the *FoxP*-expressing $\alpha\beta_c$ KCs. Here I study the mechanism of sequential sampling through the lens of the *FoxP* mutation: I identify how FoxP shapes the temporal information-processing capabilities of $\alpha\beta_c$ KCs and relate these capabilities to the olfactory choice behaviour of the animal.

Specific aims of my work are A) the identification of the neuronal substrates and the mechanisms that account for the integration of sensory evidence and B) the characterization of the functional role of FoxP in this process.

2 Methods

2.1 Fly strains and culture

Experimental flies were heterozygous for all transgenes, including *UAS-FoxP*^{RNAi} (Vienna *Drosophila* Recource Centre [VDRC] ID 15732) (Dietzl et al., 2007), and homozygous for either a wild-type (*WT*) or the mutant *FoxP*$^{5\text{-}SZ\text{-}3955}$ allele (*w*^{1118}*; P{RS}5FoxP*$^{5\text{-}SZ\text{-}3955}$, Kyoto Stock Center), as indicated. For patch-clamp recordings, *NP7175-GAL4* (Murthy et al., 2008; Tanaka et al., 2008) or *VT030604-GAL4* (VDRC ID 200228) (Kvon et al., 2014) were used to target the expression of *UAS-CD8::GFP* (Lee and Luo, 1999) to $\alpha\beta_c$ or α'β' KCs, respectively (Figure 5). In functional imaging experiments, where the α' lobe of the mushroom body could be visually identified, KC populations expressed *UAS-GCaMP6m* (Chen et al., 2013) under the control of *OK107-GAL4* (Tanaka et al., 2008) or *NP7175-GAL4* (Figures 5 and 8). To examine the subcellular distribution of Shal or the

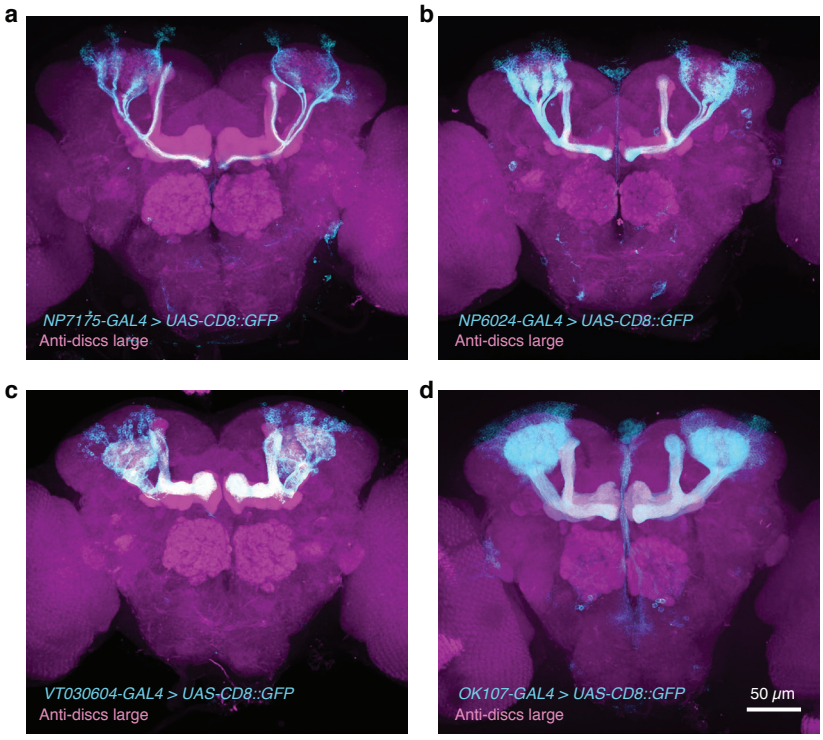


Figure 5. Expression patterns of GAL4 lines. **a–d**, Maximum intensity projections of confocal image stacks capturing the central brains of flies expressing *UAS-CD8::GFP* (cyan) under the control of *NP7175-GAL4* (**a**) or *NP6024-GAL4* (**b**) in FoxP-positive $\alpha\beta_c$ KCs; under the control of *VT030604-GAL4* in FoxP-negative α'β' KCs (**c**); or under the control of *OK107-GAL4* in all KCs (**d**). Synaptic structures were counterstained with an antibody against discs large (magenta).

behavioural consequences of altered Shal currents, the strong *NP6024-GAL4* line (Tanaka et al., 2008) was used to drive high-level expression of *UAS-GFP-Shal* (Diao et al., 2010) or *UAS-DN-Shal* (Ping et al., 2011) in $\alpha\beta_c$ KCs (Figures 22 and 23). In Figure 17, $\alpha\beta_c$ KCs coexpressed *UAS-mCherry-CAAX* (Kakihara et al., 2008); in Figure 22c, d, flies bearing *UAS-GFP-Shal* also carried *tubP-GAL80^{ts}* (McGuire et al., 2003) to enable the temperature-controlled overexpression of *Shal*. The strong *NP6024-GAL4* line (Tanaka et al., 2008) was used wherever high expression levels of transgenes and/or comprehensive targeting of the entire population of $\alpha\beta_c$ KCs were required. The more restricted, but also much weaker *NP7175-GAL4* line (Murthy et al., 2008; Tanaka et al., 2008) was used to provide specific access to a smaller, more confined population of FoxP-positive $\alpha\beta_c$ KCs (DasGupta et al., 2014).

Fly strains were cultivated on standard cornmeal agar under a 12 h light:12 h dark cycle at 25 ˚C unless they expressed GAL80^{ts}; in this case, the experimental animals and all relevant controls were raised at 18 ˚C. Adult, male flies of different ages were used in different experiments to guarantee optimal conditions: In functional imaging and behavioural experiments, where high expression levels are key to achieving reasonable signal-to-noise ratios, flies were used at 7-8 days post eclosion, when *NP7175-GAL4* and *NP6024-GAL4* show the strongest expression. Because adipose tissue surrounding the brain accumulates and the perineural sheath indurates with age, younger flies (6-24 h post eclosion) were used in whole-cell patch clamp recordings to facilitate surgical access to KC somata.
In behavioural experiments, flies were conditioned as outlined below, all other experiments assessing the function and anatomy of KCs were performed using naïve, untrained flies. This does not affect my conclusions because training through dopaminergic reinforcement modulates primarily efferent, rather than afferent, synapses of the mushroom bodies (Hige et al., 2015; Aso et al., 2014a).

2.2 Measurement of reaction times and decision accuracies

In the present study, to restrict the dimensionality of the vast ‘odour space’ at the level of KCs, I used only a single, mono-molecular odour that flies can be trained to avoid: 4-methylcyclohexanol (MCH; Quinn et al., 1974). After training, the flies had to discriminate the reinforced MCH concentration from a different concentration of the same odour (DasGupta et al., 2014). Psychometric measurements obtained with the use of MCH also apply to other odorants commonly used in olfactory conditioning experiments such

as 3-octanol as well as mixtures of MCH and 3-octanol (Claridge-Chang et al., 2009; DasGupta et al., 2014) and are likely to generalize to many mono-molecular odours and odour blends. Male flies aged 7–8 days were analyzed individually in transparent plexiglass chambers (50 mm long, 5 mm wide, 1.3 mm high) (Claridge-Chang et al., 2009; DasGupta et al., 2014). Two independently controlled odour streams entered the chambers through ports at the ends of the long chamber axis, converged at the centre, and left through lateral vents (Figures 4a and 22a). Printed circuit boards, connected via solid-state relays (Fairchild HSR312L) to a 70-V power supply, served as floors and ceilings. Filtered, flow-controlled (CMOSens, Sensirion), and humidified carrier air was mixed, in the indicated ratios, with flow-controlled odour streams drawn through vials containing 4-methylcyclohexanol (MCH), yielding a final flow rate of 0.25 l/min per half-chamber. Twenty chambers were operated simultaneously in an incubator (Sanyo MIR-154) at 25 ˚C. The chambers were backlit by 940-nm LEDs (TSAL6100, Vishay) and imaged using a Stingray F080B CCD camera (Allied Vision Technologies) with an 18-mm lens (Edmund Scientific). A virtual instrument written in LabVIEW (National Instruments) controlled the delivery of odours and electric shock and recorded the positions of the 20 flies as functions of time (Claridge-Chang et al., 2009).

Flies were trained to avoid 20 ppm MCH by pairing twelve consecutive 20-s odour presentations, which were interspersed with 20-s presentations of clean air, with 1 s of electric shock (DasGupta et al., 2014). During a 2-min testing period immediately after training, one half of each chamber was filled with MCH at the reinforced concentration while the other half was perfused with a lower concentration (2, 8, 14, or 18 ppm, respectively); the concentration ratio was titrated to determine the difficulty of the perceptual task (DasGupta et al., 2014).

Experimental data were processed offline in MATLAB (The MathWorks) (DasGupta et al., 2014). Position measurements were smoothed by computing 0.5-s moving averages and filtered to exclude animals making <2 end-to-centre runs per testing period. Each chamber contained a central, 7-mm wide decision zone (Figures 4a, b, and 22a). Correct and incorrect choices during the test period were combined into individual accuracy scores, which were used to calculate population averages. The time between entry into and exit from the decision zone was recorded as the reaction time (DasGupta et al., 2014). A fly's trajectory within the decision zone, viewed along the long chamber axis (Figures 4 a, b, and 22a), typically consisted of an entry phase at high velocity, a pause at the odour interface,

and an accelerated exit phase. Reaction times were normalized to each fly's instantaneous walking speed, estimated as the average speed from the point of entry into the decision zone to the first reduction to 10% of the entry velocity (DasGupta et al., 2014). In Figure 22c, d, all flies were kept at 31 ˚C for 40–48 h before the experiment to allow the temperature-induced overexpression of Shal.

2.3 Drift-diffusion model

In Figure 1b, c, accuracy and reaction time measurements were fit to a drift-diffusion model as described in Equations (1) and (2) (Bogacz et al., 2006). In Figures 4c and 24g, scaling factors k_i were introduced to Equations (1) and (2) (see Introduction) to relate the genotype-specific drift rates $v_{i,x}$ linearly to the difficulty x of odour intensity discrimination, which was quantified as (1–odour concentration ratio): $v_{i,x} = k_i x$. Fractions of correct choices $F_{i,x}$, were normalized by the empirically determined maximal accuracy ($F_{\max} = 0.9905$). Equations (3) and (4) relate decision accuracies $F_{i,x}$ and reaction times $T_{i,x}$ to task difficulty x and genotype i through the free parameters bound height A, residual time T_0, (Figures 1a and 24f), and the genotype-specific scaling factors k_i and noise variances σ_i^2:

$$F_{i,x} = F_{\max} \frac{1}{1 + e^{-2A\frac{k_i x}{\sigma_i^2}}} \tag{3}$$

$$T_{i,x} = \frac{A}{k_i x} \tanh\left(A \frac{k_i x}{\sigma_i^2}\right) + T_0 \tag{4}$$

For the accuracy of the model to become independent of the genotype (as observed experimentally in Figure 4c) (DasGupta et al., 2014), the noise variances σ_i^2 must be proportional to the corresponding scaling factors k_i, i.e. $k_i = c\,\sigma_i^2$ where c is a constant. Then Equations (3) and (4) simplify to:

$$F_x = F_{\max} \frac{1}{1 + e^{-2A'x}} \tag{5}$$

$$T_{i,x} = \frac{A'}{k_i' x} \tanh\left(A' x\right) + T_0 \tag{6}$$

In Equations (5) and (6), A' and k'_i are the scaled parameters defined as $A' = c\,A$ and $k'_i = c\,k_i$.

The free parameters A', k'_{WT}, k'_{FoxP}, and T_0 were estimated from a simultaneous least-squares fit, computed with the help of the Nelder-Mead simplex algorithm implemented in MATLAB, of accuracy and reaction time data of wild-type and $FoxP^{5\text{-}SZ\text{-}3955}$ mutant flies (DasGupta et al., 2014) to Equations (5) and (6). The model returned a residual time T_0 of 1.296 s, a bound height A' of 4.383, and genotype-specific scaling factors k'_i of 12.659 for wild-type and 6.704 for $FoxP^{5\text{-}SZ\text{-}3955}$ mutant flies. The units of A and k'_i are arbitrary. The ratio of noise variances between $FoxP^{5\text{-}SZ\text{-}3955}$ mutant and wild-type flies was computed as the ratio of the corresponding k'_i parameters, because k'_i are proportional to σ_i^2.

2.4 Structural imaging

Brains of male flies were dissected 2 days after eclosion and mounted in phosphate-buffered saline (PBS; 137 mM NaCl, 3 mM KCl, 8 mM Na_2HPO_4, 1.5 mM KH_2PO_4, pH 7.3) for imaging native fluorescence (Figures 3c, 7b, and 17). For immunostainings (Figure 5), dissected brains were fixed in 4% (w/v) paraformaldehyde in PBS for 20 min at room temperature, washed four times for 20 min in PBS, and permeabilized and blocked in PBS containing 0.2% (v/v) Triton X-100 and 5% (v/v) goat serum for 1 h. To label synaptic structures, the samples were first incubated with mouse monoclonal anti-discs large antibody 4F3 (Developmental Studies Hybridoma Bank, University of Iowa, 1:50) and then with Alexa Fluor 633-conjugated goat anti-mouse IgG (A-21052, Invitrogen, 1:200). Each incubation lasted for 48 h at 4 ˚C and was followed by four 20-min washes in PBS. To visualize the morphology of single biocytin-filled KCs after patch-clamp recordings (Figure 9), brains were fixed in 4% (w/v) paraformaldehyde in PBS at 4 ˚C for 18 h, washed six times for 20 min each in PBS, and permeabilized in PBS containing 0.2% (v/v) Triton X-100 for 1 h. Biocytin was detected by incubating the samples in Alexa Fluor 555-conjugated streptavidin (S32355, Invitrogen, 1:200) for 48 h at 4 ˚C, followed by 10 washes over a period of 12 h. Stained samples were mounted in Vectashield (Vector Labs) and all samples were imaged on a Leica TCS SP5 confocal microscope equipped with an HCX PL APO 40×/1.3 CS oil immersion objective (Leica). Images were processed in ImageJ.

2.5 Antibody preparation

A polyhistidine-tagged protein comprising the C-terminal 96 amino acids (425-520) of the long isoform of *Drosophila* FoxP (FoxP-PC) was produced in *Escherichia coli* BL21 (DE3), isolated from inclusion bodies, refolded, and affinity-purified by GenScript (Piscataway,

NJ). Polyclonal rabbit anti-FoxP-PC antibody was generated and affinity-purified by GenScript using a total of 5 mg of purified protein as antigen.

2.6 Western blotting

For each biological replicate, three male flies were collected at 7-8 days post-eclosion in a microcentrifuge tube. Whole-body protein extracts were obtained on ice using disposable pellet pestle tissue grinders. Each sample was solubilized in 120 µl of Laemmli sample buffer (Bio-Rad) supplemented with 5% (v/v) β-mercaptoethanol and boiled at 95 ˚C for 5 min before centrifugation at 12,000 g for 10 min at 4 ˚C to remove debris. Proteins, contained within 20 µl of each supernatant, were fractionated by sodium dodecyl sulfate polyacrylamide gel electrophoresis (SDS-PAGE) under reducing conditions and blotted onto polyvinylidenfluorid (PVDF) membranes using wet transfer conditions in 48 mM Tris, 39 mM glycine, 0.05% (v/v) SDS and 20% (v/v) methanol. Membranes were blocked for 1 h at 21 ˚C in Tris-buffered saline (pH 7.5) containing 20 mM Tris, 150 mM NaCl, 0.1% (v/v) Tween 20 (TBST) and 5% (w/v) skim milk powder. FoxP-PC was detected using custom-raised, affinity-purified rabbit anti-FoxP-PC antibody (1:2000) and peroxidase-conjugated goat anti-rabbit IgG (32260, Invitrogen, 1:5000); α-tubulin was detected using mouse monoclonal anti-α-tubulin antibody (T6199, Sigma, 1:2000) and peroxidase-conjugated goat anti-mouse IgG (32230, Invitrogen, 1:5000). Overnight-incubations with primary antibodies at 4 ˚C were followed by six 10-min washes in TBST. Incubations in secondary antibodies lasted for 2 h at 21 ˚C followed by six wash cycles. Peroxidase activity was visualised by chemiluminescence using ECL substrate (Thermo Fisher Scientific) and a CCD camera (GeneGnome XRQ, Syngene).

2.7 Functional imaging

Male flies aged 7 days were fixed to a custom mount with soft thermoplastic wax (Agar Scientific). Cuticle, adipose tissue, and trachea were surgically removed in a window large enough to expose the dorsal brain and antennal nerves, and the preparation was superfused with extracellular solution (pH 7.45) containing 5 mM HEPES, 140 mM NaCl, 2 mM KCl, 4.5 mM $MgCl_2$, and 1.5 mM $CaCl_2$. Both antennal nerves were cut as far distally as possible, and the antennae were removed to facilitate access. One nerve was aspirated into a fire-polished suction electrode (40 µm bore diameter) to achieve a 1.5 ± 0.3 MΩ seal. A constant voltage stimulator (Digitimer) was used to deliver trains of 1-ms pulses of 2 V at

increasing frequencies for 500 ms, with pauses of 20 s between stimulus trains. The pipette resistance was monitored throughout using a low-ohmic resistor and an oscilloscope (TDS 220, Tektronix) to guarantee constant stimulation currents.

GCaMP6m fluorescence was recorded by two-photon laser scanning microscopy. Excitation light pulses of 140 fs duration and a centre wavelength of 910 nm (Chameleon Ultra II, Coherent) were intensity-modulated with the help of a Pockels cell (302RM, Conoptics) and focussed by a 20×, 1.0 NA water immersion objective (W-Plan-Apochromat, Zeiss) on a Movable Objective Microscope (Sutter Instruments). Emitted photons were separated from excitation light by a series of dichromatic mirrors and dielectric and coloured glass filters and detected by a GaAsP photomultiplier tube (H10770PA-40 SEL, Hamamatsu Photonics). Photocurrents were amplified by a high-speed amplifier (HCA-4M-500K-C, Laser Components) and passed through a custom-designed integrator circuit to maximize the signal-to-noise ratio. The microscope was controlled through ScanImage (Vidrio Technologies) via a PCI-6110 DAQ board (National Instruments). Images were acquired at a resolution of 256 × 256 pixels and a frame rate of 5 Hz. All experiments were carried out at room temperature (21–23 ˚C).

$\Delta F/F$ traces in manually defined regions of interest were calculated in ImageJ by first subtracting and then dividing the fluorescence signal by the background-corrected pre-stimulus signal intensity (Lin et al., 2014). To measure the maximal GCaMP6m fluorescence, Ca^{2+} influx was induced at the end of each experiment by rapidly applying KCl to the bath at a final concentration of 100 mM (Figure 8).

2.8 Electrophysiology

For whole-cell patch-clamp recordings *in vivo*, male flies aged 6-24 h post eclosion were prepared as for functional imaging, but the perineural sheath was also removed to provide access to KC somata and the antennae and antennal nerves were left intact for measuring odour responses. The brain was continuously superfused with extracellular solution (pH 7.3) containing 5 mM TES, 103 mM NaCl, 3 mM KCl, 26 mM $NaHCO_3$, 1 mM NaH_2PO_4, 1.5 mM $CaCl_2$, 4 mM $MgCl_2$, 8 mM trehalose, 10 mM glucose, and 7 mM sucrose (275 mOsM, equilibrated with 5% CO_2 and 95% O_2). Patch pipettes (15-17 MΩ) were fabricated from borosilicate glass capillaries with outer and inner diameters of 1.5 and 0.86 mm (Sutter Instruments), using a PC-10 micropipette puller (Narishige), and filled with solution (pH 7.3) containing 10 mM HEPES, 140 mM potassium aspartate, 1 mM

KCl, 4 mM MgATP, 0.5 mM Na_3GTP, 1 mM EGTA, and 10 mM biocytin (265 mOsM). Pipettes were visually targeted to green-fluorescent KC somata using a combination of epifluorescence and differential interference contrast on an Axioscop 2 FS mot microscope (Zeiss) equipped with a 60×, 1.0 NA water immersion objective (LUMPLFLN60XW, Olympus) and an X-Cite 120PC Q light source (Excelitas Technologies). $\alpha\beta_c$ KCs labelled by *NP7175-GAL4* were considered a homogeneous population and sampled randomly, irrespective of their discernible origin from one of the four neuroblast clones that give rise to the mushroom bodies (Ito et al., 1997; Tanaka et al., 2008).

Signals were acquired at room temperature (21–23 ˚C) with a MultiClamp 700B amplifier (Molecular Devices), lowpass-filtered at 10 kHz, and sampled at 50 kHz using a Digidata 1440A digitizer controlled through pCLAMP 10 (Molecular Devices). Data were corrected for liquid junction potential (Neher, 1992) and analysed with custom procedures using the NeuroMatic package (http://neuromatic.thinkrandom.com) in Igor Pro (WaveMetrics).

In current-clamp recordings, bridge balance was used to compensate for series resistance. The most negative membrane potential recorded immediately after break-in, in the absence of a holding current and without correcting for errors introduced through seal conductances, was taken to represent the resting potential. Because of the high input resistances of KCs (Figures 11 and 12) (Turner et al., 2008), the true resting potentials are likely to be more hyperpolarized (Gouwens and Wilson, 2009). Only cells with a measured resting potential below –35 mV and a spiking response to depolarizing current injections were characterized further. Spikes were detected by finding minima in the time derivative of the membrane potential trace, which allowed the distinction of action potentials from EPSPs based on differences in the slopes of membrane repolarization. Spike thresholds and spike latencies were estimated by recording voltage responses to 600-ms current ramps, from –2 to +20 pA, starting at a membrane potential of –75 ± 2 mV. Input resistances were calculated from linear fits of the steady-state voltage changes elicited by 750-ms steps of hyperpolarizing currents (1 pA-increments, starting at –4 pA) from a pre-pulse potential of –70 ± 5 mV. Membrane time constants were determined by fitting a single exponential to the voltage deflection caused by a hyperpolarizing 2.5-pA current step lasting 750 ms. Action potential waveforms represent averages of individual, baseline-subtracted spikes recorded at membrane potentials just above threshold, when neurons fired at ≤5 Hz; EPSP waveforms represent averages of individual, baseline-subtracted EPSPs occurring spontaneously at a membrane potential of –70 ± 5 mV. Decay time constants were determined by fitting single

exponentials to the averaged EPSP waveforms. Waveforms that could not be fit adequately by an exponential function were excluded from the analysis of decay time constants.

For electrical stimulation of the antennal nerve, the amplitude of 50-µs voltage pulses delivered by a constant voltage stimulator (Digitimer) was gradually increased until EPSCs or EPSPs could be detected in the recorded KC; the stimulus intensity was then further increased by ~25% to minimize the fraction of transmission failures. Once a stable response was obtained, the stimulus intensity was left unchanged for the remainder of the experiment. Following a first set of stimulation trials at a range of frequencies, $BaCl_2$ was added to the extracellular solution at a final concentration of 150 µM, and a second set of stimulation trials was conducted; the ability of 150 µM Ba^{2+} to block Shal currents was verified in voltage-clamp recordings (Figure 16c, d). In some experiments, especially those where large stimulus amplitudes were required, a third and final set of antennal nerve stimulation trials was performed after the addition of 1 µM tetrodotoxin (TTX, Tocris) to block voltage-gated Na^+ channels and ensure that the responses of the recorded KC were synaptically mediated (Figures 18c-f and 20c, d).

For olfactory stimulation, mass flow-controlled streams of MCH-infused air (CMOSens, Sensirion) were directed at the fly's head through a behavioural chamber cut in half; flow rates matched those in behavioural experiments (0.25 l/min). Solenoid valves (The Lee Company) under LabVIEW control (National Instruments) switched between odour streams containing a variable basal (2, 8, 14, or 18 ppm, as indicated) and a constant peak (20 ppm) concentration of MCH. Steady-state odour concentrations were calibrated using a ppbRAE 3000 photoionization detector (RAE systems); the kinetics of MCH concentration changes at the position of the fly were recorded with a 200B miniPID (Aurora Scientific) at 10 kHz and smoothed with a Gaussian filter. Pressure changes caused by the opening and closing of valves were balanced with the help of a set of pressure-compensating valves and monitored periodically with a mass flow sensor (FBAL001DU, Sensor Technics). The membrane potential at the beginning of each MCH stimulation trial was –50 ± 5 mV. KCs were classified according to their spiking responses to a cyclical, high-contrast stimulus (MCH concentration ratio 0.1). 'Up' cells fired spikes during the rising phase of the stimulus; 'down' cells responded during the falling phase; 'unresponsive' cells did not show a spiking response to MCH concentration changes in either direction. Each spiking cell was assigned the response type that yielded an accuracy score of >50% (typically 98-100%) for a set of at least four presentations of the high-contrast stimulus. The response type of one KC

was consistent over multiple trials of the high-contrast stimulus, however, cells with 'up' responses to MCH were occasionally found to show 'down' responses or no response at all to other odorants. One given neuron can therefore generate the entire response spectrum depending only upon the identity of the odorant stimulus. Membrane potential variances as functions of base MCH concentration were quantified in the 5-s window immediately before stimulus onset. To quantify how the membrane potential variance differed between FoxP deficient and wild-type cells, for each cell group, the variances were averaged across the MCH concentrations, and the ratio of the averaged variances of the two groups was computed.

Voltage-clamp recordings, except those in Figures 10, 16c, d, 18b, 19 (left panels), and 20b were obtained in the presence of 1 µM TTX; because KCs lack significant Ca^{2+} currents (Gasque et al., 2005), no measures were taken to block Ca^{2+} channels. Series resistances were monitored but not compensated and allowed to rise by at most 20% over the course of a recording. Capacitative transients and linear leak currents were subtracted using a P/4 protocol. Steady-state activation parameters were determined by applying depolarizing 50-ms voltage pulses from a holding potential of –100 mV; the pulses covered the range to +50 mV in steps of 10 mV. A-type current densities were determined by dividing the peak outward current during the first 10 ms of the test pulse by the cell's capacitance. Membrane capacitances were estimated by integrating the capacitative currents produced by 10-ms steps of 20 mV and found to be identical among genotypes (P = 0.3127, Kruskal-Wallis test), averaging 2.41 ± 0.07 pF (n = 81 cells), 2.45 ± 0.07 pF (n = 49 cells), and 2.49 ± 0.06 pF (n = 42 cells) for $\alpha\beta_c$ KCs of wild-type, *FoxP*$^{5\text{-}SZ\text{-}3955}$, and *FoxP*^{RNAi} flies, respectively (means ± s.e.m.). Steady-state inactivation parameters were obtained with the help of a two-pulse protocol, in which a 500-ms pre-pulse (–120 to –30 mV in 5 mV increments) was followed by a 50-ms test pulse to +50 mV; non-inactivating outward currents, measured from a pre-pulse potential of –30 mV, were subtracted. Peak A-type currents (I_A) were normalised to the maximum current amplitude (I_{max}) of the respective cell and plotted against the pre-pulse potential (V). Curves were fit to the Boltzmann function $I_A/I_{max} = 1/(1+e^{(V-V0.5)/k})$ to determine the half-maximal inactivation voltage ($V_{0.5}$) and slope factor (k). To estimate the inactivation time constant, single exponential functions were fit to the decaying phase of currents elicited by 100-ms depolarizing voltage pulses after digitally subtracting non-inactivating outward currents. Phrixotoxin-2 (Alomone Labs) was dissolved freshly in extracellular solution at 100 µM and applied directly to the soma of

the recorded cell, using a patch pipette (3–4 MΩ) connected to a pneumatic drug ejection system (5 psi, PEDS-02DX, npi electronic).

2.9 Statistics

Data were analysed in Prism 6 (GraphPad). Group means were compared by one- or two-way ANOVA, using repeated measures designs where appropriate, followed by post-hoc analyses using Holm–Šídák's multiple comparisons test, a method with more power than the Bonferroni or Tukey methods (Seaman et al., 1991). Where the assumptions of normality or equality of variances were violated (as indicated by Shapiro–Wilk and Brown–Forsythe tests, respectively), group means were compared using two-sided Kruskal–Wallis test, followed by Dunn's multiple comparisons test. Reaction time distributions were compared by Kolmogorov–Smirnov test, using the Bonferroni correction to adjust the level of statistical significance; stimulus-response and current-spike frequency curves were analysed by *F* test. Functional imaging experiments were conducted blind to genotype. No statistical methods were used to predetermine sample sizes.

3 Results

3.1 Biophysics of FoxP-positive and FoxP-negative Kenyon cells

The single *FoxP* gene of *Drosophila* consists of six constitutively and two alternatively spliced exons that give rise to a minimum of two transcripts (*RC* and *RD*, Figure 6a) and corresponding protein isoforms (PC and PD) (Santos et al., 2011). The two isoforms share an N-terminal zinc finger domain but differ in their C-terminal, DNA-binding forkhead box motifs. The transposable element insertion sites of mutant *FoxP* alleles associated with reaction time phenotypes (Figure 4c) (DasGupta et al., 2014), including $FoxP^{5\text{-}SZ\text{-}3955}$, map to the last, alternatively spliced exon and are therefore predicted to disrupt the long (*RC*) transcript (Figure 6a). To test this prediction, I generated a polyclonal antibody against a protein consisting of the C-terminal 96 amino acids specific to the long isoform. Western blot analysis of protein extracts from wild-type flies and homozygous $FoxP^{5\text{-}SZ\text{-}3955}$ mutants

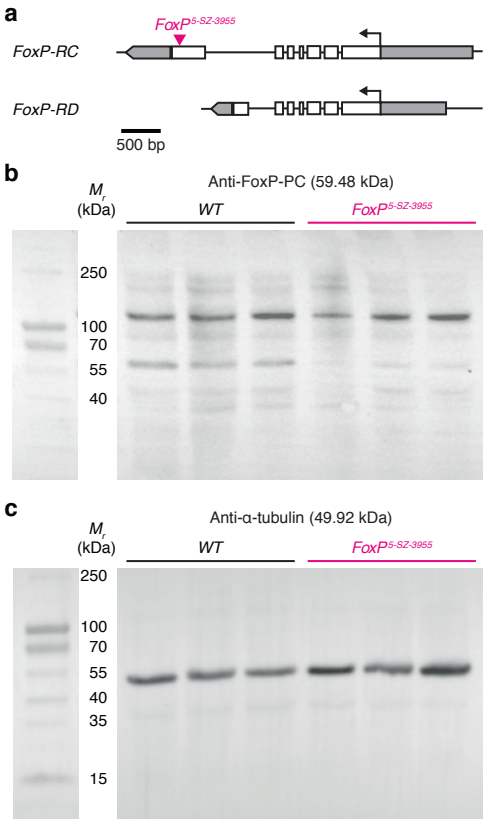


Figure 6. *Drosophila* FoxP isoforms.
a, Alternative splicing gives rise to at least two distinct transcripts of the *Drosophila FoxP* gene (*RC* and *RD*) and corresponding protein isoforms (PC and PD) that differ in their C-terminal forkhead domains. The P element insertion site (red arrowhead) in the mutant $FoxP^{5\text{-}SZ\text{-}3955}$ allele maps to this last, alternatively spliced exon of the long isoform *FoxP-RC*. **b**, Western blot analysis of protein extracts from wild-type (*WT*) and homozygous $FoxP^{5\text{-}SZ\text{-}3955}$ mutant flies. A polyclonal antibody raised against an antigen comprising the C-terminal 96 amino acids specific to FoxP-PC detected a band at the predicted relative molecular mass (M_r) of FoxP-PC (59.48 kDa) in wild-type flies; in $FoxP^{5\text{-}SZ\text{-}3955}$ flies, the intensity of the band was reduced. The antibody also detected a second, unspecific band of higher M_r. Protein standards of indicated M_r are displayed on the left. **c**, α-tubulin could be detected in samples from all genotypes at comparable intensities. Protein standards of indicated M_r are displayed on the left.

revealed a band at ~60 kDa, corresponding to the predicted molecular weight of FoxP-PC, enriched in the wild-type compared to the mutant genotype. A second, unspecific band of >100 kDa was present in all genotypes (Figure 6b). Traces of FoxP-PC protein were still detectable in the mutant genotype suggesting that the insertion of the transposable element, while drastically reducing protein abundance, might only cause an incomplete functional knockout of the *FoxP* gene.

This agrees with quantitative real-time PCR (qPCR) experiments performed by Laura Chan Wah Hak (Chan Wah Hak, unpublished data). The $\alpha\beta_c$ KC-specific driver lines *NP7175-GAL4* or *NP6024-GAL4* (Figure 5a, b) were used to drive moderate to high levels of a GFP-tagged ribosomal protein (Heiman et al., 2008) in $\alpha\beta_c$ KCs (Murthy et al., 2008; Tanaka et al., 2008), which are also marked, albeit more weakly, by a *FoxP* promoter fragment (DasGupta et al., 2014). Immunoprecipitation of tagged ribosomes from head homogenate (translating ribosome affinity purification or TRAP; Heiman et al., 2008), followed by reverse transcription of polysome-bound mRNA and qPCR, revealed an abundance of *FoxP-RC*, but not *FoxP-RD*, transcript in $\alpha\beta_c$ neurons. *FoxP-RC* mRNA concentrations were greatly, though not completely, reduced in homozygous $FoxP^{5\text{-}SZ\text{-}3955}$ mutants. A comparable reduction was achieved by expressing *NP7175-GAL4*-driven hairpin RNA

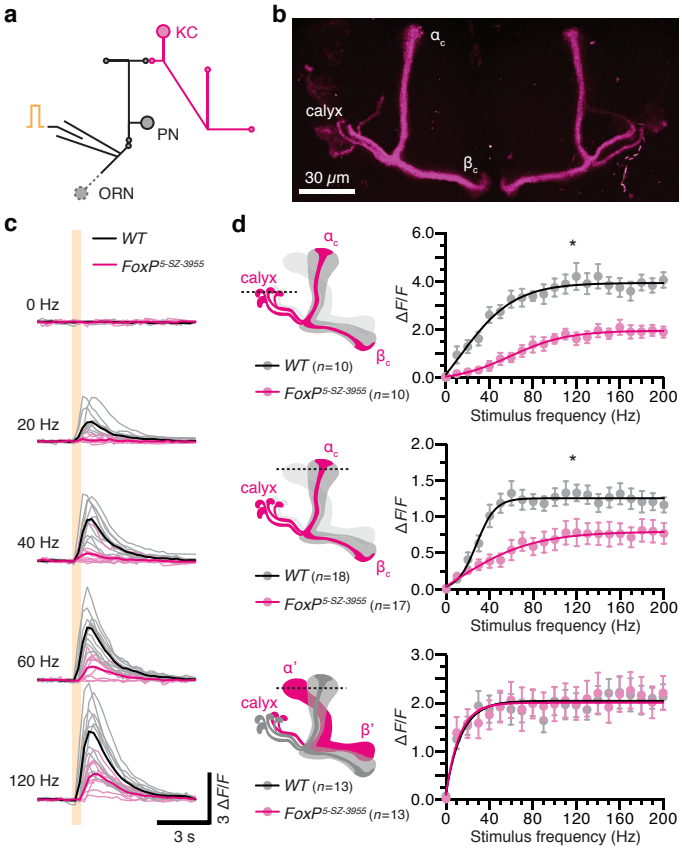


Figure 7. FoxP regulates the responsiveness of $\alpha\beta_c$ KCs to sensory stimulation.

a, Antennal nerve stimulation and two-photon Ca^{2+} imaging *in vivo*. ORN, olfactory receptor neuron; PN, projection neuron. **b**, *NP7175-GAL4*-driven GCaMP6m expression in $\alpha\beta_c$ KCs. **c**, Ca^{2+} transients in $\alpha\beta_c$ KC dendrites, evoked by 0.5-s epochs of antennal nerve stimulation at the indicated frequencies, of individual wild-type (*WT*, black, n = 10) or homozygous $FoxP^{5\text{-}SZ\text{-}3955}$ mutant flies (red, n = 10). Shaded traces represent responses in individual flies and solid traces are group averages. **d**, Peak $\Delta F/F$ as a function of stimulation frequency in $\alpha\beta_c$ KC dendrites (calyx, top) or axons (centre), or in α'β' KC axons (bottom), of wild-type (black) or homozygous $FoxP^{5\text{-}SZ\text{-}3955}$ mutant flies (red). Data are means ± s.e.m. Asterisks indicate significant differences between the stimulus-response curves of wild-type and $FoxP^{5\text{-}SZ\text{-}3955}$ mutant flies ($P < 0.0001$, F test). Dashed lines in insets indicate imaging planes.

directed against the *FoxP* transcript (*FoxP*^{RNAi}; Chan Wah Hak, unpublished data). α'β' neurons, labelled by the *VT030604-GAL4* driver (Figure 5c), lie outside the *FoxP-GAL4* expression pattern (DasGupta et al., 2014) and contained only trace amounts of both *FoxP* isoforms, irrespective of genotype (Chan Wah Hak, unpublished data). The mushroom body thus represents a mosaic of FoxP-positive and FoxP-negative KCs, as suggested by the expression pattern of *FoxP-GAL4* (DasGupta et al., 2014). The polyclonal anti-FoxP-PC antibody (Figure 6), however, failed to show clear, specific immunoreactivity with any KC subpopulation in immunohistochemical experiments.

For an initial determination of whether and how the transcription factor FoxP regulates the physiology of FoxP-expressing neurons, I targeted the Ca^{2+} indicator GCaMP6m to FoxP-positive $\alpha\beta_c$ or FoxP-negative α'β' KCs and imaged Ca^{2+} transients evoked by electrical stimulation of the ipsilateral antennal nerve (Figures 7a, b, and 8). Electrical instead of

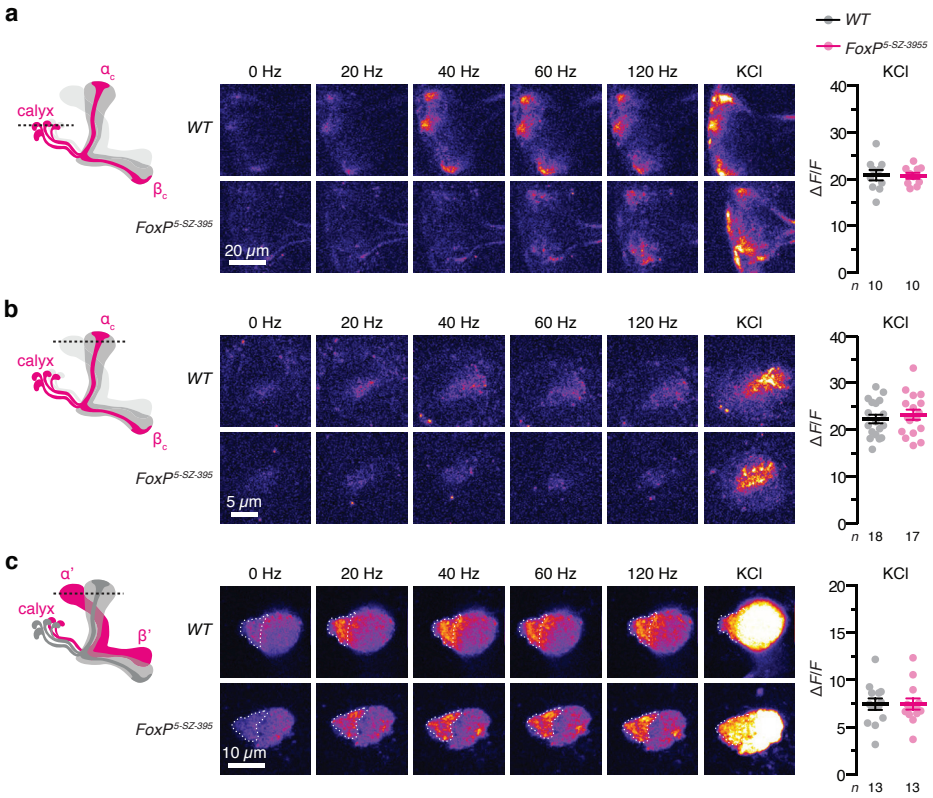


Figure 8. FoxP does not affect maximal GCaMP6m signals in KCs.
a–**c**, Raw two-photon images of GCaMP6m fluorescence (centre) in dendrites (**a**) or axons (**b**) of $\alpha\beta_c$ KCs or axons of α'β' KCs (circled regions of interest in **c**) at the indicated stimulation frequencies, in wild-type flies (*WT*) and homozygous *FoxP*$^{5\text{-}SZ\text{-}3955}$ mutants. At the end of each imaging experiment, neurons were bulk-depolarized by elevating the extracellular KCl concentration to 100 mM (right). *t* tests failed to detect significant differences between the peak changes in GCaMP6m fluorescence evoked by 100 mM KCl in wild-type flies (black) and homozygous *FoxP*$^{5\text{-}SZ\text{-}3955}$ mutants (red) ($P \geq 0.5245$). Dashed lines in insets (left) indicate imaging planes.

odour stimulation allowed me to recruit, reliably, all glomerular channels and activate KCs broadly rather than in sparse odour-specific ensembles whose membership has been shown to vary unpredictably from fly to fly (Caron et al., 2013; Gruntman and Turner, 2013; Murthy et al., 2008). The electrical stimulus was tailored to recapitulate the full range of spike frequencies observed in ORNs during odour presentations (Bhandawat et al., 2007). Both types of KC responded in a saturating fashion to stimulus trains of increasing frequency, but the normalized response amplitudes of the FoxP-negative α'β' cells increased more steeply and reached plateau at lower stimulation intensities than those of FoxP-positive $\alpha\beta_c$ KCs (Figure 7c, d). Mutating *FoxP* flattened the stimulus-response curves of $\alpha\beta_c$ but not of α'β' KCs: in normally FoxP-positive $\alpha\beta_c$ KCs Ca^{2+} concentrations now rose more slowly as a function of stimulus frequency and peaked at reduced plateaux (Figures 7c, d, and 8a, b). Responses of FoxP-negative α'β' neurons, in contrast, were unaffected in $FoxP^{5\text{-}SZ\text{-}3955}$ mutants (Figures 7d and 8c), suggesting that the overall organization and strength of inputs from olfactory projection neurons, which are thought to be shared among all classes of KC (Caron et al., 2013; Gruntman and Turner, 2013), were preserved. Changes specific to the

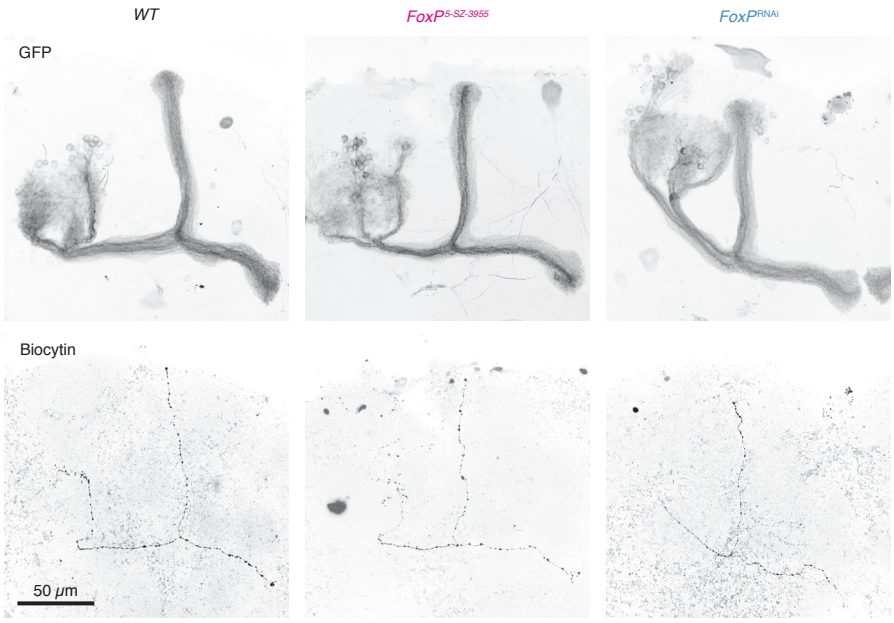


Figure 9. Morphology of $\alpha\beta_c$ KCs.
Example morphologies of $\alpha\beta_c$ KCs expressing *UAS-CD8::GFP* under the control of *NP7175-GAL4* in wild-type flies (*WT*, left), $FoxP^{5\text{-}SZ\text{-}3955}$ mutants (centre) and flies expressing *NP7175-GAL4*-driven $FoxP^{RNAi}$ (right). Top panels show maximum intensity projections of the genetically labelled population of $\alpha\beta_c$ KCs; bottom panels depict corresponding micrographs of single neurons filled with biocytin during patch clamp recordings in the same individuals. Somata of filled KCs and large parts of the dendritic tree are not visible, because they are inevitably removed after the recording due to the high-resistance seal, their small size, and superficial localization.

FoxP-positive $\alpha\beta_c$ KCs must therefore lie at the root of the selective response attenuation of these cells in *FoxP*-mutant flies. These changes, however, could reflect multiple underlying causes such as a reduction in excitatory input or alterations of the intrinsic membrane properties of $\alpha\beta_c$ KCs.

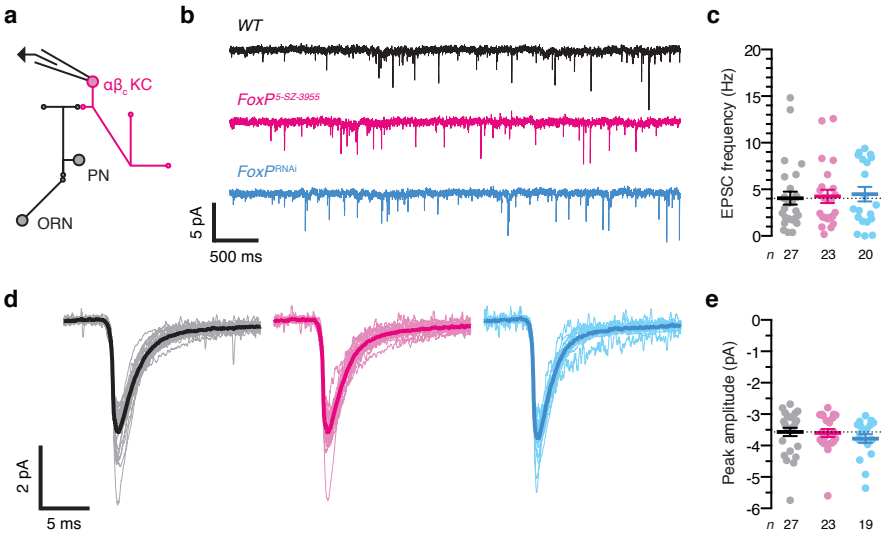


Figure 10. FoxP does not alter synaptic transmission onto $\alpha\beta_c$ KCs.
a, Targeted whole-cell voltage clamp recording *in vivo* from $\alpha\beta_c$ KCs expressing *NP7175-GAL4*-driven GFP. ORN, olfactory receptor neuron; PN, projection neuron. **b**, Example transmembrane currents (holding potential –90 mV) of $\alpha\beta_c$ KCs in wild-type flies (black), homozygous $FoxP^{5\text{-}SZ\text{-}3955}$ mutants (red), or flies expressing *NP7175-GAL4*-driven $FoxP^{RNAi}$ (blue). **c**, Kruskal–Wallis test failed to detect a significant difference in the mean frequency of spontaneous excitatory postsynaptic currents (EPSCs) in $\alpha\beta_c$ KCs of wild-type flies (black), homozygous $FoxP^{5\text{-}SZ\text{-}3955}$ mutants (red), or flies expressing *NP7175-GAL4*-driven $FoxP^{RNAi}$ (blue) (P = 0.8432). Circles, individual KCs; bars, means ± s.e.m. **d**, EPSCs of individual $\alpha\beta_c$ KCs (shaded traces) and averages (solid traces) at a holding potential of –90 mV in wild-type flies (black), homozygous $FoxP^{5\text{-}SZ\text{-}3955}$ mutants (red), or flies expressing *NP7175-GAL4*-driven $FoxP^{RNAi}$ (blue). **e**, Kruskal–Wallis test failed to detect a significant difference in peak EPSC amplitudes in $\alpha\beta_c$ KCs of wild-type flies (black), homozygous $FoxP^{5\text{-}SZ\text{-}3955}$ mutants (red), or flies expressing *NP7175-GAL4*-driven $FoxP^{RNAi}$ (blue) (P = 0.3847). Circles, individual KCs; bars, means ± s.e.m.

Whole-cell patch clamp recordings *in vivo* supported the latter hypothesis. $\alpha\beta_c$ KCs of wild-type flies, homozygous $FoxP^{5\text{-}SZ\text{-}3955}$ mutants, and flies expressing $FoxP^{RNAi}$ under the control of *NP7175-GAL4* had similar axonal morphology as revealed by dye fills of single cells (Figure 9), and received synaptic inputs at comparable rates (Figure 10b, c). At a holding potential of –90 mV, these inputs gave rise to excitatory postsynaptic currents (EPSCs) of the same average amplitudes (Figure 10d, e). FoxP-deficient $\alpha\beta_c$ KCs rested at similar membrane voltages as their wild-type counterparts (Figure 11b). Irrespective of genotype, action potentials were initiated at similar membrane voltages during steps or ramps of

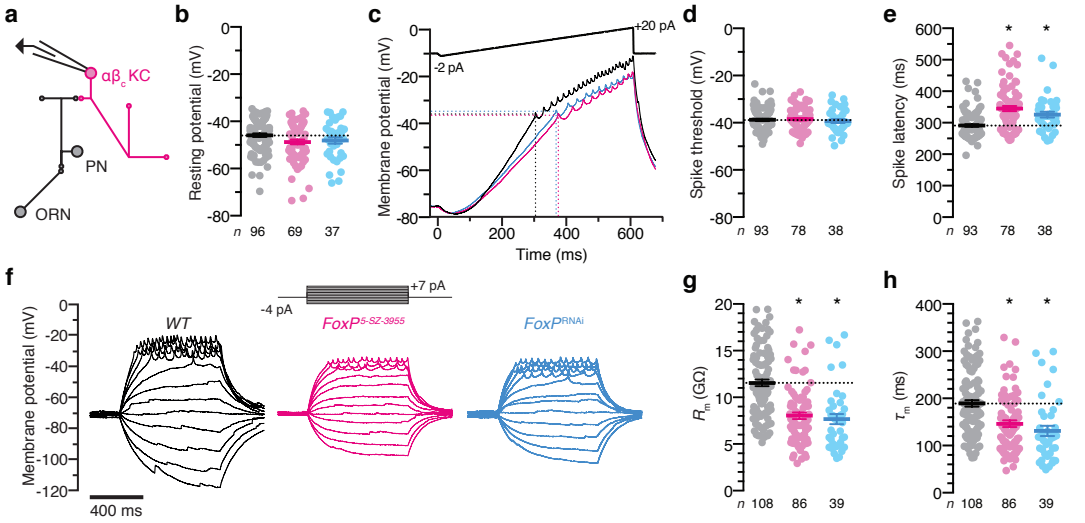


Figure 11. FoxP regulates the intrinsic excitability of αβ$_c$ KCs.
a, Targeted whole-cell current clamp recording *in vivo* from αβ$_c$ KCs expressing *NP7175-GAL4*-driven GFP. ORN, olfactory receptor neuron; PN, projection neuron. **b**, Resting membrane potentials of αβ$_c$ KCs in wild-type flies (black), homozygous *FoxP*$^{5\text{-}SZ\text{-}3955}$ mutants (red), or flies expressing *NP7175-GAL4*-driven *FoxP*^{RNAi} (blue); circles, individual KCs; bars, means ± s.e.m. One-way ANOVA failed to detect a significant difference between genotypes ($P = 0.0511$). **c**–**e**, Voltage responses (**c**) of αβ$_c$ KCs in wild-type flies (black), homozygous *FoxP*$^{5\text{-}SZ\text{-}3955}$ mutants (red), or flies expressing *NP7175-GAL4*-driven *FoxP*^{RNAi} (blue) to ramps of depolarizing current. FoxP-deficient αβ$_c$ KCs initiate action potentials at the same membrane voltage as wild-type cells (**d**, $P = 0.7143$) but reach threshold later during the ramp (**e**, $P < 0.0001$). Circles, individual KCs; bars, means ± s.e.m.; asterisks, significant differences from wild-type in post-hoc comparisons following one-way ANOVA or Kruskal–Wallis test. **f**–**h**, Voltage responses (**f**) of αβ$_c$ KCs in wild-type flies (black), homozygous *FoxP*$^{5\text{-}SZ\text{-}3955}$ mutants (red), or flies expressing *NP7175-GAL4*-driven *FoxP*^{RNAi} (blue) to steps of depolarizing current. FoxP-deficient αβ$_c$ KCs have lower input resistances (R_m) (**g**, $P < 0.0001$) and shorter membrane time constants (τ_m) than wild-type cells (**h**, $P < 0.0001$). Circles, individual KCs; bars, means ± s.e.m.; asterisks, significant differences from wild-type in post-hoc comparisons following Kruskal–Wallis tests.

depolarizing currents (Figure 11c, d, f), but the lower input resistances (Figure 11g) and shorter membrane time constants (Figure 11h) of FoxP-deficient neurons meant that larger currents were required to bring these cells to action potential threshold (Figure 11c, f). Because the necessary current amplitudes were reached later during depolarizing ramps (Figure 11c), the spike latencies of FoxP-deficient neurons exceeded those of wild-type cells (Figure 11e).

In contrast to the characteristic quiescence of αβ$_c$ KCs at rest, most FoxP-negative α'β' KCs were spontaneously active at similar membrane potential baselines, reflecting their lower action potential thresholds (Figure 12a–d) (Inada et al., 2017). α'β' KCs had lower input resistances and shorter membrane time constants than αβ$_c$ KCs (Figures 11f–h and 12f–h) and transduced depolarizing current steps nearly linearly into proportional spike rate increases, whereas αβ$_c$ KCs followed sigmoidal current-spike frequency functions (Figure 13). As expected for FoxP-negative neurons, interference with the expression of

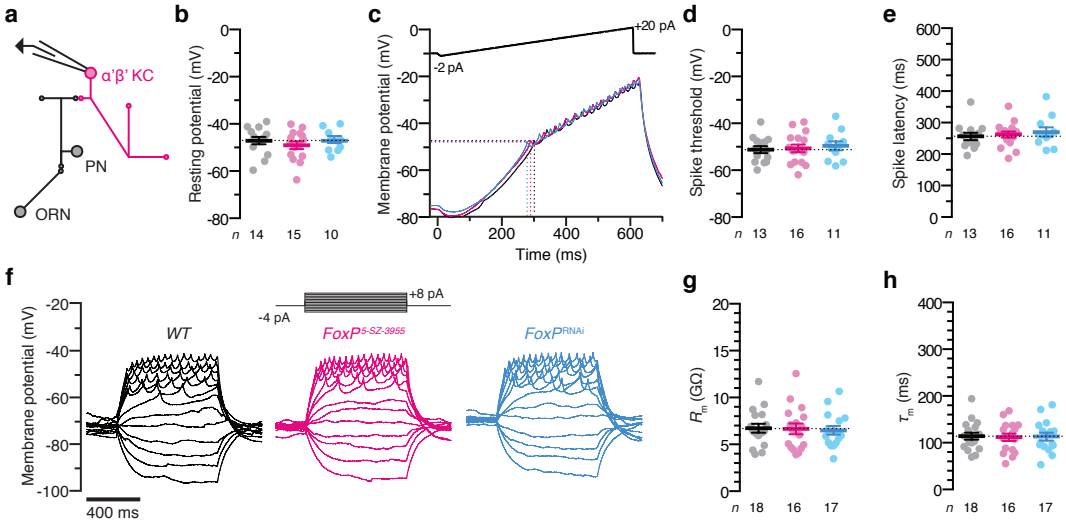


Figure 12. FoxP does not regulate the intrinsic excitability of α'β' KCs.
a, Targeted whole-cell recording *in vivo* from α'β' KCs expressing *VT030604-GAL4*-driven GFP. ORN, olfactory receptor neuron; PN, projection neuron. **b**, Resting membrane potentials of α'β' KCs in wild-type flies (black), homozygous *FoxP*$^{5\text{-}SZ\text{-}3955}$ mutants (red), or flies expressing *VT030604-GAL4*-driven *FoxP*^{RNAi} (blue); circles, individual KCs; bars, means ± s.e.m. One-way ANOVA failed to detect a significant difference between genotypes (P = 0.6016). **c**–**e**, Voltage responses (**c**) of α'β' KCs in wild-type flies (black), homozygous *FoxP*$^{5\text{-}SZ\text{-}3955}$ mutants (red), or flies expressing *VT030604-GAL4*-driven *FoxP*^{RNAi} (blue) to ramps of depolarizing current. FoxP-deficient α'β' KCs initiate action potentials at the same membrane voltage (**d**, P = 0.8062) and with the same latency as wild-type cells (**e**, P = 0.7373). Circles, individual KCs; bars, means ± s.e.m. **f**–**h**, Voltage responses (**f**) of α'β' KCs in wild-type flies (black), homozygous *FoxP*$^{5\text{-}SZ\text{-}3955}$ mutants (red), or flies expressing *VT030604-GAL4*-driven *FoxP*^{RNAi} (blue) to steps of depolarizing current. FoxP-deficient and wild-type α'β' KCs have identical input resistances (R_m) (**g**, P = 0.9497) and membrane time constants (τ_m) (**h**, P = 0.9771). Circles, individual KCs; bars, means ± s.e.m.

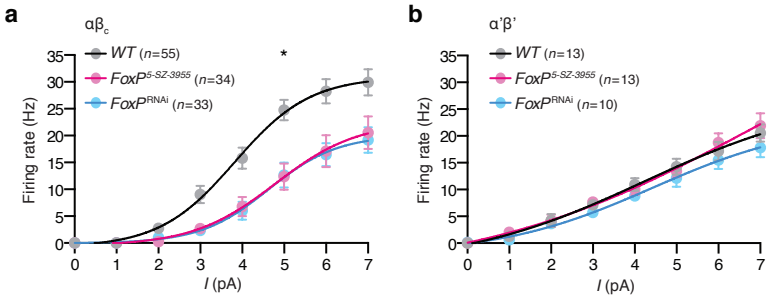


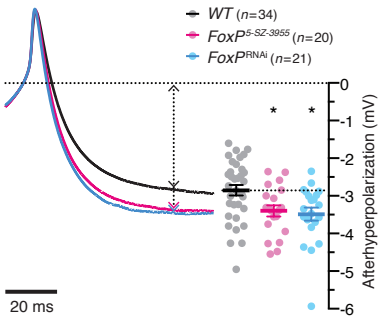
Figure 13. FoxP alters the current-spike frequency function of αβ$_c$ KCs but not of α'β' KCs.
a, Spike frequencies evoked by depolarizing current injections of increasing amplitudes into αβ$_c$ KCs of wild-type flies (black), homozygous *FoxP*$^{5\text{-}SZ\text{-}3955}$ mutants (red), or flies expressing *NP7175-GAL4*-driven *FoxP*^{RNAi} (blue). Data are means ± s.e.m. F test detected a significant difference between the current-spike frequency functions of wild-type and FoxP-deficient αβ$_c$ KCs (P < 0.0001). **b**, Spike frequencies evoked by depolarizing current injections into α'β' KCs of wild-type flies (black), homozygous *FoxP*$^{5\text{-}SZ\text{-}3955}$ mutants (red), or flies expressing *VT030604-GAL4*-driven *FoxP*^{RNAi} (blue). Data are means ± s.e.m. F test failed to detect a significant difference between the current-spike frequency functions of wild-type and FoxP-deficient α'β' KCs (P = 0.0660). Curves originate at 0 Hz because the cells were held at an initial membrane potential of -70 ± 5 mV (see Methods).

FoxP, be it ubiquitously through mutation or in an α'β' KC-restricted manner through *VT030604-GAL4*-driven *FoxP*^{RNAi}, did not perturb any of the biophysical characteristics of α'β' KCs (Figures 12 and 13b).

3.2 FoxP represses *Shal* in $\alpha\beta_c$ KCs

The identical spike thresholds of wild-type and FoxP-deficient $\alpha\beta_c$ KCs (Figure 11c, d) argue against a role of FoxP in regulating voltage-gated sodium or calcium channels, which shape the upstroke of the action potential (Hille, 2001; Koch, 1999). The prolonged latency to spiking during current ramps (Figure 11c, e) and subtle changes in the action potential waveform during repolarization (Figure 14) instead hint at augmented potassium currents in FoxP-deficient $\alpha\beta_c$ KCs (Kim et al., 2005). Whole-cell voltage-clamp experiments *in vivo* confirmed this notion.

Figure 14. FoxP influences the action potential waveform of $\alpha\beta_c$ KCs.
Average action potential waveforms (left) and afterhyperpolarization amplitudes (right) of $\alpha\beta_c$ KCs in wild-type flies (black), homozygous *FoxP*$^{5\text{-}SZ\text{-}3955}$ mutants (red), or flies expressing *NP7175-GAL4*-driven *FoxP*^{RNAi} (blue). Circles, individual KCs; bars, means ± s.e.m. Kruskal–Wallis test detected a significant genotype effect (P = 0.0058); asterisks denote significant differences from wild-type in post-hoc comparisons.



$\alpha\beta_c$ KCs expressed a prominent voltage-dependent A-type potassium current (Figure 15a, b) with half-activation and -inactivation voltages at steady state of –16.6 ± 1.5 mV and –72.9 ± 1.2 mV, respectively (Figure 15c, d), and an inactivation time constant of 37.2 ± 2.4 ms at +50 mV (Figure 15e, f). Deficiency of FoxP nearly doubled the membrane density of this current (Figure 15a, b) while leaving its steady-state activation and inactivation curves (Figure 15c, d) as well as its inactivation time constant (Figure 15e, f) unchanged. FoxP thus appears to control the cell surface density of the pore-forming α subunit of a voltage-gated potassium (K_V) channel and not the level of an accessory protein that influences the channel's gating.

The gating parameters of this transient A-type current expressed by $\alpha\beta_c$ KCs (Figure 15c-f), its sensitivity to phrixotoxin-2 (Figure 16a, b) and low concentrations of Ba^{2+} (Figure 16c, d) matched those of Shal, the *Drosophila* homologue of the K_V4 family of ion channels

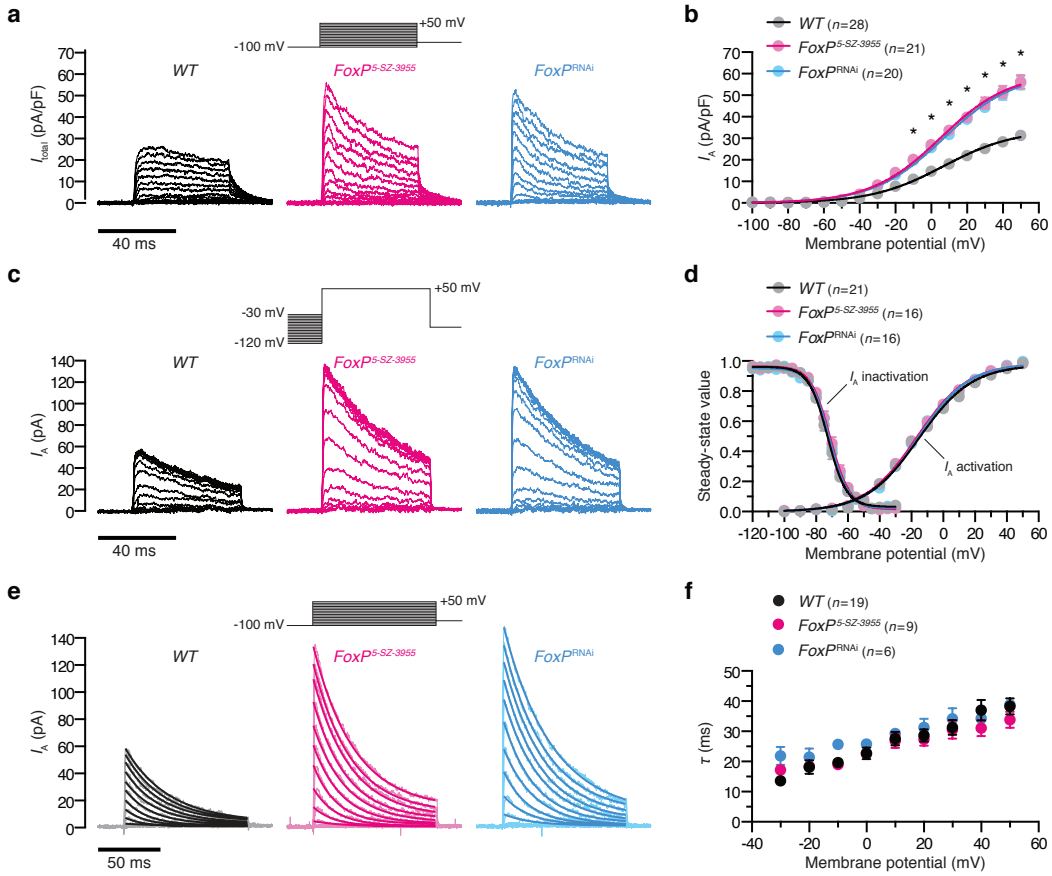


Figure 15. FoxP represses an A-type potassium current in αβ$_c$ KCs.
a, Examples of potassium current densities, evoked by voltage steps from a holding potential of –100 mV, in αβ$_c$ KCs of wild-type flies (black), homozygous *FoxP*$^{5\text{-}SZ\text{-}3955}$ mutants (red), or flies expressing *NP7175-GAL4*-driven *FoxP*^{RNAi} (blue). **b**, Average A-type potassium current densities in FoxP-deficient αβ$_c$ KCs are increased relative to wild-type cells (**b**, $P < 0.0001$). Circles, means ± s.e.m.; solid lines, Boltzmann fits; asterisks, significant differences from wild-type in post-hoc comparisons following two-way ANOVA. **c**, Examples of A-type potassium currents evoked by stepping αβ$_c$ KCs of wild-type flies (black), homozygous *FoxP*$^{5\text{-}SZ\text{-}3955}$ mutants (red), or flies expressing *NP7175-GAL4*-driven *FoxP*^{RNAi} (blue) from variable holding potentials (–120 mV to –30 mV) to a test potential of +50 mV. **d**, Steady-state activation and inactivation curves of A-type potassium currents in αβ$_c$ KCs of wild-type flies (black), homozygous *FoxP*$^{5\text{-}SZ\text{-}3955}$ mutants (red), or flies expressing *NP7175-GAL4*-driven FoxP^{RNAi} (blue). Circles, means ± s.e.m.; solid lines, Boltzmann fits. Kruskal–Wallis tests failed to detect significant genotype effects on half-activation voltage ($P = 0.9102$), activation slope factor ($P = 0.9422$), half-inactivation voltage ($P = 0.4735$), and inactivation slope factor ($P = 0.8752$). **e**, Average A-type potassium currents (shaded lines) evoked by stepping the membrane potential of αβ$_c$ KCs of wild-type flies (black), homozygous *FoxP*$^{5\text{-}SZ\text{-}3955}$ mutants (red), or flies expressing *NP7175-GAL4*-driven *FoxP*^{RNAi} (blue) from –100 mV to variable test potentials. A-type currents were isolated by subtracting non-inactivating currents measured from a holding potential of –30 mV. Solid lines represent exponential fits to the inactivating phase of the currents. **f**, Inactivation time constants τ of I_A in αβ$_c$ KCs of wild-type flies (black), homozygous *FoxP*$^{5\text{-}SZ\text{-}3955}$ mutants (red), or flies expressing *NP7175-GAL4*-driven *FoxP*^{RNAi} (blue) as a function of voltage. Two-way repeated measures ANOVA failed to detect a significant interaction between genotype and the voltage-dependence of τ ($P = 0.8943$).

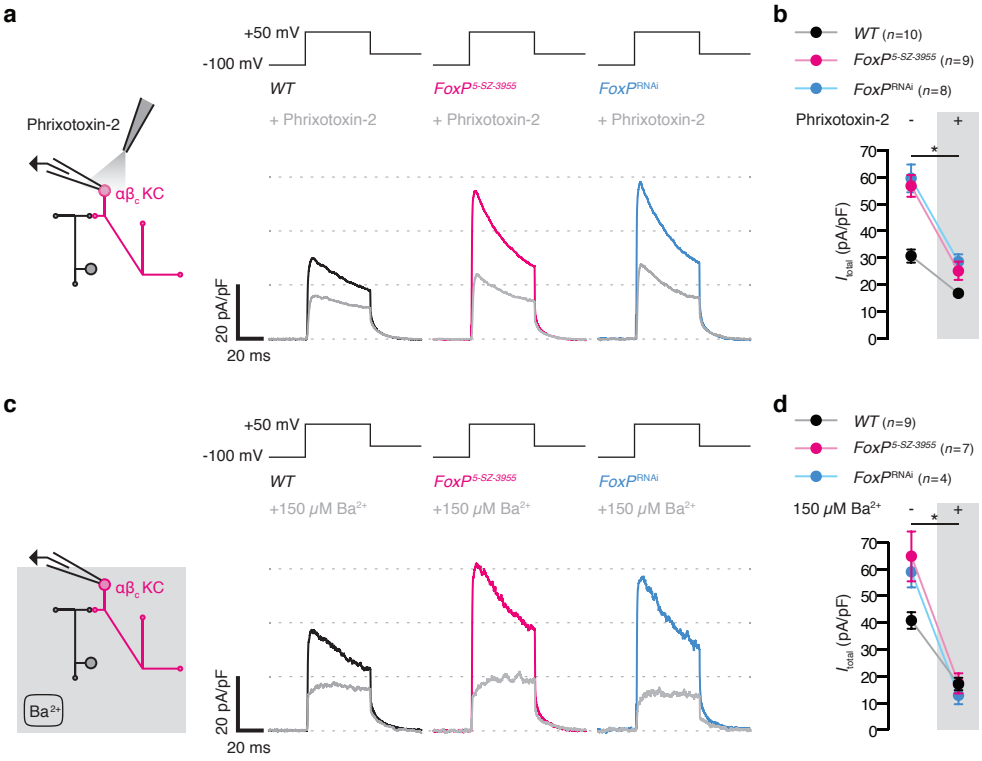


Figure 16. A-type potassium currents of αβ$_c$ KCs show pharmacological characteristics of Shal.

a, Application of phrixotoxin-2 to the soma of an αβ$_c$ KC. Average potassium current densities in response to a single voltage pulse before (coloured lines) and after (grey lines) the application of phrixotoxin-2 to αβ$_c$ KCs of wild-type flies (black), homozygous *FoxP*$^{5\text{-}SZ\text{-}3955}$ mutants (red), or flies expressing *NP7175-GAL4*-driven *FoxP*^{RNAi} (blue). **b**, Average peak current densities before (left) and after (right) the application of phrixotoxin-2. Data are means ± s.e.m. Two-way repeated-measures ANOVA detected significant effects of genotype and toxin ($P < 0.0001$) and a significant genotype × toxin interaction ($P = 0.0050$); the asterisk denotes significant differences in peak current densities before and after the application of phrixotoxin-2. One-way ANOVA detected a significant difference in peak current densities among wild-type and FoxP-deficient αβ$_c$ KCs before ($P < 0.0001$) and after ($P = 0.0067$) the application of phrixotoxin-2. **c**, Bath-application of 150 µM Ba^{2+}. Average potassium current densities in response to a single voltage pulse before (coloured lines) and after (grey lines) the application of Ba^{2+} to αβ$_c$ KCs of wild-type flies (black), homozygous *FoxP*$^{5\text{-}SZ\text{-}3955}$ mutants (red), or flies expressing *NP7175-GAL4*-driven *FoxP*^{RNAi} (blue). **d**, Average peak current densities before (left) and after (right) Ba^{2+}-application. Data are means ± s.e.m. Two-way repeated-measures ANOVA detected a significant effect of Ba^{2+}-treatment ($P < 0.0001$) and a significant genotype × treatment interaction ($P = 0.0012$); the asterisk denotes significant differences in peak current densities before and after the addition of Ba^{2+}. Kruskal-Wallis tests detected a significant difference in peak current densities among wild-type and FoxP-deficient αβ$_c$ KCs before ($P = 0.0034$) but not after ($P = 0.2968$) the addition of Ba^{2+}.

(Butler et al., 1989; Gasparini et al., 2007; Gasque et al., 2005; Norris and Nerbonne, 2010; Podlaski et al., 2017; Wei et al., 1990). Quantitation of polysome-bound transcripts after cell-specific TRAP performed by Laura Chan Wah Hak independently identified Shal as the sole FoxP target among the pore-forming subunits of 32 potassium, sodium, calcium, and chloride channels encoded in the fly genome. Mutation of the *FoxP* locus or RNAi-mediated

depletion of FoxP elevated the concentrations of *Shal* mRNA in $\alpha\beta_c$ KCs ~10-fold; the levels of all other ion channel transcripts remained unaltered (Chan Wah Hak, unpublished data).

3.3 FoxP, Shal, and synaptic integration

The somatodendritic localization (Figure 17) (Diao et al., 2010) and hyperpolarized voltage operating range of Shal (Figure 15a–d) suggest that the channel, like its mammalian orthologue $K_V4.2$ in hippocampal pyramidal cells (Cai et al., 2004; Hoffman et al., 1997; Kim et al., 2005; Sheng et al., 1992), dampens dendritic voltage deflections and thereby regulates the amplitude, time course, and propagation of excitatory postsynaptic potentials (EPSPs).

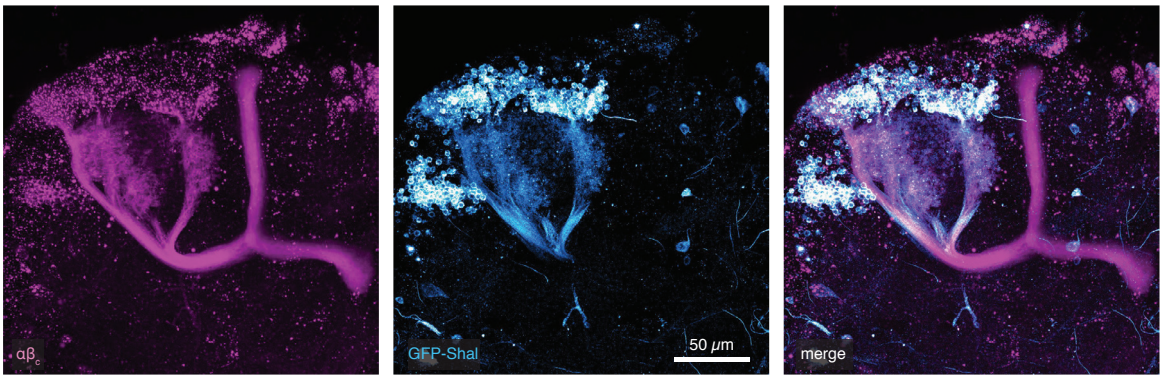
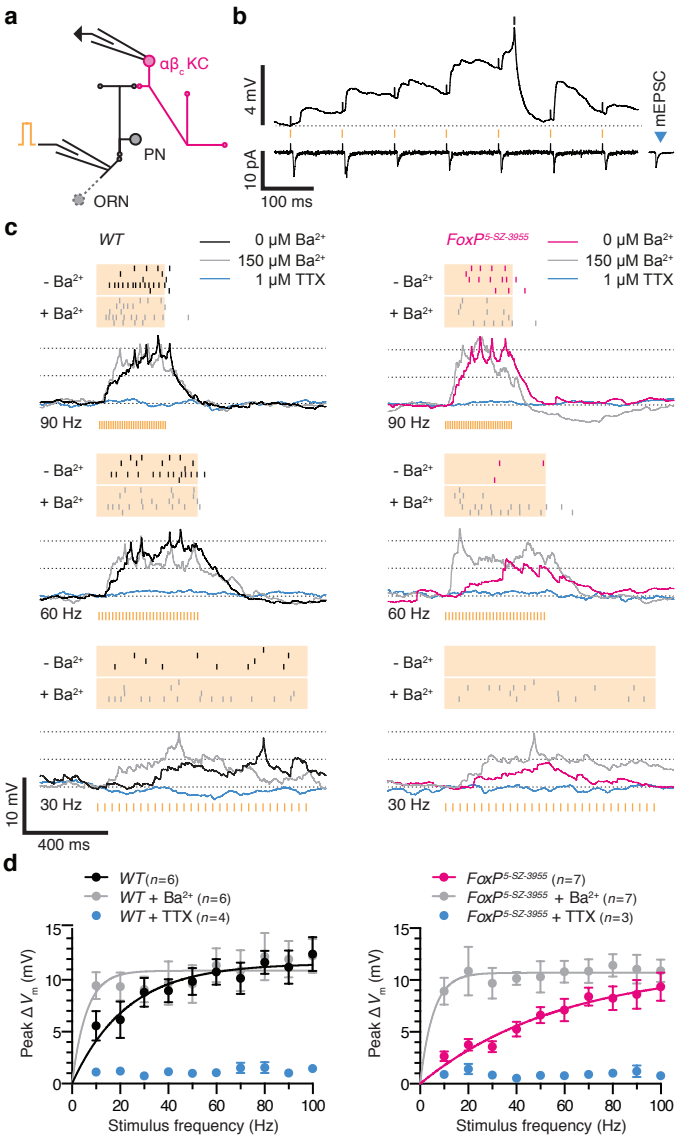


Figure 17. Somatodendritic localization of Shal in in $\alpha\beta_c$ KCs.
NP6024-GAL4-driven expression of membrane-bound mCherry (red) and GFP-tagged Shal (blue) in $\alpha\beta_c$ KCs.

To test for a role of Shal (and, indirectly, of FoxP) in synaptic integration, I recorded from $\alpha\beta_c$ and α'β' KCs *in vivo* while electrically stimulating trains of 30 mostly unitary synaptic inputs from antennal lobe projection neurons (Figures 18, 19, and 20). Varying the input frequencies while leaving the total number of stimuli unchanged allowed me to probe the ability of KCs to add up a set number of successive EPSPs over different timescales. The membrane potentials of $\alpha\beta_c$ KCs in wild-type flies climbed in a step-wise fashion from resting potential to spike threshold, bridging the average potential difference of 8.2 mV by integrating 4–30 synaptic quanta (Figure 18b, c). Inputs were summed most efficiently when delivered at high frequencies (Figure 18c, d), but even EPSPs spaced 100 ms apart could add up sufficiently to drive spiking (Figure 18b). By contrast, the narrow voltage gap between the resting potentials and spike thresholds of α'β' KCs (Figure 20b, d) (Inada et al., 2017) eliminated the need for integrating synaptic inputs over time (Figure 20b–d).

Figure 18. FoxP tunes the integrative properties of $\alpha\beta_c$ KCs.

a, Antennal nerve stimulation and targeted whole-cell recording *in vivo* from $\alpha\beta_c$ KCs expressing *NP7175-GAL4*-driven GFP. ORN, olfactory receptor neuron; PN, projection neuron. **b**, Sequentially recorded voltage (top) and transmembrane current responses (bottom, holding potential –70 mV) of the same $\alpha\beta_c$ KC in a wild-type fly during antennal nerve stimulation at 10 Hz (orange marks); the average of 119 miniature EPSCs recorded in the same cell (mEPSC) is shown for comparison. **c**, Examples of spike rasters of 5 $\alpha\beta_c$ KCs (top) and voltage responses of one exemplary cell (bottom) in wild-type flies (left) and homozygous *FoxP*$^{5\text{-}SZ\text{-}3955}$ mutants (right) during minimal antennal nerve stimulation at the indicated frequencies, in control conditions (black or red) and after the sequential addition of 150 µM Ba^{2+} to block Shal (grey) and 1 µM tetrodotoxin (TTX) to block action potentials (blue). Groups of three traces each correspond to responses recorded from one and the same cell under different conditions. Stimulus artifacts were removed for clarity. Dashed lines are spaced 5 mV apart. **d**, Stimulus-response curves of $\alpha\beta_c$ KCs in wild-type flies (left) and homozygous *FoxP*$^{5\text{-}SZ\text{-}3955}$ mutants (right) during antennal nerve stimulation, in control conditions (black or red) and after the addition of 150 µM Ba^{2+} to block Shal (grey) and 1 µM TTX to block action potentials (blue). Data are means ± s.e.m.



The EPSC amplitudes of wild-type and FoxP-deficient $\alpha\beta_c$ KCs were identical when the cells were voltage-clamped below the activation threshold of Shal (Figure 10c, d). In current-clamp recordings near resting potential, however, spontaneous EPSPs in $\alpha\beta_c$ KCs of *FoxP* mutants were smaller and decayed faster than those in wild-type cells (Figure 21), and evoked EPSPs were dissipated more readily (Figure 18c) than those in wild-type cells. Consequently, opportunities for temporal summation of synaptic inputs were curtailed, and only high-frequency stimulation could produce cumulative membrane depolarizations that breached action potential threshold (Figure 18c, d). The addition of 150 µM Ba^{2+}, which at this concentration selectively blocks K_V4 channels (Figure 16c, d) (Gasparini et al., 2007; Norris and Nerbonne, 2010), steepened the stimulus-response curves of wild-type and

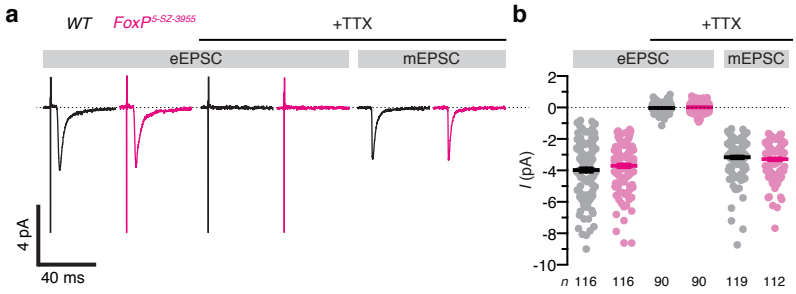
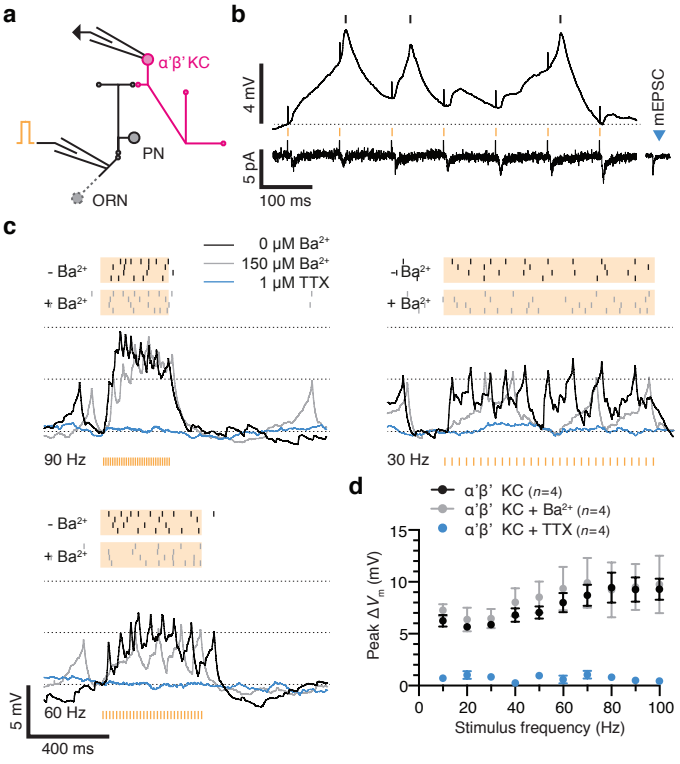


Figure 19. Comparison of stimulus-evoked and miniature EPSCs in αβ$_c$ KCs.

a, Average transmembrane currents (holding potential –90 mV) of αβ$_c$ KCs in wild-type flies (black) or homozygous *FoxP*$^{5\text{-}SZ\text{-}3955}$ mutants (red). EPSCs evoked by 50-µs voltage pulses (eEPSC, left and centre) could be blocked by 1 µM tetrodotoxin (TTX; centre); to minimise the fraction of transmission failures, stimulation voltages exceeded those at which EPSCs were first detected (minimal stimulation) by ~25%. The peak currents of spontaneously occurring miniature EPSCs in 1 µM TTX (mEPSCs, right) averaged 79.7–88.6% of those of eEPSCs, suggesting that ~16% of electrical stimuli caused the release of more than one quantum of transmitter. **b**, Peak eEPSC currents in the absence and presence of 1 µM TTX (left and centre) vs. peak mEPSC currents in 1 µM TTX (right), in αβ$_c$ KCs of wild-type flies (black) and homozygous *FoxP*$^{5\text{-}SZ\text{-}3955}$ mutants (red). Circles, individual EPSCs; bars, means ± s.e.m. Dunn's test following one-way Kruskal–Wallis test did not detect a significant effect of release mode (evoked vs. spontaneous, $P = 0.0852$) or genotype ($P > 0.9999$).

Figure 20. Integrative properties of α'β' KCs.

a, Antennal nerve stimulation and targeted whole-cell recording *in vivo* from α'β' KCs expressing *VT030604-GAL4*-driven GFP. ORN, olfactory receptor neuron; PN, projection neuron. **b**, Sequentially recorded voltage (top) and transmembrane current responses (bottom, holding potential –70 mV) of the same α'β' KC in a wild-type fly during antennal nerve stimulation at 10 Hz (orange marks); the average of 17 miniature EPSCs recorded in the same cell (mEPSC) is shown for comparison. **c**, Examples of spike rasters of 4 α'β' KCs (top) and voltage responses of one exemplary cell (bottom) in wild-type flies during minimal antennal nerve stimulation at the indicated frequencies, in control conditions (black) and after the sequential addition of 150 µM Ba^{2+} to block Shal (grey) and 1 µM tetrodotoxin (TTX) to block action potentials (blue). Groups of three traces each correspond to responses recorded from one and the same cell under different conditions. Stimulus artifacts were removed for clarity. **d**, Stimulus-response curves of α'β' KCs in wild-type flies during antennal nerve stimulation, in control conditions (black) and after the addition of 150 µM Ba^{2+} to block Shal (grey) and 1 µM TTX to block action potentials (blue). Data are means ± s.e.m.



FoxP-deficient cells to different degrees (probably reflecting the different amounts of Shal expressed by these neurons) and brought them into precise alignment ($P = 0.9702$, F test; Figure 18d): $\alpha\beta_c$ KCs of both wild-type and mutant flies now required just a handful of synaptic impulses to emit action potentials (Figure 18c, d).

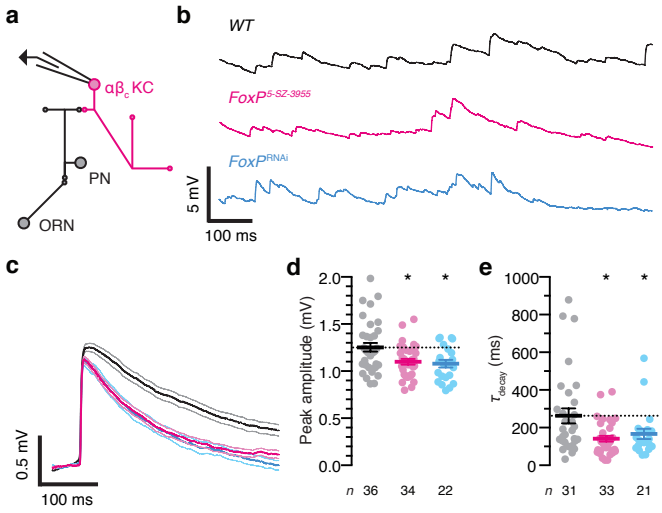


Figure 21. FoxP influences the EPSP waveform of $\alpha\beta_c$ KCs.
a, Targeted whole-cell current clamp recording in vivo from $\alpha\beta_c$ KCs expressing *NP7175-GAL4*-driven GFP. ORN, olfactory receptor neuron; PN, projection neuron. **b**, Example membrane potential traces of $\alpha\beta_c$ KCs in wild-type flies (black), homozygous *FoxP*$^{5\text{-}SZ\text{-}3955}$ mutants (red), or flies expressing *NP7175-GAL4*-driven *FoxP*^{RNAi} (blue). **c**–**e**, EPSP waveforms (**c**) in $\alpha\beta_c$ KCs of wild-type flies (black), homozygous *FoxP*$^{5\text{-}SZ\text{-}3955}$ mutants (red), or flies expressing *NP7175-GAL4*-driven *FoxP*^{RNAi} (blue). EPSP waveforms (solid and shaded lines, means ± s.e.m.) in wild-type flies (black), homozygous *FoxP*$^{5\text{-}SZ\text{-}3955}$ mutants (red), or flies expressing *NP7175-GAL4*-driven *FoxP*^{RNAi} (blue). Cell numbers are indicated in (**d**). FoxP-deficient $\alpha\beta_c$ KCs have lower mEPSP amplitudes (**d**, $P < 0.0036$) and shorter decay time constants (τ_{decay}) than wild-type cells (**e**, $P = 0.0299$). Circles, individual KCs; bars, means ± s.e.m.; asterisks, significant differences from wild-type in post-hoc comparisons following one-way ANOVA or Kruskal-Wallis test. In five $\alpha\beta_c$ KCs of wild-type flies, one $\alpha\beta_c$ KC of a *FoxP*$^{5\text{-}SZ\text{-}3955}$ mutant, and one $\alpha\beta_c$ KC of a *FoxP*^{RNAi} fly, a satisfactory single-exponential fit to the decaying phase of the EPSP could not be found; these cells were excluded from the analyis of τ_{decay} in (**e**).

3.4 FoxP, Shal, and reaction times

The ability to erase the biophysical difference between *FoxP*-mutant and wild-type $\alpha\beta_c$ KCs, simply by blocking Shal (Figure 18c–d), reaffirms the notion that this ion channel is a crucial mediator of FoxP's effects on $\alpha\beta_c$ KCs. I therefore examined whether an analogous manipulation could also correct the reaction time phenotype of *FoxP* mutants on the behavioural level. Flies were trained to avoid a specific concentration (20 ppm) of 4-methylyclohexanol (MCH) by pairing odour exposures with electric foot shock (Figure 4a) (Claridge-Chang et al., 2009; DasGupta et al., 2014). The animals then had to discriminate the reinforced concentration of MCH from a lower intensity (2, 8, 14, or 18 ppm, respectively) of the same odour (Figure 22a). The difficulty of discrimination was adjusted by varying the MCH concentration ratio during testing. Control flies make rapid, accurate decisions in easy discriminations (concentration ratio 0.1) and slow, error-prone choices in difficult tasks (concentration ratio 0.9). Homozygous carriage of the *FoxP*$^{5\text{-}SZ\text{-}3955}$ mutation extracted

a steeper difficulty-dependent cost of decision time (Figure 4c) (DasGupta et al., 2014), but the chronometric function was restored to its wild-type shape when *FoxP*$^{5\text{-}SZ\text{-}3955}$ mutants expressed a dominant-negative Shal subunit (*UAS-DN-Shal*) selectively in $\alpha\beta_c$ KCs (Figure 22b). Expression of the *UAS-DN-Shal* transgene, which encodes a pore loop mutation (Kim et al., 2005; Ping et al., 2011), reduced A-type current densities in $\alpha\beta_c$ KCs of *FoxP*$^{5\text{-}SZ\text{-}3955}$ mutants effectively to below wild-type values (Figure 23a).

The overexpression of functional Shal in $\alpha\beta_c$ KCs of wild-type flies had the opposite effect: it increased A-type current densities dramatically (Figure 23b) while preserving the channel's steady-state gating parameters (Figure 23d) and its sensitivity to phrixotoxin-2 (Figure 23c), just like under *FoxP*-mutant conditions (Figures 15d and 16a). On the behavioural level,

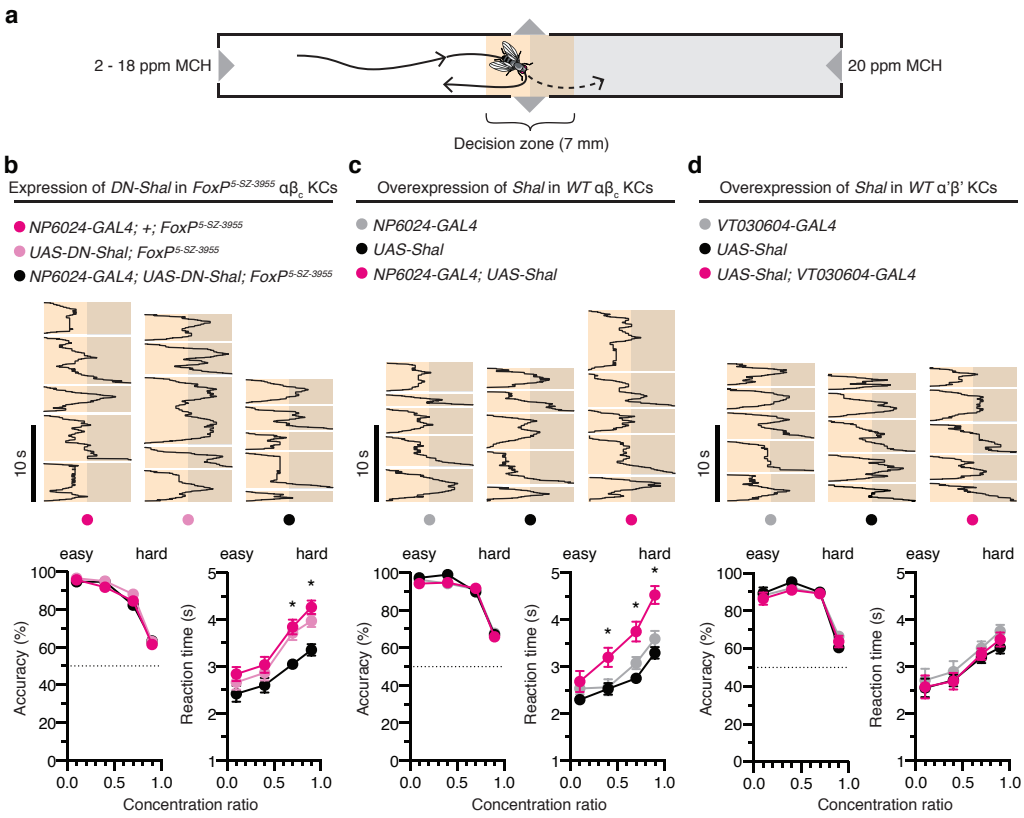


Figure 22. Shal currents in $\alpha\beta_c$ KCs determine reaction times.
a, Measurement of reaction times and decision accuracies. Two odour streams converge in a 7-mm wide decision zone (orange) at the centre of a narrow chamber. Flies are trained to avoid 20 ppm of 4-methylcyclohexanol (MCH, grey) and must discriminate the reinforced from a lower MCH concentration (2–18 ppm); the concentration ratio during testing determines the difficulty of the task. The time spent in the decision zone is quantified as the reaction time. **b**–**d**, Example traces (top) of position on the long chamber axis vs. time of the indicated genotypes in the decision zone; the MCH concentration ratio is 0.9. Accuracy (bottom left) and reaction time (bottom right) of the indicated genotypes as functions of the MCH concentration ratio during discrimination. Data are means ± s.e.m. (see Table 1 for sample sizes); asterisks, significant differences of experimental flies from both parental controls (accuracy: Dunn's test following one-way Kruskal–Wallis test; reaction time: Kolmogorov-Smirnov test with Bonferroni-corrected $P < 0.00625$).

Genotype	Concentration ratio							
	0.1		0.4		0.7		0.9	
	Flies	Decisions	Flies	Decisions	Flies	Decisions	Flies	Decisions
NP6024-GAL4/+; +; FoxP$^{5\text{-}SZ\text{-}3955}$	168	550	110	363	156	635	179	665
UAS-DN-Shal/+; FoxP$^{5\text{-}SZ\text{-}3955}$	152	539	127	446	151	665	203	913
NP6024-GAL4/+; UAS-DN-Shal/+; FoxP$^{5\text{-}SZ\text{-}3955}$	112	371	118	398	165	727	144	619
NP6024-GAL4/+	188	530	119	420	144	666	110	480
UAS-GFP-Shal/+; tubP-GAL80^{ts}/+	141	410	171	643	134	706	110	547
NP6024-GAL4/+; UAS-GFP-Shal/+; tubP-GAL80^{ts}/+	118	306	148	410	101	401	133	575
VT030604-GAL4/+	83	182	114	303	179	652	177	617
UAS-GFP-Shal/+; 2xGAL80ts/+	80	187	139	446	151	665	121	486
UAS-GFP-Shal/+; VT030604-GAL4/2xGAL80ts	82	160	130	433	143	601	119	385

Table 1. Sample sizes for behavioural measurements in Figure 22.

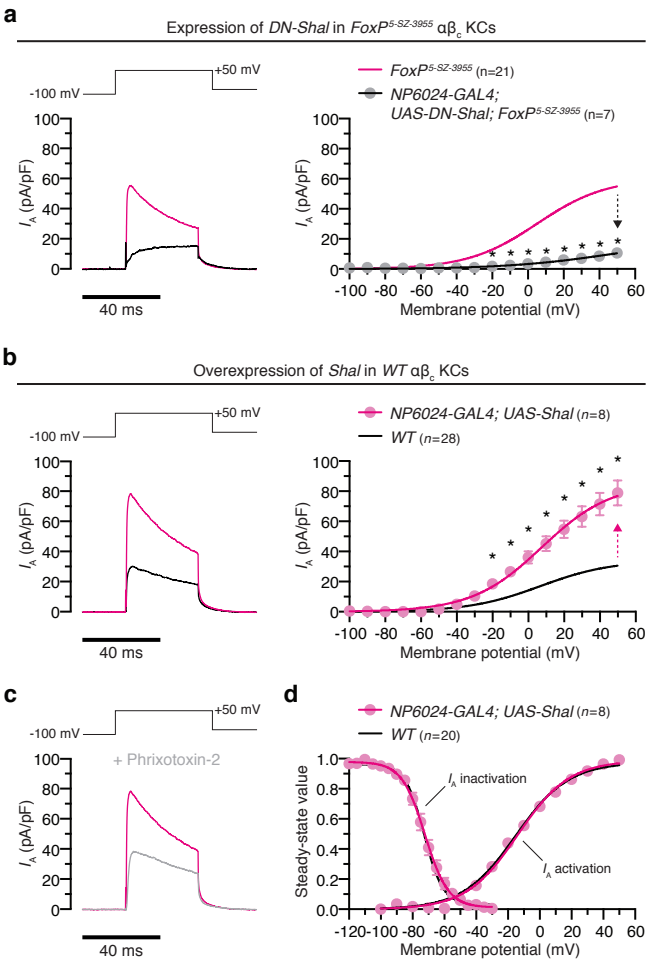


Figure 23. Bidirectional manipulations of Shal currents in αβ$_c$ KCs.
a, Average potassium current density trace in response to a voltage pulse (inset) in αβ$_c$ KCs overexpressing dominant-negative Shal (*UAS-DN-Shal*) in a homozygous *FoxP*$^{5\text{-}SZ\text{-}3955}$-mutant genetic background (left, black); an average trace from *FoxP*$^{5\text{-}SZ\text{-}3955}$-mutant αβ$_c$ KCs from Figure 15b is shown in red for comparison. A-type potassium current densities in *FoxP*$^{5\text{-}SZ\text{-}3955}$ αβ$_c$ KCs expressing *DN-Shal* are reduced relative to *FoxP*$^{5\text{-}SZ\text{-}3955}$ cells (right, $P < 0.0005$). Circles, means ± s.e.m.; lines, Boltzmann fits; asterisks, significant differences from *FoxP*$^{5\text{-}SZ\text{-}3955}$ control in post-hoc comparisons following two-way ANOVA. **b**, Average potassium current density trace in response to a single voltage pulse in αβ$_c$ KCs overexpressing functional *Shal* (*UAS-Shal*) in a wild-type genetic background (left, red); an average trace from wild-type αβ$_c$ KCs (*WT*, black) from Figure 15b is shown for comparison. A-type potassium current densities in *Shal*-overexpressing αβ$_c$ KCs are increased relative to wild-type cells (right, $P = 0.0079$). Circles, means ± s.e.m.; lines, Boltzmann fits; asterisks, significant differences from wild-type in post-hoc comparisons following two-way ANOVA. **c**, Average potassium current densities in αβ$_c$ KCs overexpressing *Shal* in response to a single voltage pulse before (red) and after (grey) the application of phrixotoxin-2. **d**, Steady-state activation and inactivation curves of A-type potassium currents in αβ$_c$ KCs of *Shal*-overexpressing (red), and wild-type flies (black, from Figure 15d). Circles, means ± s.e.m.; solid lines, Boltzmann fits. Mann-Whitney tests failed to detect a significant genotype effect on activation slope factor ($P = 0.8074$) and inactivation slope factor ($P = 0.1561$); *t* tests did not detect a significant effect of genotype on half-activation and half-inactivation voltages ($P = 0.3673$ and $P = 0.3669$, respectively).

the temperature-inducible overexpression of functional Shal in $\alpha\beta_c$ KCs (Figures 22c)—but not in α'β' KCs (Figure 22d)—of wild-type flies recapitulated the *FoxP* mutant phenotype. Bidirectional tuning of Shal currents in $\alpha\beta_c$ KCs thus produced a spectrum of chronometric functions, mimicking both wild-type and mutant reaction times, irrespective of the genotype of the *FoxP* locus (Figure 22b, c). These data establish $\alpha\beta_c$ KCs as the decision-relevant site, and repression of Shal as the decision-relevant mechanism, of FoxP's action.

3.5 Neurometric functions based on first spikes

Repression of Shal by FoxP is predicted to regulate the dendritic but not the axonal information-processing capabilities of $\alpha\beta_c$ KC (Figure 17), and should influence membrane potential dynamics below rather than above spike threshold. To establish a bridge between dendritic biophysics and behaviour, I recorded the membrane potential responses of $\alpha\beta_c$ KCs to changes in odour concentration.

The odour stimuli were designed to emulate as closely as possible a fly's experience of the decision zone in a behavioural chamber (Claridge-Chang et al., 2009; DasGupta et al., 2014). A continuous stream of MCH was stepped repeatedly between base (2-18 ppm, variable between trials) and peak concentrations (20 ppm, constant across trials), recreating the exact range of odour intensities and intensity contrasts encountered during behavioural testing (Figure 22). The intervals between odour intensity changes (500 ms) approximated the times flies typically spend on one side of the decision zone (Figure 22) (Claridge-Chang et al., 2009; DasGupta et al., 2014), while periodic stimulation mimicked their back-and-forth movements and allowed me to quantify $\alpha\beta_c$ KC responses to concentration steps in the preferred and null directions (see below), a prerequisite for neurometric estimates of accuracy.

Current clamp recordings during trains of 10 stimulation cycles revealed three functionally distinct classes of $\alpha\beta_c$ KC: neurons responding selectively to increases in MCH concentration ('up' cells), neurons responding to decreases in concentration ('down' cells), and unresponsive neurons (Figure 24b, c). In principle, a fly's behavioural decision could thus be based on the comparison of activity in two opponent pools of $\alpha\beta_c$ KCs representing evidence for the two alternatives—an arrangement reminiscent of the 'neuron–antineuron' configuration in visual motion discrimination (Britten et al., 1992). Learning to avoid an increase in MCH concentration would adjust, through dopamine-induced plasticity (Hige et al., 2015), the connections of these opponent $\alpha\beta_c$ KC pools to MBONs of opposite valence

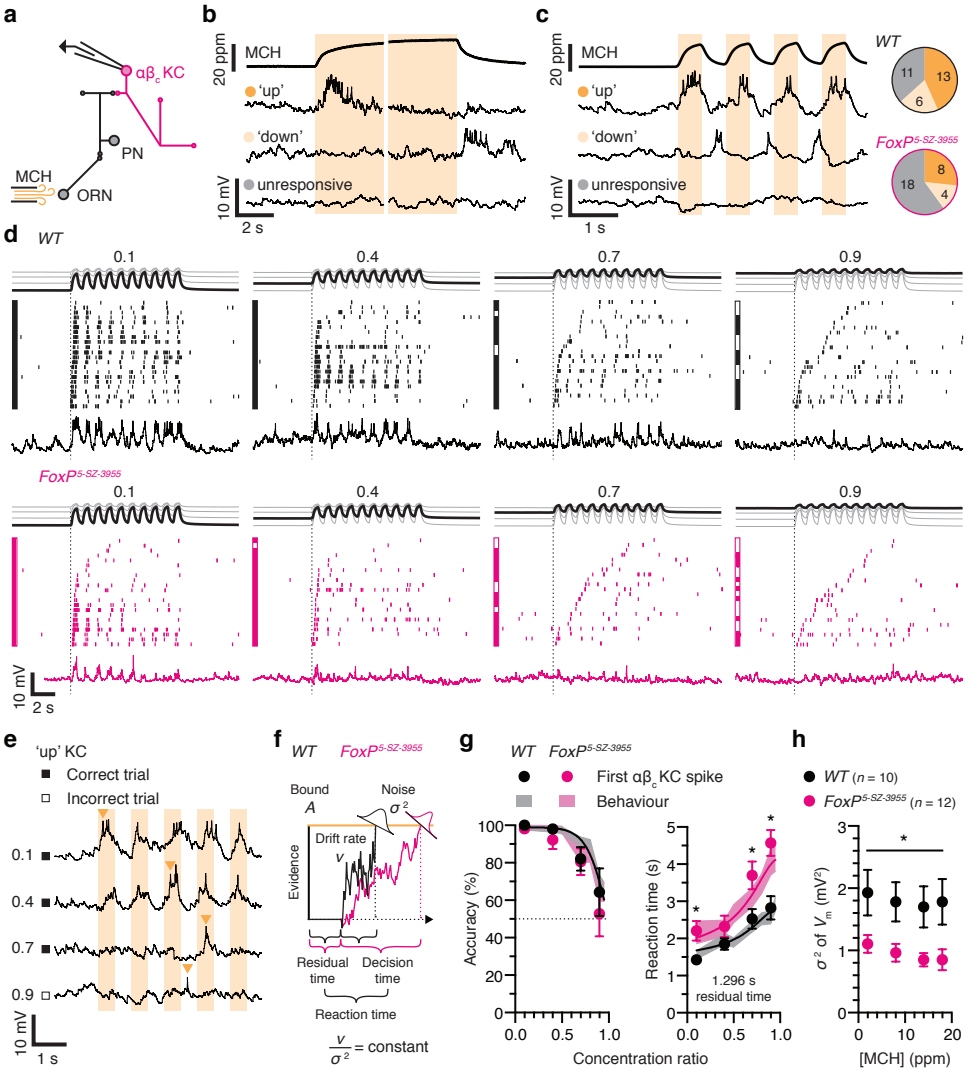


Figure 24. The first odour-evoked spikes of αβ$_c$ KCs predict behavioural performance.
a, Odour stimulation and targeted whole-cell recording in vivo from αβ$_c$ KCs expressing *NP7175-GAL4*-driven GFP. ORN, olfactory receptor neuron; PN, projection neuron; MCH, 4-methylcyclohexanol. **b**, **c**, MCH concentrations (top) and membrane voltages (bottom) of 'up' (orange), 'down' (pale orange), and unresponsive αβ$_c$ KCs (grey) during a single long (**b**) or repeated short steps (**c**) between base (2 ppm) and peak MCH concentrations (20 ppm); pie charts on the right in (**c**) indicate the numbers of the three αβ$_c$ KC types encountered in wild-type flies and homozygous *FoxP*$^{5\text{-}SZ\text{-}3955}$ mutants. 'Up' and 'down' cells were classified based on their spiking responses to a high-contrast MCH stimulus. **d**, Examples of spike rasters and voltage responses of multiple 'up' αβ$_c$ KCs in wild-type flies (black) and homozygous *FoxP*$^{5\text{-}SZ\text{-}3955}$ mutants (red) during 10 odour intensity cycles between a variable base (2–18 ppm) and a constant peak (20 ppm) MCH concentration. Measured MCH concentration time courses at the different base-to-peak ratios are displayed on top of each spike raster plot. The spike rasters represent pooled data from ≥7 neurons and are sorted, in ascending order from the bottom, by the latency of the first spike after stimulus onset (dashed lines). Filled and open squares on the left margins mark the accuracy of each individual trial as in (**e**). **e**, Voltage responses of an 'up' αβ$_c$ KC during 10 odour intensity cycles between a variable base (2–18 ppm) and a constant peak (20 ppm) MCH concentration. Only the first five of the 10 odor stimulation cycles are shown. MCH base-to-peak ratios are indicated on the left; filled and open squares mark trials whose first spikes (arrowheads) occur during odour concentration changes in the preferred or null ('correct' or 'incorrect') directions. **f**, Drift-diffusion model of evidence

accumulation. Homozygous *FoxP*$^{5\text{-}SZ\text{-}3955}$ mutants (red) exhibit lower drift rate (v) and noise (σ^2) than wild-type flies (black). **g**, Neurometric predictions of accuracy (left) and reaction time (right) as functions of MCH concentration ratio. The predictions are based on the timing and fidelity of the first MCH-evoked $\alpha\beta_c$ KC spikes in wild-type flies (black) and homozygous *FoxP*$^{5\text{-}SZ\text{-}3955}$ mutants (red). Data are means ± s.e.m. (see Table 2 for sample sizes); asterisks, significant differences from wild-type (accuracy: Mann-Whitney U test; reaction time: Kolmogorov-Smirnov test; both with Bonferroni-corrected $P < 0.0125$). Shaded bands represent 95% confidence intervals of behavioural estimates of the psychometric and chronometric functions; solid lines depict the fit of a drift-diffusion model to these behavioural data. **h**, Mean variance of $\alpha\beta_c$ KC membrane potential as a function of base MCH concentration, in wild-type flies (black) and homozygous *FoxP*$^{5\text{-}SZ\text{-}3955}$ mutants (red). Data are means ± s.e.m. Two-way ANOVA detected a significant genotype effect ($P < 0.0164$).

(Aso et al., 2014a; 2014b), so that activity in 'up' and 'down' cells elicits avoidance and approach, respectively. If the activity of 'up' cells exceeds that of 'down' cells following an increase in odour intensity, a correct reversal will result; if the activity of 'down' cells exceeds that of 'up' cells, an incorrect approach to the negatively reinforced odour will be made. The existence of 'down' cells should enable a fly to learn to discriminate a negatively reinforced low from a higher MCH concentration. Indeed, despite their innate avoidance of high MCH concentrations, flies could be trained to approach an increase and avoid a decrease of MCH concentration (Figure 25).

Since I encountered approximately twice as many 'up' as 'down' cells (pie charts in Figure 24c), my subsequent analyses concentrated on them. $\alpha\beta_c$ KCs showed virtually no background spiking activity, irrespective of the basal MCH concentration, and instead responded exclusively to changes in concentration (Figures 24b, c). In wild-type flies, large fractional increases in odour intensity (from 2 to 20 ppm MCH, a concentration ratio of 0.1) evoked action potentials with short latencies (<300 ms) that tended to repeat during the correct phase of many, if not all, successive odour concentration cycles in each trial (Figure 24d). Reducing the intensity contrast (by elevating the MCH base concentration) eroded this close temporal coupling between stimulus and response until, at a concentration ratio of 0.9, a median of three stimulation cycles were needed to evoke the first spike (Figure 24d). This 'up' cell spike now often occurred during the incorrect—that is, downward—phase of the

Genotype	Concentration ratio							
	0.1		0.4		0.7		0.9	
	KCs	Trials	KCs	Trials	KCs	Trials	KCs	Trials
NP7175-GAL4/+; UAS-CD8::GFP/+ (WT)	13	66	11	73	9	44	7	36
NP7175-GAL4/+; UAS-CD8::GFP/+; FoxP$^{5\text{-}SZ\text{-}3955}$	8	52	7	39	8	41	7	48

Table 2. Sample sizes for neurometric measurements in Figure 24g.

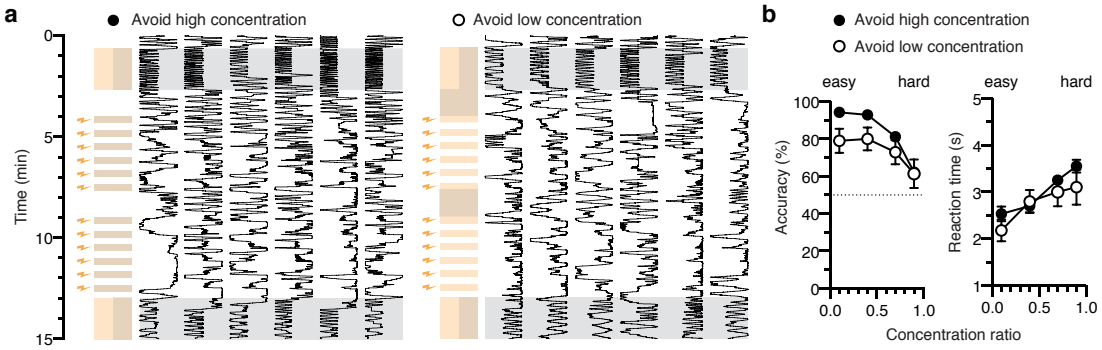


Figure 25. Discrimination between a high and a negatively reinforced lower odour concentration.

a, Positions of six exemplary flies inside behavioural chambers (horizontal dimension) as a function of time (vertical dimension) trained to avoid either a high (20 ppm, left, filled circle) or a low (2 ppm, right, open circle) concentration of MCH. An initial assessment of the flies' innate concentration preference (top) is followed by twelve presentations of the respective concentration of MCH paired with electric shock (lightning), before testing the reinforced concentration preference (bottom). Orange insets indicate the presence of MCH at high (dark) and low (light) concentrations in the corresponding parts of the chamber during the respective epochs. Note the change in concentration preference after the flies were trained to avoid the low MCH concentration (right). **b**, Accuracy (left) and reaction time (right) of the indicated training paradigms as functions of the MCH concentration ratio between the two sides of the chamber during discrimination. Data are means ± s.e.m. (see Table 3 for sample sizes).

concentration cycle (Figures 24d, e). Neuronal sensitivity and selectivity, quantified as the timing and fidelity (relative to stimulus phase) of the first odour-evoked spike, thus declined with diminishing odour contrast. The decline in sensitivity was precipitous in FoxP-deficient $\alpha\beta_c$ KCs, which suffered excessive spike delays (Figure 24d) or response failures (pie charts in Figure 24c) that likely reflect the synaptic integration defect exposed during electrical stimulation of the antennal nerve (Figure 18e, f).

Altogether, the changes in $\alpha\beta_c$ KC responses as a function of stimulus contrast parallel changes in the speed and accuracy of the decision-making animal in perceptual tasks of varying difficulty. (For a contrast with the odour responses of α'β' KCs, please see Figure 27). To make this notion rigorous, I compared the detailed psycho- and chronometric functions measured behaviourally (Figure 4) (DasGupta et al., 2014) with neurometric counterparts constructed from the separately recorded $\alpha\beta_c$ KC responses (Figure 24d).

Training paradigm	Concentration ratio							
	0.1		0.4		0.7		0.9	
	Flies	Decisions	Flies	Decisions	Flies	Decisions	Flies	Decisions
Avoid high concentration	149	478	137	461	235	890	175	653
Avoid low concentration	37	49	35	51	37	56	35	51

Table 3. Sample sizes for behavioural measurements in Figure 25b.

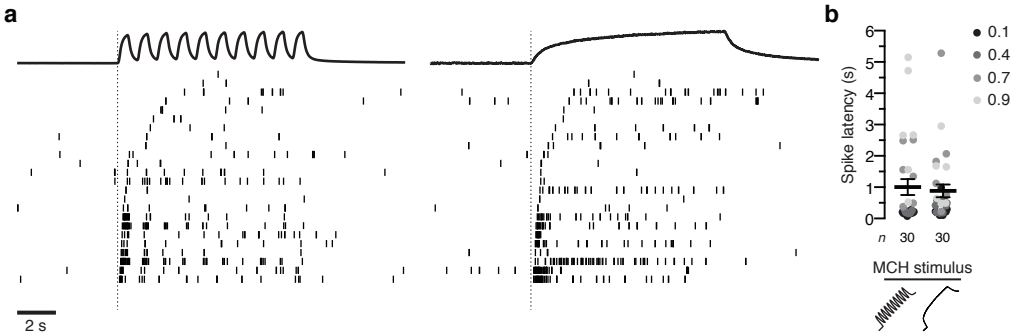


Figure 26. Spike metrics of $\alpha\beta_c$ KCs are robust under changes of odour stimulus waveform.

a, MCH stimulus waveforms (top) and example spike rasters of 'up' $\alpha\beta_c$ KCs (bottom) during 10 odor intensity cycles between a variable base (2–18 ppm) and a constant peak (20 ppm) MCH concentration (left) or a single 10-s step from variable base (2–18 ppm) to peak MCH concentration (20 ppm) and back (right). **b**, Latencies of the first MCH-evoked $\alpha\beta_c$ KC spikes during 10 odor intensity cycles between a variable base (2–18 ppm) and a constant peak (20 ppm) MCH concentration or a single 10-s step from variable base (2–18 ppm) to peak MCH concentration (20 ppm) and back, at different MCH base-to-peak ratios indicated by grey shading; numbers of trials for each ratio were matched between different waveforms. Circles, individual trials; bars, means ± s.e.m. Mann-Whitney U test failed to detect a significant difference between spike latencies under the two MCH stimulus waveforms (P = 0.2840).

Because the temporal structure of the odour stimulus used to elicit these responses was only an imperfect match to the sequences of odour concentration changes experienced by flies moving in the decision zone (Figure 22) (DasGupta et al., 2014), I tested how far the exact stimulus waveform influenced the average response latency. A train of 10 stimulation cycles over a period of 10 s yielded a spike latency distribution statistically indistinguishable from the one observed in response to a single 10-s odour pulse (Figure 26). The conclusions that follow are therefore robust.

Behavioural performance is well-described by a drift-diffusion model with three free parameters, as described in Equations (5) and (6) (Figures 1a and 24f) (Bogacz et al., 2006; DasGupta et al., 2014; Ratcliff and McKoon, 2008). The model splits the reaction time into two additive components: a difficulty- and genotype-dependent decision time, and a constant residual time (T_0) of 1.296 s, which is taken up by sensory and motor processes unrelated to the decision itself (Figures 1a and 24f) (Bogacz et al., 2006; Ratcliff, 1978; Ratcliff and McKoon, 2008). In my assay, the lion's share of the residual time is spent on locomotion: a fly walking at a mean velocity of 3.4 mm/s (DasGupta et al., 2014) from the border of the decision zone to the choice point and back will need approximately 1.2 s to travel this distance. Adding this behaviorally constrained residual time, derived from the drift-diffusion model, to the mean latency of the first $\alpha\beta_c$ KC spike predicted the reaction

times of both genotypes at all difficulty levels (Figure 24g, right panel). A similar degree of correspondence was found between the behaviourally and the neurometrically quantified accuracies, which were identical for wild-type and *FoxP*$^{5\text{-}SZ\text{-}3955}$ mutant flies (Figure 24g, left panel). Neurometric measures of accuracy were obtained by tallying the percentages of first spikes released after odour concentration steps in the preferred or null directions (for an example, please see Figure 24e).

The fact that the psychometric functions of wild-type and *FoxP*$^{5\text{-}SZ\text{-}3955}$ mutant flies overlapped while their chronometric functions differed (Figures 4c and 24g) places an additional constraint on putative neural mechanisms of sequential sampling.

In the drift-diffusion framework (Bogacz et al., 2006; Ratcliff, 1978; Ratcliff and McKoon, 2008), any change that slows the sensory evidence-driven drift of a decision variable towards threshold will not only extend the average reaction time but simultaneously reduce accuracy, due to the relatively augmented influence of diffusion noise σ^2. When the decision criterion is fixed, as is the spike threshold of wild-type and mutant $\alpha\beta_c$ KCs relative to resting potential (Figure 11b–d), maintaining constant accuracy despite lower drift rate v requires a commensurate reduction in noise, keeping v/σ^2 constant (Figure 24f). Such a compensatory change was evident in the subthreshold membrane potential fluctuations of FoxP-deficient $\alpha\beta_c$ KCs (Figure 24d, h). Because K_V4 channels act like shock absorbers

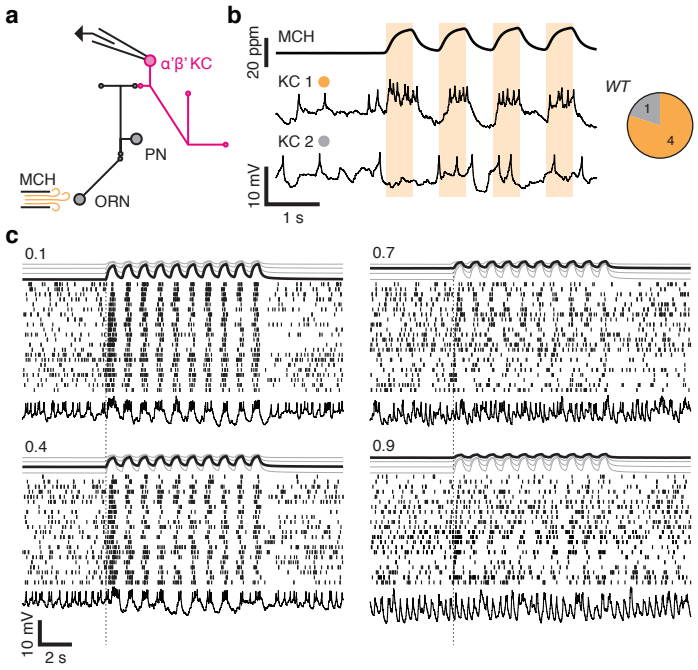


Figure 27. Odour responses of α'β' KCs.

a, Odour stimulation and targeted whole-cell recording *in vivo* from α'β' KCs expressing *VT030604-GAL4*-driven GFP. ORN, olfactory receptor neuron; PN, projection neuron; MCH, 4-methylcyclohexanol. **b**, MCH concentration (top) and membrane voltages (bottom) of responsive (orange) and unresponsive α'β' KCs (grey); the pie chart on the right indicates the numbers of the two α'β' KC types encountered in wild-type flies. **c**, Examples of spike rasters (centre) and voltage responses (bottom) of α'β' KCs in wild-type flies during 10 odour intensity cycles between a variable base (2–18 ppm) and a constant peak (20 ppm) MCH concentration. Measured MCH concentration time courses at the different base-to-peak ratios are displayed on top. The spike rasters represent pooled data from 4 neurons and are sorted, in ascending order from the bottom, by the latency of the first spike.

that limit large, rapid voltage changes (Cai et al., 2004; Hoffman et al., 1997; Kim et al., 2005), their overabundance in mutants reduced the average membrane potential variance (σ^2) to 0.5242 times that of wild-type cells (Figure 24h). Estimates, from reaction time data (DasGupta et al., 2014), of the drift rates (v) of homozygous *FoxP*$^{5\text{-}SZ\text{-}3955}$ mutant and wild-type flies yielded a virtually identical ratio of 0.5296 (Figure 24f), ensuring the required constancy of v/σ^2 across genotypes.

4 Discussion

In search of a neural integrator within the olfactory system of the fruit fly, my work links three fields of research: the gene expression control by the FoxP family of transcription factors, the biophysics of neuronal dendrites, and the neural mechanisms of decision-making.

4.1 Control of *Shal* expression by FoxP

Building upon the finding that FoxP influences the speed of perceptual decisions in *Drosophila* via a small group of third-order olfactory neurons ($\alpha\beta_c$ KCs) which express this transcription factor (DasGupta et al., 2014), I here describe the underlying mechanism on a functional level. Using calcium imaging and patch clamp electrophysiology *in vivo*, as well as behavioural experiments, I show that FoxP acts in $\alpha\beta_c$ neurons to repress the dendritic voltage-gated potassium channel Shal (K_V4). Direct, molecular evidence for this repression comes from the identification of target genes *in vivo* using FoxP-tethered DNA adenine methyltransferase, TRAP followed by qPCR experiments, and luciferase reporter assays, all performed by Laura Chan Wah Hak.

Two independently generated *FoxP-GAL4* lines (DasGupta et al., 2014; Schatton and Scharff, 2017) have located reporter gene expression to $\alpha\beta_c$ KCs in adult fruit flies, an expression pattern with striking anatomical similarity to that of *FoxP* within the brains of adult honeybees and bumblebees (Schatton and Scharff, 2017). The *FoxP* promoter-driven expression of GAL4, in all likelihood, does not provide a comprehensive account of all FoxP-positive neurons and leaves open the possibility that FoxP may be present in other types of neurons, at least to some extent. Targeted interference with *FoxP* gene expression, however, has identified $\alpha\beta_c$ KCs—labelled by either *NP6024-GAL4* or *NP7175-GAL4*—as the decision-relevant site of FoxP's action (DasGupta et al., 2014). The two *GAL4* lines (*NP6024-GAL4* and *NP7175-GAL4),* which I also used throughout this study to capture

$\alpha\beta_c$ KCs, encompass, but are not necessarily limited to FoxP-positive neurons. This could possibly account for the high variability of single-cell data (e.g. Figure 11).
TRAP experiments detected a high average abundance of *FoxP-RC* mRNA in $\alpha\beta_c$ but not in α'β' KCs. The same set of experiments also revealed that the ion channel repertoires of FoxP-positive $\alpha\beta_c$ and FoxP-negative α'β' KCs are dominated by different K_V types. While *Shal* represents the most abundant mRNA species in $\alpha\beta_c$ KCs, *Shaker* and *Shaw* predominate in α'β' KCs (Chan Wah Hak, unpublished data). Distinct mechanisms thus operate in different KC classes to control ion channel expression: In $\alpha\beta_c$ KCs, which contain both Shal and FoxP, the repressive action of FoxP limits the dosage of *Shal* mRNA, whereas in α'β' neurons, which express little Shal and no FoxP, a FoxP-independent mechanism inhibits transcription of the *Shal* locus. Such a mechanism could act, for example, through transcription factors of the LIM-homeodomain family, which exhibit mutually exclusive expression patterns with members of the FoxP-family (Cesario et al., 2016; Cesario et al., 2015; Hernández et al., 2015) and also regulate K_V expression (Wolfram et al., 2012).

The repression of *Shal* by FoxP is likely mediated by direct binding of FoxP to the *Shal* locus (Chan Wah Hak, unpublished data) and therefore distinct from a previously proposed, indirect regulatory mechanism by which vertebrate FoxP1 causes an increase, rather than a decrease, in cell surface expression of the Shal family member $K_V4.2$ (Araujo et al., 2015; Foeger et al., 2012). My data are consistent with findings in the basal ganglia of mice where a population of neurons that express FoxP2 in 72% of the cases also show markedly reduced K_V4 currents compared to their FoxP2-negative counterparts (Hernández et al., 2015). In human basal ganglia, the gene encoding $K_V4.1$ is among 141 putative target genes of human FoxP2 (Spiteri et al., 2007), suggesting a degree of evolutionary conservation in the transcriptional targets of FoxP orthologues. Vertebrate isoforms of FoxP might consequently influence time-dependent aspects of neural computation in a manner akin to the action of *Drosophila* FoxP in $\alpha\beta_c$ KCs (Figure 28).

4.2 Biophysics of neuronal dendrites

Like most nerve cells, $\alpha\beta_c$ KCs of the *Drosophila* mushroom bodies integrate incoming excitatory and inhibitory inputs to generate spiking output, yet their biophysical properties set them apart. Owing to their long membrane time constants (on average 189.6 ms; Figure 11h), FoxP-expressing $\alpha\beta_c$ KCs can retain information in the form of their membrane potential for hundreds of milliseconds, enabling them to sum individual synaptic quanta

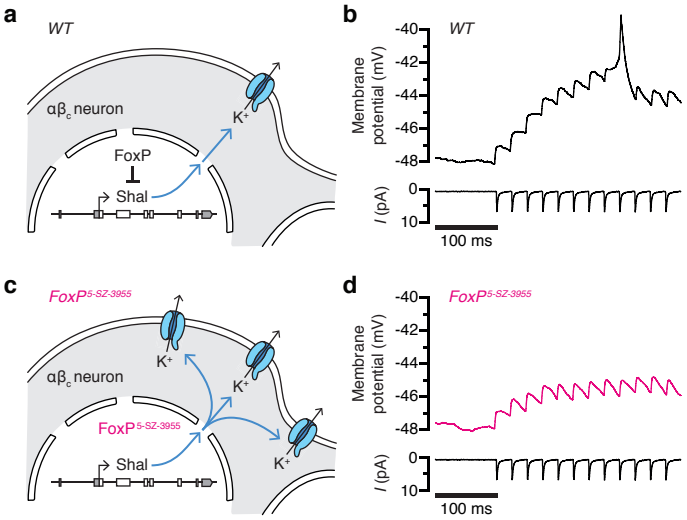


Figure 28. Proposed mechanism: FoxP represses *Shal* to regulate dendritic signal propagation.
a, Simplified schematic depicting the proposed mechanism by which FoxP influences the dendritic integration of sensory evidence. In wild-type $\alpha\beta_c$ KCs, FoxP represses the transcription of the *Shal* gene, maintaining low concentrations of *Shal* mRNA and protein within the neuron's somatodendritic compartment. **b**, Owing to their biophysical membrane properties, wild-type $\alpha\beta_c$ KCs have long intrinsic time constants allowing them to integrate individual EPSCs (bottom) efficiently up to spike threshold (top) over exceptionally long timeframes. **c**, Schematic as in (**a**). Under *FoxP*$^{5\text{-}SZ\text{-}3955}$-mutant conditions, the repressive action of FoxP on *Shal* transcription is abolished, leading to an increased abundance of functional Shal channels in the plasma membranes of $\alpha\beta_c$ KCs. **d**, In *FoxP*$^{5\text{-}SZ\text{-}3955}$ mutant $\alpha\beta_c$ KCs, voltage deflections (top), caused by individual EPSCs (bottom), are dissipated faster as they propagate along the neurite by the voltage-dependent opening of dendritic Shal channels. This results in prolonged spike latencies or failure to discharge an action potential (pictured).

efficiently up to spike threshold (Figures 18b and 28b) like a near-perfect integrate-and-fire device with only minimal leak (Koch, 1999). This contrasts with other types of KC (Turner et al., 2008), and KCs in other species (Perez-Orive et al., 2004), where active dendritic conductances favour coincidence detection. *Drosophila* $\alpha\beta_c$ KCs thus act as integrators rather than coincidence detectors of synaptic input, for two reasons: first, with an average of 7 dendritic claws per KC (Caron et al., 2013) and a mean spontaneous EPSC frequency of only 4.06 Hz (Figure 10b, c), $\alpha\beta_c$ KCs receive excitatory inputs at an extremely low rate compared to, for example pyramidal neurons (Koch, 1999); the probability of precise coincidence is therefore evanescent. Second, even if EPSPs were to coincide, with an average EPSP amplitude of 1.254 mV (Figure 21d), the canonical $\alpha\beta_c$ KC would require

simultaneous excitatory input from all its postsynaptic sites within a millisecond to bridge the 8.2-mV gap between resting membrane potential and spike threshold (Figure 11b, d). This, of course, is a purely quantitative argument assuming linear summation, and ignoring other uncertainties such as the neurotransmitter release dynamics of presynaptic PNs, yet, experiments delivering well-controlled excitatory inputs (Figure 19) at varying frequencies paint a similar picture of $\alpha\beta_c$ KCs as integrators (Figure 18b).

Most integrators designed by engineers operate in negative-feedback systems and are characterized by large gains at low and low gains at high frequencies; in other words: to prevent oscillations, integrators have to be low-pass filters (Robinson, 1989). KCs also act as low pass filters, more so than other neurons, due to the extensive cable filtering imposed by their unique anatomy (Günay et al., 2015): a single neurite of up to 80 µm length and only ~250 nm diameter connects the KC's dendritic claws to its spike initiation zone. Shal is found at exactly this compartment (Figure 17) (Trunova et al., 2011).

The overabundance of Shal in $\alpha\beta_c$ KCs of *FoxP* mutants affects active (Figures 18 and 21) as well as passive (Figure 11) membrane properties. Compared to wild-type neurons, FoxP-deficient $\alpha\beta_c$ KCs trend towards more hyperpolarized resting membrane potentials (Figure 11b). In mammalian neurons, the extent of membrane hyperpolarization caused by K_V4 channels (under the driving force of an even more hyperpolarized potassium reversal potential) is comparably small (Carrasquillo et al., 2012). All other electrophysiological differences between wild-type and FoxP-deficient cells, such as the increased afterhyperpolarization of action potentials (Figure 14), prolonged spike latencies (Figure 11c, e), and faster decay of EPSPs (Figure 21), also mirror those observed during targeted manipulations of K_V4 (Kim et al., 2005; Ping et al., 2015; Ping et al., 2011).

I have shown how the overabundance of Shal affects signal propagation along the neurite of *FoxP*-mutant $\alpha\beta_c$ KCs (Figures 18 and 21); however, the functional significance of this channel in wild-type cells remains elusive and will require further study.

Low densities of Shal could constitute an inductance-like element and might contribute to shunt peaking, a way of improving bandwidth without sacrificing too much of the KC's input resistance (Heras et al., 2016). In general, a nerve cell's bandwidth, like that of any resistor-capacitor circuit, is fundamentally limited by its input resistance (R_m) and membrane capacitance (C_m; Koch, 1999), but also by metabolic constraints (Laughlin, 2001), posing a problem for the representation of widely varying stimulus intensities as spike rates (Hong and Wilson, 2013). Yet, a specific odour can be identified, perceptually,

across a concentration range spanning 5-10 orders of magnitude (Lancet, 1986), and flies can make olfactory discriminations even in the presence of high concentrations of masking background odour (DasGupta et al., 2014). Hence, olfactory neurons, such as $\alpha\beta_c$ KCs, must have evolved means of coping with large variations in baseline odour concentrations. With a capacitance C_m of, on average, 2.41 pF and a resistance R_m of ~11.55 GΩ, a typical $\alpha\beta_c$ KC, in the absence of inductances, has a theoretical –3 dB cutoff frequency ($f_c = 1/2\pi R_m C_m$) of only 5.72 Hz. This cannot be improved by conventional means. KCs have already reached the biophysical limits of miniaturization (Faisal et al., 2005) and with the specific capacitance of a lipid bilayer being constant (Gentet et al., 2000), $\alpha\beta_c$ KCs are likely to employ inductive elements to guarantee reasonable dynamic ranges. The differential dynamic responses of wild-type and *FoxP*-mutant $\alpha\beta_c$ KCs to antennal nerve stimulation frequencies of up to ~60 Hz and ~100 Hz, respectively (Figures 7d, and 18d, f), suggest that Shal might account for such an inductance. Consistent with this idea, α'β' KCs, which do not express *Shal*, have a much narrower dynamic range (Figures 7d, and 20d). However, even in the presence of Shal, the KCs bandwidth is not sufficient to transform steady-state absolute odour concentrations linearly into spike rates and KCs must have evolved different mechanisms to reliably detect and discriminate odours. One canonical mechanism common to many sensory systems is adaptation, which can result from either intrinsic gain control or normalization to the summed activity of a larger pool of neurons (Carandini and Heeger, 2011; Hong and Wilson, 2013). In the olfactory system, this adaptation occurs at different stages and is likely mediated by lateral inhibition and excitation in the antennal lobe (Olsen et al., 2010; Olsen and Wilson, 2008; Shang et al., 2007) and by lateral inhibition in the mushroom bodies (Papadopoulou et al., 2011) (see Figure 3a, b for a circuit diagram).

Experiments depicted in Figure 24b, d reveal that the membrane potentials of $\alpha\beta_c$ KCs adapt quickly and to a remarkable extent to different baseline odour concentrations and respond virtually exclusively to concentration changes; two distinct pools of 'up' and 'down' cells signal increases or decreases in odour concentration, respectively. Such stimulus selective neurons can be found in many phyla at different stages of sensory processing (Chalasani et al., 2007; Hubel and Wiesel, 1962; Newsome et al., 1989; Wässle, 2004) and are thought to play important roles in the evolution of perceptual decisions (see below). So far, KCs, including $\alpha\beta_c$ KCs (Murthy et al., 2008), have been described mostly as responsive to the onset of an odour stimulus, but KCs responding exclusively to odour offset exist also in the moth (Ito et al., 2008). The mechanisms that give rise to these 'down' cell-responses are not

as intuitively explainable as those underlying the responses of 'up' cells. Activity caused by decreases of odour concentration could potentially originate at every stage of neural processing and might be independent of the integrative properties described in Figure 18 but could, for example, arise from rebound excitation after the release of lateral inhibition at odour offset. The neurophysiology of 'down' cells will require further investigation involving recordings of neural activity in ORNs, PNs, and KCs with concomitant manipulations of feedback loops.

In the absence of a changing odour stimulus, irrespective of the background odour concentration, the membrane potentials of $\alpha\beta_c$ KCs are virtually devoid of spiking activity (Figure 24b–d) (Murthy et al., 2008). Triggered by a change in odour concentration, $\alpha\beta_c$ KCs briefly assume an electrically active state before returning to quiescence. This seemingly bistable activity pattern is apparent during odour presentations (Figure 24b–d), but also during somatic current injections (Figure 13a) and is in stark contrast to that of α'β' neurons, which seem to employ a noisier, rate-based code (Figures 13b, and 27c), possibly enabling them to detect odours with high sensitivity and speed (Figure 7d)—a feature essential to their proposed role in alerting the fly to novel stimuli (Hattori et al., 2017). The difference between a neuron using a rate-based code (coincidence detection) and one using a spike-based code (integration) lies merely in the timeframe over which a given number of inputs have to coincide to elicit the discharge of an action potential (Shadlen and Newsome, 1994). This integration window is determined by oscillatory network dynamics (Gupta et al., 2016) as well as the intrinsic biophysical properties of an individual neuron, especially by active dendritic conductances (for an example, see Branco et al., 2016). In the case of $\alpha\beta_c$ KCs, the determinant is Shal. Like its mammalian orthologues (Cai et al., 2004), Shal dampens dendritic voltage deflections and thereby regulates the ability of $\alpha\beta_c$ KCs to summate synaptic inputs over time (Figures 18, and 28) to transition from a quiet to an electrically active state. An overabundance of Shal compromises the ability of *FoxP* mutants to execute this integration operation. How this process of synaptic integration by an identified group of neurons might relate to the psychophysics of a decision-making behaviour is outlined below.

4.3 Neural mechanisms of decision-making

Searches for the mechanisms that allow neurons to accumulate information during decision-making, compare the accumulated signal to a response criterion, and release behaviour

when the criterion is met have centred almost exclusively on suprathreshold dynamics, detectable through extracellular electrodes (Latimer et al., 2015; Mante et al., 2013; Roitman and Shadlen, 2002; Shadlen and Newsome, 2001) or genetically encoded Ca^{2+} reporters (Harvey et al., 2012). In the prevalent view, ramp-like changes in mean firing rate represent accumulating evidence in the lead-up to a choice (Roitman and Shadlen, 2002; Shadlen and Newsome, 2001). My findings suggest that $\alpha\beta_c$ KCs integrate subthreshold depolarizations evoked by individual quanta of sensory information, and that the ability to execute this operation dictates the behavioural performance of an animal. In contrast to ramping (Roitman and Shadlen, 2002; Shadlen and Newsome, 2001), stepping (Latimer et al., 2015) or high-dimensional (Harvey et al., 2012) patterns of spiking activity, which must be read out by as yet unspecified thresholding mechanisms, synaptic integration reaches a natural endpoint: the discharge of an action potential. It can therefore provide all computational elements needed to map a process of bounded evidence accumulation onto a neuronal medium.

While the ability to combine synaptic inputs is, of course, common to most neurons, $\alpha\beta_c$ KCs appear to tailor, through a particular constellation of biophysical properties, this generic process to the demands of sequential sampling. A relatively large voltage difference, equal to the linear sum of ~7 coincident EPSPs, separates resting potential and spike threshold (Figures 11b, d and 21c). This makes action potentials infrequent and, when they occur, contingent on the summation of multiple sensory inputs (Figures 18c, 24d, and 28b). A long membrane time constant (Figure 11h) provides accumulator memory (Figure 18b, c). The frequency-dependent current leak mediated by Shal could improve behavioural accuracy by reducing noise (Figure 24h) and discounting sporadic sensory events (Figure 18c, d).
The accord between the behaviourally inferred noise in the decision variable and the measured voltage noise of $\alpha\beta_c$ KCs suggests that the membrane potential of these neurons could potentially encode a quantity closely related to a decision variable. Consistent with this interpretation, decisions take the same average time to form as the membrane potential does to reach spike threshold (when factoring in the residual time returned by the drift diffusion model) (Figure 24d, g). Manipulations that advance or delay the first $\alpha\beta_c$ KC spike have corresponding consequences for reaction times (Figure 22b, c).

Strikingly, the electrical activity of as few as seven responsive $\alpha\beta_c$ KCs is sufficient to detect subtle changes in odour concentration, matching the perceptual sensitivity and speed of a fly (Figure 24g) without the need for abstract, high-dimensional representations and

intricate statistical classification (Figure 24e). This raises the question of why there are at least 80 $\alpha\beta_c$ KCs per hemisphere of the fly brain, a large fraction of which have similar response patterns (Figure 24c). Or, put differently, why doesn't the fly's performance exceed that of a single neuron? Ideally, averaging responses across KCs should increase the signal-to-noise ratio by the square root of the number of cells and thereby improve behavioural accuracy. If, however, $\alpha\beta_c$ KCs share part of their noise, this is not the case. Even weak positive correlations of noise can cause the amount of transmittable information to reach an asymptote at approximately 50-100 neurons (Zohary et al., 1994), spoiling the overall benefit of pooling signals across a neuronal population. In view of the stochastic connectivity between PNs and KCs (Caron et al., 2013), partly correlated inputs are to be expected and preliminary results from paired recordings of $\alpha\beta_c$ KCs support the notion that voltage fluctuations are driven, at least in part, by shared synaptic inputs (data not shown).

The agreement between the average latency of the first $\alpha\beta_c$ KC spike and the average reaction time leaves little scope for downstream integrators, at the level of MBONs or beyond, to accumulate multiple spikes from each $\alpha\beta_c$ KC: if this were the case, reaction times would be expected markedly to exceed spike latencies.
Instead, I envision that MBONs consider—on average—only the first few spikes emitted by members of opponent pools of 'up' and 'down' $\alpha\beta_c$ KCs. Preliminary data from whole-cell patch clamp recordings of MBONs during cyclic odour stimulations support this hypothesis.

The existence of 'up' and 'down' cells suggests that a decision could entail a race between two integrators—one that accumulates evidence for an increase in odour concentration, and another that does the opposite (Shadlen and Kiani, 2013). It is possible—though difficult at present to prove (see below)—that the winner of the race informs the animal's choice by activating MBONs of inherent valance (Aso et al., 2014b). Synapses between KCs and MBONs depress (Hige et al., 2015; Séjourné et al., 2011) when odour-driven activity in KCs and MBONs coincides with local dopaminergic reinforcement (Claridge-Chang et al., 2009; Liu et al., 2012; Schwaerzel et al., 2003). Because MBONs directing attraction are paired with aversively reinforcing dopaminergic neurons and *vice versa*, (Aso et al., 2014a; 2014b), synaptic depression will differentially weaken the connections of the opponent $\alpha\beta_c$ KC pools with MBONs of opposite valence. Paired recordings from two opponent MBONs during odour presentations before and after negative reinforcement of either an increase or a decrease in odour concentration will be crucial to reaffirm this model.

In my training regime, the expected net effect of changes to mushroom body output synapses is that activity in 'up' and 'down' cells elicits learned avoidance and approach, respectively. Correct and erroneous choices follow naturally from this model: If 'up' cells spike before 'down' cells during an increase in odour intensity, a correct reversal will result; if 'down' cells spike before 'up' cells, an incorrect approach to the negatively reinforced odour will be made. A convincing demonstration of a causal connection between the first $\alpha\beta_c$ KC spike and motor output, however, requires the recording of neural activity during the lead-up to a choice. To this end, it will be essential to devise an experimental setup that allows for stable recordings of neural activity during the training and behavioural testing of individual head-fixed flies embedded in a virtual olfactory environment. To link KC activity firmly to motor output, it will also be necessary to suppress spiking in $\alpha\beta_c$ KCs during evidence accumulation using, for example, optogenetic tools such as anion channelrhodopsins (Mohammad et al., 2017). This intervention is predicted to suspend the fly at the choice point in an indecisive state, at least until the arrival of a putative 'urgency signal'. The converse experiment, the triggering of a premature choice through optogenetic activation of $\alpha\beta_c$ KCs, poses a technically more difficult challenge: Since the functional segregation of 'up' and 'down' cells seems to arise from differential connectivity rather than from intrinsic cellular properties (a cell with an 'up' response to MCH can exhibit a 'down' response to another odorant) it is currently not possible to distinguish between the two opponent pools of $\alpha\beta_c$ KCs genetically. Theoretically, selective activation of 'up' or 'down' cells should be achievable through the injection of small, subthreshold amplitudes of depolarizing current across all $\alpha\beta_c$ KCs; applied at the right point in time, when the membrane potentials of one population of cells are closer to spike threshold than those of the other population (Figure 24c), this should trigger action potentials in one type of $\alpha\beta_c$ KC only. To inject such small, EPSC-like currents optically without activating KC-MBON synapses directly, light-gated cation channels could be targeted to the dendrites of $\alpha\beta_c$ KCs making use of, for example, the dendritic targeting motif of Shal (Figure 17) (Diao et al., 2010).

My work does not imply that the process of evidence accumulation by an individual is equivalent to, or could be explained solely by, the membrane potential of a single neuron. I do, however, recognize that dendritic signal propagation in $\alpha\beta_c$ KCs seems to represent, if not a decision-variable, then a bottleneck in sensory processing that dictates the speed of olfactory decisions. Just like in enzymatic reactions, the rate-limiting step within a sensory system can be identified, unambiguously, only if bidirectional manipulations of reaction

kinetics are possible; one must be able to both slow down and speed up the reaction. In a psychophysical context, this means that it should be possible to widen the bottleneck and reduce reaction times below those of wild-type animals, for example, by targeted overexpression of a dominant-negative Shal construct in $\alpha\beta_c$ KCs of wild-type flies.
This intervention, whose behavioural consequences remain to be tested, might also affect the accuracy of choice, because in the absence of Shal currents, sporadic sensory events (noise) are predicted to have a larger influence on the spiking activity of $\alpha\beta_c$ KCs—an effect that could potentially be compensated for by interneurons downstream of KCs.

The competition between the two pools of $\alpha\beta_c$ KCs or the MBONs sampling them could be enhanced by lateral, feedforward or pooled inhibition mediated by GABAergic or glutamatergic MBONs interconnecting mushroom body compartments (Aso et al., 2014a), or by the GABAergic anterior paired lateral neuron (Figure 3) (Lin et al., 2014; Papadopoulou et al., 2011). These circuit architectures are similar, in essence, to connectionist or reduced network models of spike-based integration (Figure 2) (Bogacz et al., 2006; Shadlen and Newsome, 2001; Usher and McClelland, 2001; Wang, 2002), but with the important difference that subthreshold rather than suprathreshold processes are responsible for the rate-limiting integration step.

"A nerve impulse arriving over a single axon terminal may not fire the cell but may modify its excitability to impulses from other sources. In an elaborate system of neurons such subthreshold effects might establish a pattern of facilitation which would determine the combination of cells fired by subsequent excitations."

— Karl S. Lashley (1951)

References

Abraham, N.M., Spors, H., Carleton, A., Margrie, T.W., Kuner, T., and Schaefer, A.T. (2004). Maintaining accuracy at the expense of speed: stimulus similarity defines odor discrimination time in mice. *Neuron 44*, 865-876.

Araujo, D.J., Anderson, A.G., Berto, S., Runnels, W., Harper, M., Ammanuel, S., Rieger, M.A., Huang, H.C., Rajkovich, K., Loerwald, K.W*., et al.* (2015). FoxP1 orchestration of ASD-relevant signaling pathways in the striatum. *Genes Dev. 29*, 2081-2096.

Aso, Y., Hattori, D., Yu, Y., Johnston, R.M., Iyer, N.A., Ngo, T.T., Dionne, H., Abbott, L.F., Axel, R., Tanimoto, H*., et al.* (2014a). The neuronal architecture of the mushroom body provides a logic for associative learning. *eLife 3*, e04577.

Aso, Y., Sitaraman, D., Ichinose, T., Kaun, K.R., Vogt, K., Belliart-Guerin, G., Placais, P.Y., Robie, A.A., Yamagata, N., Schnaitmann, C*., et al.* (2014b). Mushroom body output neurons encode valence and guide memory-based action selection in *Drosophila*. *eLife 3*, e04580.

Barnstedt, O., Owald, D., Felsenberg, J., Brain, R., Moszynski, J.P., Talbot, C.B., Perrat, P.N., and Waddell, S. (2016). Memory-Relevant Mushroom Body Output Synapses Are Cholinergic. *Neuron 89*, 1237-1247.

Bhandawat, V., Olsen, S.R., Gouwens, N.W., Schlief, M.L., and Wilson, R.I. (2007). Sensory processing in the *Drosophila* antennal lobe increases reliability and separability of ensemble odor representations. *Nat. Neurosci. 10*, 1474-1482.

Bogacz, R., Brown, E., Moehlis, J., Holmes, P., and Cohen, J.D. (2006). The physics of optimal decision making: a formal analysis of models of performance in two-alternative forced-choice tasks. *Psychol. Rev. 113*, 700-765.

Branco, T., Tozer, A., Magnus, C.J., Sugino, K., Tanaka, S., Lee, A.K., Wood, J.N., and Sternson, S.M. (2016). Near-Perfect Synaptic Integration by $Na_V1.7$ in Hypothalamic Neurons Regulates Body Weight. *Cell 165*, 1749-1761.

Britten, K.H., Shadlen, M.N., Newsome, W.T., and Movshon, J.A. (1992). The analysis of visual motion: a comparison of neuronal and psychophysical performance. *J. Neurosci. 12*, 4745-4765.

Brunton, B.W., Botvinick, M.M., and Brody, C.D. (2013). Rats and humans can optimally accumulate evidence for decision-making. *Science 340*, 95-98.

Buck, L., and Axel, R. (1991). A novel multigene family may encode odorant receptors: a molecular basis for odor recognition. *Cell 65*, 175-187.

Butler, A., Wei, A.G., Baker, K., and Salkoff, L. (1989). A family of putative potassium channel genes in *Drosophila*. *Science 243*, 943-947.

Cai, X., Liang, C.W., Muralidharan, S., Kao, J.P., Tang, C.M., and Thompson, S.M. (2004). Unique roles of SK and $K_V4.2$ potassium channels in dendritic integration. *Neuron 44*, 351-364.

Campbell, R.A.A., Honegger, K.S., Qin, H., Li, W., Demir, E., and Turner, G.C. (2013). Imaging a population code for odor identity in the *Drosophila* mushroom body. *J. Neurosci. 33*, 10568-10581.

Cannon, S.C., Robinson, D.A., and Shamma, S. (1983). A proposed neural network for the integrator of the oculomotor system. *Biol. Cybern. 49*, 127-136.

Carandini, M., and Heeger, D.J. (2011). Normalization as a canonical neural computation. *Nat. Rev. Neurosci. 13*, 51-62.

Caron, S.J., Ruta, V., Abbott, L.F., and Axel, R. (2013). Random convergence of olfactory inputs in the *Drosophila* mushroom body. *Nature 497*, 113-117.

Carrasquillo, Y., Burkhalter, A., and Nerbonne, J.M. (2012). A-type K^+ channels encoded by $K_V4.2$, $K_V4.3$ and $K_V1.4$ differentially regulate intrinsic excitability of cortical pyramidal neurons. *J. Physiol. 590*, 3877-3890.

Cesario, J.M., Almaidhan, A.A., and Jeong, J. (2016). Expression of forkhead box transcription factor genes FoxP1 and FoxP2 during jaw development. *Gene Expr. Patterns 20*, 111-119.

Cesario, J.M., Landin Malt, A., Deacon, L.J., Sandberg, M., Vogt, D., Tang, Z., Zhao, Y., Brown, S., Rubenstein, J.L., and Jeong, J. (2015). Lhx6 and Lhx8 promote palate development through negative regulation of a cell cycle inhibitor gene, p57Kip2. *Hum. Mol. Genet. 24*, 5024-5039.

Chalasani, S.H., Chronis, N., Tsunozaki, M., Gray, J.M., Ramot, D., Goodman, M.B., and Bargmann, C.I. (2007). Dissecting a circuit for olfactory behaviour in Caenorhabditis elegans. *Nature 450*, 63-70.

Chan Wah Hak, L. (unpublished data).

Chen, T.W., Wardill, T.J., Sun, Y., Pulver, S.R., Renninger, S.L., Baohan, A., Schreiter, E.R., Kerr, R.A., Orger, M.B., Jayaraman, V*., et al.* (2013). Ultrasensitive fluorescent proteins for imaging neuronal activity. *Nature 499*, 295-300.

Claridge-Chang, A., Roorda, R.D., Vrontou, E., Sjulson, L., Li, H., Hirsh, J., and Miesenböck, G. (2009). Writing memories with light-addressable reinforcement circuitry. *Cell 139*, 405-415.

Clyne, P.J., Warr, C.G., Freeman, M.R., Lessing, D., Kim, J., and Carlson, J.R. (1999). A novel family of divergent seven-transmembrane proteins: candidate odorant receptors in *Drosophila*. *Neuron 22*, 327-338.

DasGupta, S., Ferreira, C.H., and Miesenböck, G. (2014). FoxP influences the speed and accuracy of a perceptual decision in Drosophila. *Science 344*, 901-904.

de Belle, J.S., and Heisenberg, M. (1994). Associative odor learning in *Drosophila* abolished by chemical ablation of mushroom bodies. *Science 263*, 692-695.

Diao, F., Chaufty, J., Waro, G., and Tsunoda, S. (2010). SIDL interacts with the dendritic targeting motif of Shal (K_V4) K^+ channels in Drosophila. *Mol. Cell. Neurosci. 45*, 75-83.

Dietzl, G., Chen, D., Schnorrer, F., Su, K.C., Barinova, Y., Fellner, M., Gasser, B., Kinsey, K., Oppel, S., Scheiblauer, S*., et al.* (2007). A genome-wide transgenic RNAi library for conditional gene inactivation in *Drosophila*. *Nature 448*, 151-156.

Donders, F.C. (1869). Over de snelheid van psychologische processen. *Acta Psycol.* (Amst) *4*, 117-145.

Enard, W., Przeworski, M., Fisher, S.E., Lai, C.S., Wiebe, V., Kitano, T., Monaco, A.P., and Paabo, S. (2002). Molecular evolution of FOXP2, a gene involved in speech and language. *Nature 418*, 869-872.

Faisal, A.A., White, J.A., and Laughlin, S.B. (2005). Ion-channel noise places limits on the

miniaturization of the brain's wiring. *Curr. Biol. 15*, 1143-1149.

Fisek, M., and Wilson, R.I. (2014). Stereotyped connectivity and computations in higher-order olfactory neurons. *Nat. Neurosci. 17*, 280-288.

Foeger, N.C., Norris, A.J., Wren, L.M., and Nerbonne, J.M. (2012). Augmentation of $K_V4.2$-encoded currents by accessory dipeptidyl peptidase 6 and 10 subunits reflects selective cell surface $K_V4.2$ protein stabilization. *J. Biol. Chem. 287*, 9640-9650.

Gao, Q., Yuan, B., and Chess, A. (2000). Convergent projections of *Drosophila* olfactory neurons to specific glomeruli in the antennal lobe. *Nat. Neurosci. 3*, 780-785.

Gasparini, S., Losonczy, A., Chen, X., Johnston, D., and Magee, J.C. (2007). Associative pairing enhances action potential back-propagation in radial oblique branches of CA1 pyramidal neurons. *J. Physiol. 580*, 787-800.

Gasque, G., Labarca, P., Reynaud, E., and Darszon, A. (2005). Shal and shaker differential contribution to the K^+ currents in the *Drosophila* mushroom body neurons. *J. Neurosci. 25*, 2348-2358.

Gentet, L.J., Stuart, G.J., and Clements, J.D. (2000). Direct measurement of specific membrane capacitance in neurons. *Biophys. J. 79*, 314-320.

Goel, A., and Buonomano, D.V. (2014). Timing as an intrinsic property of neural networks: evidence from in vivo and in vitro experiments. *Philos. Trans. R. Soc. Lond. B Biol. Sci. 369*, 20120460.

Gold, J.I., and Shadlen, M.N. (2002). Banburismus and the brain: decoding the relationship between sensory stimuli, decisions, and reward. *Neuron 36*, 299-308.

Gold, J.I., and Shadlen, M.N. (2007). The neural basis of decision making. *Annu. Rev. Neurosci. 30*, 535-574.

Goldman, A.L., Van der Goes van Naters, W., Lessing, D., Warr, C.G., and Carlson, J.R. (2005). Coexpression of two functional odor receptors in one neuron. *Neuron 45*, 661-666.

Gouwens, N.W., and Wilson, R.I. (2009). Signal propagation in *Drosophila* central neurons. *J. Neurosci. 29*, 6239-6249.

Groszer, M., Keays, D.A., Deacon, R.M., de Bono, J.P., Prasad-Mulcare, S., Gaub, S., Baum, M.G., French, C.A., Nicod, J., Coventry, J.A., *et al.* (2008). Impaired synaptic plasticity and motor learning in mice with a point mutation implicated in human speech deficits. *Curr. Biol. 18*, 354-362.

Gruntman, E., and Turner, G.C. (2013). Integration of the olfactory code across dendritic claws of single mushroom body neurons. *Nat. Neurosci. 16*, 1821-1829.

Günay, C., Sieling, F.H., Dharmar, L., Lin, W.H., Wolfram, V., Marley, R., Baines, R.A., and Prinz, A.A. (2015). Distal spike initiation zone location estimation by morphological simulation of ionic current filtering demonstrated in a novel model of an identified *Drosophila* motoneuron. *PLoS Comput. Biol. 11*, e1004189.

Gupta, N., Singh, S.S., and Stopfer, M. (2016). Oscillatory integration windows in neurons. *Nat. Commun. 7*, 13808.

Haesler, S., Rochefort, C., Georgi, B., Licznerski, P., Osten, P., and Scharff, C. (2007). Incomplete and inaccurate vocal imitation after knockdown of FoxP2 in songbird basal ganglia nucleus Area X. *PLoS Biol. 5*, e321.

Hallem, E.A., Ho, M.G., and Carlson, J.R. (2004). The molecular basis of odor coding in the *Drosophila* antenna. *Cell 117*, 965-979.

Hallem, E.A., and Carlson, J.R. (2006). Coding of odors by a receptor repertoire. *Cell 125*, 143-160.

Hamdan, F.F., Daoud, H., Rochefort, D., Piton, A., Gauthier, J., Langlois, M., Foomani, G., Dobrzeniecka, S., Krebs, M.O., Joober, R*., et al.* (2010). De novo mutations in FOXP1 in cases with intellectual disability, autism, and language impairment. *Am. J. Hum. Genet. 87*, 671-678.

Hanes, D.P., and Schall, J.D. (1996). Neural control of voluntary movement initiation. *Science 274*, 427-430.

Hanks, T.D., Ditterich, J., and Shadlen, M.N. (2006). Microstimulation of macaque area LIP affects decision-making in a motion discrimination task. *Nat. Neurosci. 9*, 682-9.

Harvey, C.D., Coen, P., and Tank, D.W. (2012). Choice-specific sequences in parietal cortex during a virtual-navigation decision task. *Nature 484*, 62-68.

Hattori, D., Aso, Y., Swartz, K.J., Rubin, G.M., Abbott, L.F., and Axel, R. (2017). Representations of novelty and familiarity in a mushroom body compartment. *Cell 169*, 956-969 e917.

Heiman, M., Schaefer, A., Gong, S., Peterson, J.D., Day, M., Ramsey, K.E., Suarez-Farinas, M., Schwarz, C., Stephan, D.A., Surmeier, D.J*., et al.* (2008). A translational profiling approach for the molecular characterization of CNS cell types. *Cell 135*, 738-748.

Heimbeck, G., Bugnon, V., Gendre, N., Keller, A., and Stocker, R.F. (2001). A central neural circuit for experience-independent olfactory and courtship behavior in *Drosophila melanogaster*. *Proc. Natl. Acad. Sci. U. S. A. 98*, 15336-15341.

Heisenberg, M., Borst, A., Wagner, S., and Byers, D. (1985). *Drosophila* mushroom body mutants are deficient in olfactory learning. *J. Neurogenet. 2*, 1-30.

Heras, F.J., Laughlin, S.B., and Niven, J.E. (2016). Shunt peaking in neural membranes. *J. R. Soc. Interface 13*.

Hernández, V.M., Hegeman, D.J., Cui, Q., Kelver, D.A., Fiske, M.P., Glajch, K.E., Pitt, J.E., Huang, T.Y., Justice, N.J., and Chan, C.S. (2015). Parvalbumin^{+} Neurons and Npas1^{+} Neurons Are Distinct Neuron Classes in the Mouse External Globus Pallidus. *J. Neurosci. 35*, 11830-11847.

Hige, T., Aso, Y., Modi, M.N., Rubin, G.M., and Turner, G.C. (2015). Heterosynaptic Plasticity Underlies Aversive Olfactory Learning in *Drosophila*. *Neuron 88*, 985-998.

Hildebrand, J.G., and Shepherd, G.M. (1997). Mechanisms of olfactory discrimination: converging evidence for common principles across phyla. *Annu. Rev. Neurosci. 20*, 595-631.

Hille, B. (2001). Ion channels of excitable membranes, 3rd Edn. (Sunderland, Mass.: Sinauer).

Hoffman, D.A., Magee, J.C., Colbert, C.M., and Johnston, D. (1997). K^{+} channel regulation of signal propagation in dendrites of hippocampal pyramidal neurons. *Nature 387*, 869-875.

Hong, E.J., and Wilson, R.I. (2013). Olfactory neuroscience: normalization is the norm. *Curr. Biol. 23*, R1091-1093.

Hubel, D.H., and Wiesel, T.N. (1962). Receptive fields, binocular interaction and functional architecture in the cat's visual cortex. *J. Physiol. 160*, 106-154.

Huk, A.C., and Shadlen, M.N. (2005). Neural activity in macaque parietal cortex reflects temporal integration of visual motion signals during perceptual decision making. *J. Neurosci. 25*, 10420-10436.

Huston, S.J., Stopfer, M., Cassenaer, S., Aldworth, Z.N., and Laurent, G. (2015). Neural Encoding of Odors during Active Sampling and in Turbulent Plumes. *Neuron 88*, 403-418.

Inada, K., Tsuchimoto, Y., and Kazama, H. (2017). Origins of Cell-Type-Specific Olfactory Processing in the *Drosophila* Mushroom Body Circuit. *Neuron 95*, 357-367 e354.

Ito, I., Ong, R.C., Raman, B., and Stopfer, M. (2008). Sparse odor representation and olfactory learning. *Nat. Neurosci. 11*, 1177-1184.

Ito, K., Awano, W., Suzuki, K., Hiromi, Y., and Yamamoto, D. (1997). The *Drosophila* mushroom body is a quadruple structure of clonal units each of which contains a virtually identical set of neurones and glial cells. *Development 124*, 761-771.

Jefferis, G.S., Marin, E.C., Stocker, R.F., and Luo, L. (2001). Target neuron prespecification in the olfactory map of *Drosophila*. *Nature 414*, 204-208.

Kakihara, K., Shinmyozu, K., Kato, K., Wada, H., and Hayashi, S. (2008). Conversion of plasma membrane topology during epithelial tube connection requires Arf-like 3 small GTPase in *Drosophila*. *Mech. Dev. 125*, 325-336.

Katz, L.N., Yates, J.L., Pillow, J.W., and Huk, A.C. (2016). Dissociated functional significance of decision-related activity in the primate dorsal stream. *Nature 535*, 285-288.

Keene, A.C., and Waddell, S. (2007). *Drosophila* olfactory memory: single genes to complex neural circuits. *Nat. Rev. Neurosci. 8*, 341-354.

Kim, J., Wei, D.S., and Hoffman, D.A. (2005). Kv4 potassium channel subunits control action potential repolarization and frequency-dependent broadening in rat hippocampal CA1 pyramidal neurones. *J. Physiol. 569*, 41-57.

Koch, C. (1999). Biophysics of computation : information processing in single neurons (Oxford: Oxford University Press).

Konopka, G., Bomar, J.M., Winden, K., Coppola, G., Jonsson, Z.O., Gao, F., Peng, S., Preuss, T.M., Wohlschlegel, J.A., and Geschwind, D.H. (2009). Human-specific transcriptional regulation of CNS development genes by FOXP2. *Nature 462*, 213-217.

Kvon, E.Z., Kazmar, T., Stampfel, G., Yanez-Cuna, J.O., Pagani, M., Schernhuber, K., Dickson, B.J., and Stark, A. (2014). Genome-scale functional characterization of *Drosophila* developmental enhancers in vivo. *Nature 512*, 91-95.

Lai, C.S., Fisher, S.E., Hurst, J.A., Vargha-Khadem, F., and Monaco, A.P. (2001). A forkhead-domain gene is mutated in a severe speech and language disorder. *Nature 413*, 519-523.

Lancet, D. (1986). Vertebrate olfactory reception. *Annu. Rev. Neurosci. 9*, 329-355.

Lashley, K.S. (1951). Cerebral mechanisms in behavior., L. A. Jeffress, Ed. Wiley, New York, pp. 112–131.

Latimer, K.W., Yates, J.L., Meister, M.L., Huk, A.C., and Pillow, J.W. (2015). Single-trial spike trains in parietal cortex reveal discrete steps during decision-making. *Science 349*, 184-187.

Laughlin, S.B. (2001). Energy as a constraint on the coding and processing of sensory information. *Curr. Opin. Neurobiol. 11*, 475-480.

Lee, T., and Luo, L. (1999). Mosaic analysis with a repressible cell marker for studies of gene function in neuronal morphogenesis. *Neuron 22*, 451-461.

Lin, A.C., Bygrave, A.M., de Calignon, A., Lee, T., and Miesenböck, G. (2014). Sparse, decorrelated odor coding in the mushroom body enhances learned odor discrimination. *Nat. Neurosci. 17*, 559-568.

Link, S.W., and Tindall, A.D. (1971). Speed and Accuracy in Comparative Judgments of Line Length. *Percept. Psychophys. 9*, 284-288

Liu, C., Placais, P.-Y., Yamagata, N., Pfeiffer, B.D., Aso, Y., Friedrich. A.B., Siwanowicz, I., Rubin, G.M., Preat, T., and Tanimoto, H. (2012). A subset of dopamine neurons signals reward for odour

memory in *Drosophila. Nature 488,* 512-516.

Liu, W.W., and Wilson, R.I. (2013). Glutamate is an inhibitory neurotransmitter in the *Drosophila* olfactory system. *Proc. Natl. Acad. Sci. U. S. A. 110*, 10294-10299.

Mante, V., Sussillo, D., Shenoy, K.V., and Newsome, W.T. (2013). Context-dependent computation by recurrent dynamics in prefrontal cortex. *Nature 503*, 78-84.

Marin, E.C., Jefferis, G.S., Komiyama, T., Zhu, H., and Luo, L. (2002). Representation of the glomerular olfactory map in the *Drosophila* brain. *Cell 109*, 243-255.

McGuire, S.E., Le, P.T., Osborn, A.J., Matsumoto, K., and Davis, R.L. (2003). Spatiotemporal rescue of memory dysfunction in *Drosophila*. *Science 302*, 1765-1768.

Mohammad, F., Steward, J.C., Ott, S., Chlebikova, K., Chua, J.Y., Koh, T.-W., Ho, J., and Claridge-Chang, A. (2017). Optogenetic inhibition of behavior with anion channelrhodopsins. *Nat. Methods 14*, 271-274.

Mountcastle, V.B., Steinmetz, M.A., and Romo, R. (1990). Frequency discrimination in the sense of flutter: psychophysical measurements correlated with postcentral events in behaving monkeys. *J. Neurosci. 10*, 3032-44.

Murthy, M., Fiete, I., and Laurent, G. (2008). Testing odor response stereotypy in the *Drosophila* mushroom body. *Neuron 59*, 1009-1023.

Neher, E. (1992). Correction for liquid junction potentials in patch clamp experiments. *Methods Enzymol. 207*, 123-131.

Newsome, W.T., Britten, K.H., and Movshon, J.A. (1989). Neuronal correlates of a perceptual decision. *Nature 341*, 52-54.

Ng, M., Roorda, R.D., Lima, S.Q., Zemelman, B.V., Morcillo, P., and Miesenböck, G. (2002). Transmission of olfactory information between three populations of neurons in the antennal lobe of the fly. *Neuron 36*, 463-474.

Norris, A.J., and Nerbonne, J.M. (2010). Molecular dissection of I_A in cortical pyramidal neurons reveals three distinct components encoded by $K_V4.2$, $K_V4.3$, and $K_V1.4$ alpha-subunits. *J. Neurosci. 30*, 5092-5101.

Olsen, S.R., Bhandawat, V., and Wilson, R.I. (2010). Divisive normalization in olfactory population codes. *Neuron 66*, 287-299.

Olsen, S.R., and Wilson, R.I. (2008). Lateral presynaptic inhibition mediates gain control in an olfactory circuit. *Nature 452*, 956-960.

Owald, D., Felsenberg, J., Talbot, C.B., Das, G., Perisse, E., Huetteroth, W., and Waddell, S. (2015). Activity of defined mushroom body output neurons underlies learned olfactory behavior in *Drosophila*. *Neuron 86*, 417-427.

Palmer, J., Huk, A.C., and Shadlen, M.N. (2005). The effect of stimulus strength on the speed and accuracy of a perceptual decision. *J. Vis. 5*, 376-404.

Papadopoulou, M., Cassenaer, S., Nowotny, T., and Laurent, G. (2011). Normalization for sparse encoding of odors by a wide-field interneuron. *Science 332*, 721-725.

Parnas, M., Lin, A.C., Huetteroth, W., and Miesenböck, G. (2013). Odor discrimination in *Drosophila*: from neural population codes to behavior. *Neuron 79*, 932-944.

Perez-Orive, J., Bazhenov, M., and Laurent, G. (2004). Intrinsic and circuit properties favor coincidence detection for decoding oscillatory input. *J. Neurosci. 24*, 6037-6047.

Pikielny, C.W., Hasan, G., Rouyer, F., and Rosbash, M. (1994). Members of a family of *Drosophila* putative odorant-binding proteins are expressed in different subsets of olfactory hairs. *Neuron 12*, 35-49.

Ping, Y., Hahm, E.T., Waro, G., Song, Q., Vo-Ba, D.A., Licursi, A., Bao, H., Ganoe, L., Finch, K., and Tsunoda, S. (2015). Linking Aβ42-induced hyperexcitability to neurodegeneration, learning and motor deficits, and a shorter lifespan in an Alzheimer's model. *PLoS. Genet. 11*, e1005025.

Ping, Y., Waro, G., Licursi, A., Smith, S., Vo-Ba, D.A., and Tsunoda, S. (2011). Shal/K(v)4 channels are required for maintaining excitability during repetitive firing and normal locomotion in *Drosophila*. *PloS one 6*, e16043.

Podlaski, W.F., Seeholzer, A., Groschner, L.N., Miesenböck, G., Ranjan, R., and Vogels, T.P. (2017). Mapping the function of neuronal ion channels in model and experiment. *eLife 6*, e22152.

Quinn, W.G., Harris, W.A., and Benzer, S. (1974). Conditioned behavior in *Drosophila melanogaster*. *Proc. Natl. Acad. Sci. U. S. A. 71*, 708-712.

Raman, B., Joseph, J., Tang, J., and Stopfer, M. (2010). Temporally diverse firing patterns in olfactory receptor neurons underlie spatiotemporal neural codes for odors. *J. Neurosci. 30*, 1994-2006.

Ratcliff, R. (1978). Theory of Memory Retrieval. *Psychol. Rev. 85*, 59-108.

Ratcliff, R., Cherian, A., and Segraves, M. (2003). A comparison of macaque behavior and superior colliculus neuronal activity to predictions from models of two-choice decisions. *J. Neurophysiol. 90*, 1392-1407.

Ratcliff, R., and McKoon, G. (2008). The diffusion decision model: theory and data for two-choice decision tasks. *Neural Comput. 20*, 873-922.

Ressler, K.J., Sullivan, S.L., and Buck, L.B. (1994). Information coding in the olfactory system: evidence for a stereotyped and highly organized epitope map in the olfactory bulb. *Cell 79*, 1245-1255.

Rinberg, D., Koulakov, A., and Gelperin, A. (2006). Speed-accuracy tradeoff in olfaction. *Neuron 51*, 351-358.

Robinson, D.A. (1989). Integrating with neurons. *Annu. Rev. Neurosci. 12*, 33-45.

Roitman, J.D., and Shadlen, M.N. (2002). Response of neurons in the lateral intraparietal area during a combined visual discrimination reaction time task. *J. Neurosci. 22*, 9475-9489.

Salzman, C.D., Britten, K.H., and Newsome, W.T. (1990) Cortical microstimulation influences perceptual judgements of motion direction. *Nature 346*, 174-7.

Santos, M.E., Athanasiadis, A., Leitao, A.B., DuPasquier, L., and Sucena, E. (2011). Alternative splicing and gene duplication in the evolution of the FoxP gene subfamily. *Mol. Biol. Evol. 28*, 237-247.

Sato, K., Pellegrino, M., Nakagawa, T., Nakagawa, T., Vosshall, L.B., and Touhara, K. (2008). Insect olfactory receptors are heteromeric ligand-gated ion channels. *Nature 452*, 1002-1006.

Schatton, A., and Scharff, C. (2017). FoxP expression identifies a Kenyon cell subtype in the honeybee mushroom bodies linking them to fruit fly $\alpha\beta_c$ neurons. *Eur. J. Neurosci. 46*, 2534-2541.

Schwaerzel, M., Monastirioti, M., Scholz, H., Friggi-Grelin, F., Birman, S., and Heisenberg, M. (2003). Dopamine and octopamine differentiate between aversive and appetitive olfactory memories in *Drosophila. J. Neurosci. 23*, 10495-10502.

Seaman, M.A., Levin, J.R., and Serlin, R.C. (1991). New developments in pairwise multiple comparisons: Some powerful and practicable procedures. *Psychol. Bull. 110*, 577-586.

Séjourné, J., Placais, P.-Y., Aso, Y., Siwanowicz, I., Trannoy, S., Thoma, V., Tedjakumala, S.R., Rubin, G.M., Tchénio, P., Ito, K., Isabel, G., Tanimoto, H., and Preat, T. (2011). Mushroom body efferent neurons responsible for aversive olfactory memory retrieval in *Drosophila*. *Nat. Neurosci. 14*, 903-910.

Shadlen, M.N., and Kiani, R. (2013). Decision making as a window on cognition. *Neuron 80*, 791-806.

Shadlen, M.N., and Newsome, W.T. (1994). Noise, neural codes and cortical organization. *Curr. Opin. Neurobiol. 4*, 569-579.

Shadlen, M.N., and Newsome, W.T. (2001). Neural basis of a perceptual decision in the parietal cortex (area LIP) of the rhesus monkey. *J. Neuropysiol. 86*, 1916-1936.

Shang, Y., Claridge-Chang, A., Sjulson, L., Pypaert, M., and Miesenböck, G. (2007). Excitatory local circuits and their implications for olfactory processing in the fly antennal lobe. *Cell 128*, 601-612.

Sheng, M., Tsaur, M.L., Jan, Y.N., and Jan, L.Y. (1992). Subcellular segregation of two A-type K^+ channel proteins in rat central neurons. *Neuron 9*, 271-284.

Sia, G.M., Clem, R.L., and Huganir, R.L. (2013). The human language-associated gene SRPX2 regulates synapse formation and vocalization in mice. *Science 342*, 987-991.

Spiteri, E., Konopka, G., Coppola, G., Bomar, J., Oldham, M., Ou, J., Vernes, S.C., Fisher, S.E., Ren, B., and Geschwind, D.H. (2007). Identification of the transcriptional targets of FOXP2, a gene linked to speech and language, in developing human brain. *Am. J. Hum. Genet. 81*, 1144-1157.

Strauss, R. (2002). The central complex and the genetic dissection of locomotor behaviour. *Curr. Opin. Neurobiol. 12*, 633-638.

Tanaka, N.K., Tanimoto, H., and Ito, K. (2008). Neuronal assemblies of the *Drosophila* mushroom body. *J. Comp. Neurol. 508*, 711-755.

Tkacik, G., and Bialek, W. (2016). Information Processing in Living Systems. *Annu. Rev. Conden. Ma. P. 7*, 89-117.

Trunova, S., Baek, B., and Giniger, E. (2011). Cdk5 regulates the size of an axon initial segment-like compartment in mushroom body neurons of the *Drosophila* central brain. *J. Neurosci. 31*, 10451-10462.

Turner, G.C., Bazhenov, M., and Laurent, G. (2008). Olfactory representations by *Drosophila* mushroom body neurons. *J. Neurophysiol. 99*, 734-746.

Uchida, N., and Mainen, Z.F. (2003). Speed and accuracy of olfactory discrimination in the rat. *Nat. Neurosci. 6*, 1224-1229.

Usher, M., and McClelland, J.L. (2001). The time course of perceptual choice: the leaky, competing accumulator model. *Psychol. Rev. 108*, 550-592.

Vargha-Khadem, F., Watkins, K., Alcock, K., Fletcher, P., and Passingham, R. (1995). Praxic and nonverbal cognitive deficits in a large family with a genetically transmitted speech and language disorder. *Proc. Natl. Acad. Sci. U. S. A. 92*, 930-933.

Vassar, R., Chao, S.K., Sitcheran, R., Nunez, J.M., Vosshall, L.B., and Axel, R. (1994). Topographic organization of sensory projections to the olfactory bulb. *Cell 79*, 981-991.

Vickers, D. (1970). Evidence for an accumulator model of psychophysical discrimination. *Ergonomics 13*, 37-58.

Vosshall, L.B., Amrein, H., Morozov, P.S., Rzhetsky, A., and Axel, R. (1999). A spatial map of olfactory receptor expression in the *Drosophila* antenna. *Cell 96*, 725-736.

Vosshall, L.B., Wong, A.M., and Axel, R. (2000). An olfactory sensory map in the fly brain. *Cell 102*, 147-159.

Wang, X.J. (2002). Probabilistic decision making by slow reverberation in cortical circuits. *Neuron 36*, 955-968.

Wässle, H. (2004). Parallel processing in the mammalian retina. *Nat. Rev. Neurosci. 5*, 747-757.

Wei, A., Covarrubias, M., Butler, A., Baker, K., Pak, M., and Salkoff, L. (1990). K^+ current diversity is produced by an extended gene family conserved in *Drosophila* and mouse. *Science 248*, 599-603.

Wicher, D., Schafer, R., Bauernfeind, R., Stensmyr, M.C., Heller, R., Heinemann, S.H., and Hansson, B.S. (2008). *Drosophila* odorant receptors are both ligand-gated and cyclic-nucleotide-activated cation channels. *Nature 452*, 1007-1011.

Wilson, R.I., and Mainen, Z.F. (2006). Early events in olfactory processing. *Annu. Rev. Neurosci. 29*, 163-201.

Wolfram, V., Southall, T.D., Brand, A.H., and Baines, R.A. (2012). The LIM-homeodomain protein islet dictates motor neuron electrical properties by regulating K^+ channel expression. *Neuron 75*, 663-674.

Yates, J.L., Park, I.M., Katz, L.N., Pillow, J.W., and Huk, A.C. (2017). Functional dissection of signal and noise in MT and LIP during decision-making. *Nat. Neurosci. 20*, 1285-1292.

Zohary, E., Shadlen, M.N., and Newsome, W.T. (1994). Correlated neuronal discharge rate and its implications for psychophysical performance. *Nature 370*, 140-143.